

POLITECNICO DI MILANO

Scuola di Ingegneria Industriale e dell'Informazione

Corso di laurea Magistrale
in Ingegneria Meccanica



INFLUENCE OF INLET PRESSURE LOSS ON POWER AND EFFICIENCY OF A MICRO GAS TURBINE

Relatore: Prof. Giacomo Bruno PERSICO

Co-relatore: Prof. Reinhard WILLINGER

Tesi di Laurea Magistrale di
Gherardo QUARIO RONDO
Matricola 784107

Anno Accademico 2013-2014

Alla mia Mamma e al mio GRANDE Papà

Colui che è stato e sempre sarà, l'esempio di UOMO che un giorno anch'io vorrei essere!!!

...

Finalmente ci siamo, è' da tanto che rincorro questo momento! Eh si, il momento più bello è proprio quello in cui potersi lasciare andare e ringraziare tutte le persone che in questi 7 anni, hanno reso meno faticose, più divertenti e stimolanti le numerose sfide cui il Poli mi ha sottoposto.

Sono riconoscente al Prof. Reinhard Willinger per avermi dato la possibilità di svolgere questo lavoro di Tesi presso la meravigliosa Università Tecnica di Vienna, ed anche il Prof. Giacomo Persico, che sebbene si sia trovato così lontano nelle fasi iniziali del lavoro ha accettato di seguirmi così da vicino nelle fasi finali di stesura della Tesi, GRAZIE!

Voglio ringraziare tanto Francesca, per aver saputo cum-patire insieme a me le fatiche Politecniche, per avermi sostenuto laddove la mente cedeva e per aver rallegtrato momenti difficili e faticosi. Non ti sei mai tirata indietro in seguito ad una mia richiesta di aiuto e grazie a te, ho sempre trovato lo stimolo giusto per superare miei limiti che pensavo fossero insuperabili!

Grazie ai miei Amici Cabbo, Carlo, Raul e Orso con i quali condivido da tanto una profonda amicizia, che sono sicuro continuerà ancora molto molto a lungo! Dalla moto, allo sport, alle uscite, abbiamo sempre vissuto momenti epici! E poi grazie al Poli, che mi ha fatto conoscere Nico, Matte, Gigi, Davide e Lorenzo. Avete contribuito a rendere divertenti le tante giornate passate a ricopiare geroglifici (opss, appunti) scritti alla lavagna, ma anche a passare momenti extrauniversitari incredibilmente divertenti. Un grazie particolare a Lorenzo, con il quale i mesi Viennesi sono stati ricchi di sorprese e cene all' Italiana dalle ricette stellate. E infine un grazie al Bruco Nicola, aiuto fondamentale per la corretta stesura della Tesi ed esperto canoista compagno di allenamenti! Brinderemo insieme con lo spumante Terra dei Forti, bottiglia conquistata faticosamente dopo una lunga e tormentata gara nuoto-canoistica nelle gelide acque del fiume Adige.

Se anche non direttamente citati, ringrazio anche tutti voi altri amici e amiche, che con me avete sempre voluto vivere tanti momenti belli, sportivi e non.

Penso ai nonni che non ci sono più, e sono sicuro che il nonno Giorgio sarà contento di avere come collega un nipote! Ringrazio il resto della mia famiglia e in particolare la Nonna Lilli, le Zie e gli Zii, i cugini tra cui Alice, Chiara Federica e Filippo con cui crescere è stato proprio divertente!

E poi i miei due fratelli Lorenz e Fede, che oltre ad essere più grandi di me, sono stati davvero grandi per me, facendomi da apripista in tante situazioni e da esempio in molte altre.

Infine ringrazio i miei genitori che sempre in questi 20 anni di studio, hanno saputo insegnarmi a gioire delle piccole vittorie, senza fare drammi per le piccole sconfitte. E se anche, Papi, oggi non sei qui, so che in realtà starai sorridendo, fiero di me. Grazie per avermi reso capace di gioire di ogni istante di vita!

Gherardo

Contents

List of Figures	v
List of Tables	ix
Abstract.....	xi
Italian Abstract.....	xiii
Italian Extended Abstract	xv
Chapter 1.....	1
Introduction	1
1.1 General contents	1
1.2 Small gas turbines	2
1.2.1 An historical background	2
Chapter 2.....	5
The ROVER 1S/60	5
2.1 Overall features	5
2.2 Main components	7
2.2.1 Compressor stage	8
2.2.2 Combustion Chamber.....	12
2.2.3 Turbine stage	15
Chapter 3.....	19
The Test Bed	19
3.1 The TU WIEN's test bed.....	19
3.2 Components and transducers.....	21
3.2.1 Inlet and outlet ducts	21
3.2.2 Absolute pressure transducers	22
3.2.3 Differential pressure transducers.....	23
3.2.4 Thermocouples	24
3.2.5 Speed adaptor and eddy current brake	26
3.3 Mass flow rate measurement.....	28
3.3.1 Norms for volume and mass flow rate measurement.....	29
3.3.1.1 EN-ISO 5167-1 and 5167-2	29

3.3.1.2 VDI-VDE 2041.....	34
3.3.2 Adopted diaphragms.....	35
Chapter 4.....	38
Tests	38
4.1 Tests preparation.....	38
4.2 Data acquisition setbacks.....	39
4.2.1 Test one repetition for the 169,5mm diaphragm	40
4.2.2 Chimney Effect.....	40
4.2.3 Calibration for the outlet differential pressure transducer	41
4.3 Data set	42
4.3.1 Air and fuel properties	42
4.3.2 Static pressure and total temperature	45
4.3.3 Estimated values	47
4.4 Data processing and ROVER 1S/60 performance	50
4.4.1 169,5 mm diaphragm	50
4.4.1.1 Compressor	50
4.4.1.2 Combustion chamber	51
4.4.1.3 Turbine.....	54
4.4.2 140mm Diaphragm	58
4.4.3 115,8mm Diaphragm	60
Chapter 5.....	62
Gas Turbine Performances.....	62
5.1 ISO norm performances.....	62
5.2 Factors Affecting Gas Turbine Performance	63
5.2.1 Ambient temperature	63
5.2.1.1 Effects on ROVER 1S/60 performances	64
5.2.1.2 Sensitivity analysis	66
5.2.2 Ambient pressure	66
5.2.3 Humidity	68
5.2.4 Inlet & outlet pressure loss	68
Chapter 6.....	70

Influence of Inlet Pressure Loss on the ROVER 1S/60s's Performances	70
6.1 Experimental results	70
6.1.1 Varying T_3	70
6.1.2 Keeping T_3 constant	74
6.2 Modelling of phenomenon	77
6.2.1 Model's hypothesis	77
6.2.2 Model's equations	78
6.2.3 Model fitting to experimental data	81
6.3 Comparison with the results obtained for a heavy duty gas turbine	85
6.4 Conclusions	86
Notation	88
List of Symbols	88
References	91
Appendix A1	93
Eulerian work	93
Appendix A2	95
Polytropic Efficiency	95

List of Figures

Figure 1.1	<i>ROVER 1S/60 and simple Brayton_Joule cycle performed by</i>	2
Figure 1.2	<i>Centrifugal- axial early gas turbine</i>	3
Figure 2.1	<i>Emblem of Rover's company</i>	5
Figure 2.2	<i>Radial compressor-axial turbine and gas flow diagram</i>	7
Figure 2.3	<i>Surged and choked regions pointed out into the performance map</i>	8
Figure 2.4	<i>Rover's rotor</i>	9
Figure 2.5	<i>Radial blades geometry, [1]</i>	10
Figure 2.6	<i>Interblade Jet&Wake flow</i>	11
Figure 2.7	<i>Gas turbine's combustion chamber</i>	12
Figure 2.8	<i>Lean vs. rich combustion</i>	13
Figure 2.9	<i>Toroidal flow and axial swirler</i>	13
Figure 2.10	<i>Typical combustion chamber</i>	14
Figure 2.11	<i>ROVER 1S/60's combustor [3]</i>	15
Figure 2.12	<i>Internal combustor pressure losses</i>	15
Figure 2.13	<i>Section of the ROVER's turbine stage</i>	17
Figure 3.1	<i>Scheme of TU WIEN's test bed</i>	20
Figure 3.2	<i>Main and eddy current brake's panels</i>	21
Figure 3.3	<i>Inlet duct and old control panel before Januschewsky's renovation</i>	22
Figure 3.4	<i>Absolute pressure transducer [6]</i>	22
Figure 3.5	<i>Scheme of an inductive differential pressure transducer</i>	23
Figure 3.6	<i>Thermocouple</i>	25
Figure 3.7	<i>Thermocouple's scheme</i>	25
Figure 3.8	<i>Thermocouples positioning</i>	26

Figure 3.9 <i>Borghi&Saveri eddy current braking system with load cell connection</i>	27
Figure 3.10 <i>Eddy current braking system principle of functioning</i>	28
Figure 3.11 <i>169.5mm inlet diaphragm load points represented on functioning map</i>	28
Figure 3.12 <i>Pipe line and Bernoulli's terms</i>	30
Figure 3.13 <i>Measuring points</i>	31
Figure 3.14 <i>C coefficient function of Re and β</i>	32
Figure 3.15 <i>Scheme of the inlet measuring system</i>	34
Figure 3.16 <i>Normed orifice plate</i>	35
Figure 3.17 <i>169.5 mm orifice plate</i>	36
Figure 4.1 <i>ROVER's functioning map</i>	39
Figure 4.2 <i>Focus on the three different diaphragms operating load points</i>	39
Figure 4.3 <i>T3-P_eff diagram and the unforeseen phenomenon</i>	40
Figure 4.4 <i>Δp_{04} test check equipment</i>	42
Figure 4.5 <i>Temperature-specific heat at constant pressure diagram and influence of λ</i>	44
Figure 4.6 <i>Static pressure probe</i>	46
Figure 4.7 <i>Simplified scheme of combustion process</i>	52
Figure 4.8 <i>Loss power in function of gearbox output shaft revolutions</i>	55
Figure 5.1 <i>Influence of ambient temperature increasing on the operating point</i>	63
Figure 5.2 <i>Ideal Joule-Brayton open cycle s-T diagram</i>	64
Figure 5.3 <i>Ideal Joule-Brayton open cycle at constant TIT=700°C in Duhovic's tests[14]</i>	65
Figure 5.4 <i>Effects of ambient pressure lowering</i>	67
Figure 5.5 <i>Humidity effect curve for an heavy duty gas turbine [15]</i>	68
Figure 5.6 <i>Inlet and outlet pressure loss such as isohentalpic transformations</i>	69

Figure 6.1 <i>Changing in Nett Power performance as a consequence of TIT variation</i>	<i>71</i>
Figure 6.2 <i>Changing in global thermal efficiency as a consequence of TIT variation</i>	<i>71</i>
Figure 6.3 <i>Mass flow rate decreases as soon as inlet pressure loss arises.....</i>	<i>72</i>
Figure 6.4 <i>Inlet pressure loss drops when operational load increases or diaphragm's diameter decreases</i>	<i>72</i>
Figure 6.5 <i>Air Fuel equivalent Ratio drops in correspondence of higher T3 ...</i>	<i>73</i>
Figure 6.6 <i>Specific fuel consumption drops when load increases.....</i>	<i>73</i>
Figure 6.7 <i>Inlet pressure loss increase modifies the inlet air mass flow rate ...</i>	<i>74</i>
Figure 6.8 <i>Small variations in the reduced mass flow rate coefficient can be ignored.....</i>	<i>75</i>
Figure 6.9 <i>Negative influence of inlet pressure loss on gas turbine's power ...</i>	<i>76</i>
Figure 6.10 <i>Negative influence of inlet pressure loss on gas turbine's efficiency</i>	<i>77</i>
Figure 6.11 <i>Model and experimental Efficiency ratios as a function of ξ.....</i>	<i>83</i>
Figure 6.12 <i>Model and experimental Power ratios as a function of ξ.....</i>	<i>84</i>
Figure 6.13 <i>Model and experimental Efficiency ratio as a function of $\Delta p _{01}$</i>	<i>85</i>
Figure 6.14 <i>Model and experimental Power ratio as a function of $\Delta p _{01}$.....</i>	<i>85</i>
Figure 6.15 <i>Influence of inlet pressure loss on power and efficiency of a heavy duty GE MS7001EA gas turbine.</i>	<i>86</i>
Figure A2.1 <i>Compression transformation</i>	<i>95</i>
Figure A2.2 <i>Real adiabatic compression</i>	<i>96</i>

List of Tables

Table 2.1 <i>Some applications of Rover 1S series</i>	6
Table 2.2 <i>Rover 1S/60 specification</i>	8
Table 3.1 <i>JUMO 40.4346 series absolute pressure transducers</i>	23
Table 3.2 <i>JUMO 40.4304 series differential pressure transducers</i>	24
Table 3.3 <i>K-series Thermocouples' properties</i>	26
Table 4.1 <i>Unsteady output data given by $\Delta p04$ differential pressure transducer</i>	42
Table 4.10 <i>T3th determination with a simple iterative procedure</i>	56
Table 4.11 <i>Combustor's performance</i>	57
Table 4.12 <i>Calculated values</i>	58
Table 4.13 <i>Turbine properties</i>	61
Table 4.14 <i>Evaluation of the test bed performances with the 140mm diaphragm</i>	62
Table 4.15 <i>Evaluation of the test bed performances with the 115.8mm diaphragm</i>	64
Table 4.2 <i>Correspondence between Air Fuel equivalence Ratio and gas constant</i>	44
Table 4.3 <i>Air properties at 22 [°C]</i>	46
Table 4.4 <i>Diesel properties</i>	46
Table 4.5 <i>Inlet pipe flow conditions</i>	48
Table 4.6 <i>Outlet duct flow conditions</i>	48
Table 4.7 <i>169.5 mm test section output data</i>	50
Table 4.8 <i>140 mm test section output data</i>	51
Table 4.9 <i>115.8 mm test section output data</i>	52

Table 5.1	<i>Final results of Duhovic's analysis: influence of Ambient Temperature on Power and Efficiency of ROVER 1S/60, at constant TIT values[14]</i>	68
Table 5.2	<i>ROVER 1S/60's sensitivity coefficients [14]</i>	69
Table 6.1	<i>ROVER's performance changes adopting different diaphragms</i>	79
Table 6.2	<i>Input model's data</i>	85
Table 6.4	<i>Experimental ratios</i>	86

Abstract

This final master Thesis work has been fulfilled at the *Technische Universität WIEN*, during the Erasmus studying exchange program. It consisted of different experimental tests, in order to investigate the influence of inlet pressure loss on power and efficiency of a ROVER 1S/60 micro gas turbine. The machine was housed into a fully equipped test bed at the department of Fluid Machines and Energetic Systems. The gas turbine was run in different tests, adopting three different diaphragms, able to induce different inlet pressure loss. The experimental results and the comparison with the results obtained with an analytical model has confirmed the reduction of global performances when inlet pressure loss arose. Particularly, the percentage reduction of power has been greater than the percentage reduction of efficiency. Furthermore the comparison with the performance reduction occurred to a heavy duty gas turbine, has permitted to establish the greater drop of power and efficiency for the ROVER 1S/60, in correspondence to the same value of inlet pressure loss. This means that small size gas turbine are more heavily affected by inlet pressure loss than those of greater size and power.

Key words: Micro gas turbine, ROVER 1S/60, diaphragm, inlet pressure loss, power and efficiency

Italian Abstract

Il lavoro di tesi è stato svolto presso la *Technische Universität WIEN*, nel corso del programma di scambio Erasmus ed è consistito nell'andare a indagare come le perdite di carico in fase di aspirazione avessero influenza sulle prestazioni di una micro turbina a gas ROVER 1S/60. La micro turbina a gas era alloggiata all'interno di un banco prova strumentato, già allestito in precedenza e utilizzato a fini didattici. Mediante una campagna di prove sperimentali, con l'utilizzo di diversi diaframmi normati, si sono potute indurre perdite di carico via via crescenti. Il calcolo delle prestazioni ottenute per via sperimentale e la comparazione con i risultati ottenuti grazie all'utilizzo di un semplice modello matematico, ha confermato il trend di decremento in termini di rendimento e potenza visto dalla ROVER 1s/60 all'aumentare delle perdite di carico all'ingresso. In particolar modo, si è assistito ad una riduzione percentuale di potenza maggiore della riduzione percentuale di rendimento. Un ulteriore confronto con i risultati ottenuti per via sperimentale su un modello di turbina a gas heavy duty, ha permesso di evidenziare come il calo di prestazioni sia stato più importante nel caso della micro turbina a gas oggetto di studio. Ciò dimostra come, all'aumentare delle perdite di carico in fase di aspirazione, le turbine a gas di piccola taglia siano maggiormente affette da un calo di prestazioni, di quanto non lo siano le turbine a gas di grande potenza.

Parole chiave: Micro turbina a gas, ROVER 1s/60, diaframma, perdite di carico in aspirazione, potenza e rendimento

Italian Extended Abstract

In questi anni il mercato delle turbine a gas ha assistito ad una impressionante espansione. Basti pensare all'impiego massiccio che stanno avendo negli impianti di produzione di energia elettrica o come motori per propellere gli aeromobili destinati al trasporto di persone e cose. La turbina a gas è stata definita da molti come la macchina più studiata al mondo e difatti a partire dalla fine degli anni ottanta ha visto crescere il suo utilizzo nelle centrali di produzione di potenza elettrica, andando a sostituire sempre più le centrali tradizionali a ciclo Rankine. Una volta collocate in impianti a ciclo combinato e/o cogenerativo, gli elevati rendimenti di ciclo hanno fatto sì che il loro utilizzo si rivelasse sempre più vantaggioso dal punto di vista economico e ambientale. Per quanto riguarda il settore aeronautico, ma anche quello navale, le maggiori aziende produttrici hanno profuso notevoli sforzi al fine di soddisfare la crescente richiesta di turbine a gas per impiego propulsivo. La flotta aeronautica civile in quasi vent'anni, dal 1996 ad oggi, ha visto raddoppiare il numero di velivoli nei cieli di tutto il mondo.

L'aumento del costo delle fonti di energia primaria e le crescenti limitazioni in termini di emissioni inquinanti e sonore, ha spinto la ricerca a trovare soluzioni sempre più estreme nel campo dei materiali e dell'aerodinamica, permettendo al contempo di innalzare il rendimento di ciclo, la potenza e di diminuirne la massa complessiva.

Tuttavia, sebbene solo negli ultimi vent'anni si sia assistito ad un vero e proprio boom nell'impiego di turbine a gas nei diversi settori, è bene ricordare come il loro impiego nel settore aeronautico sia risalente già alla fine della Seconda Guerra Mondiale. La necessità di velivoli da guerra con prestazioni sempre maggiori, spinse i progettisti a ricercare soluzioni diverse all'adozione dei classici motori alternativi. La scelta ricadde sulle turbine a gas. I primi modelli sviluppati, adottavano semplici soluzioni tecniche con compressori radiali centrifughi e turbine assiali calettate sullo stesso albero. Il ciclo di lavoro operato all'interno della turbomacchina era un semplice ciclo Joule-Brayton aperto. Le limitate capacità resistenziali dei materiali alle alte temperature unite alle incomplete conoscenze in campo aerodinamico, nelle tecniche di raffreddamento e di regolazione, fecero sì che i rendimenti delle prime turbine a gas si arrestassero a pochi punti percentuali.

Negli anni immediatamente successivi al termine del Conflitto, esse videro accrescere il loro impiego anche nel settore della nascente aeronautica civile e in altri settori quali quello navale e del mechanical drive, fino a giungere ai giorni nostri, in cui rivestono un ruolo di fondamentale importanza.

All'inizio degli anni '50 l'azienda inglese Rover, immise sul mercato un prodotto destinato a riscuotere grande successo anche negli anni a venire. Infatti da quando la piccola turbina a gas ROVER1S/60 è stata commercializzata, numerosi sono stati i suoi usi e varianti. La ROVER 1S/60, mostrata in Figura 1, nacque dall'esigenza di realizzare un motore compatto e affidabile che fosse in grado di adempiere a diversi compiti, tra cui quello di mechanical drive per trascinare pompe o generatori di corrente, fino addirittura ad essere impiegato per la propulsione di piccoli velivoli civili.

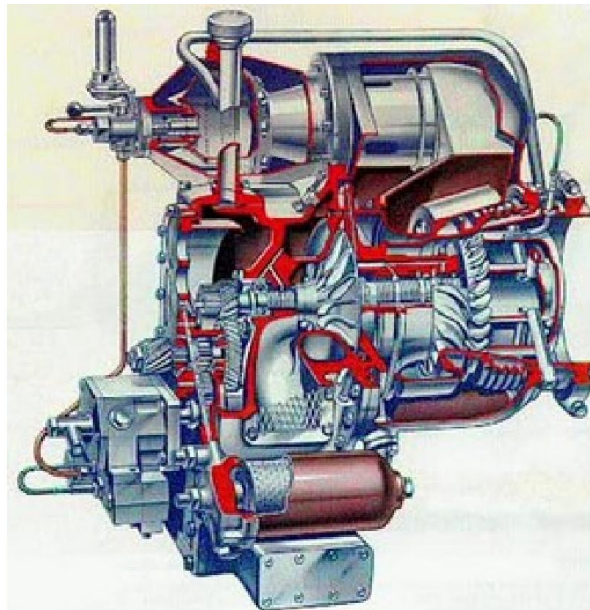


Figura 1 *Micro turbina a gas ROVER1S/60*

Sebbene oggi il mercato delle micro turbine a gas offra numerosi prodotti dalle caratteristiche tecniche e dimensioni molto più compatte, la ROVER 1S/60 si può certamente ritenere in assoluto una tra le prime micro turbine a gas mai commercializzate.

Il lavoro di Tesi svolto presso l'Università Tecnica di Vienna (TU WIEN), durante il periodo di scambio Erasmus è consistito nell'andare ad indagare per via sperimentale come le perdite di carico in fase di aspirazione (Δp_{01}) andassero ad influenzare le prestazioni della micro turbina a gas ROVER 1/60, alloggiata all'interno di un banco prova appositamente strumentato per lo scopo. Il banco prova allestito presso i laboratori di fluidodinamica delle macchine

della TU WIEN, viene impiegato comunemente a scopi didattici nel corso di Macchine.

Tutte le prove sono state condotte in corrispondenza di una velocità di rotazione all'uscita dell'albero riduttore di 2000 rpm, in luogo del valore nominale di 3000 rpm.

In una seconda fase, i risultati sperimentali sono stati confrontati con quelli forniti da un modello teroico appositamente sviluppato all'interno della TU WIEN.

La ROVER1S/60 basa il suo funzionamento su un semplice ciclo Jouyle-Brayton aperto (Figura 2), in cui l'aria aspirata viene compressa nel passaggio attraverso un singolo stadio di compressione centrifugo.

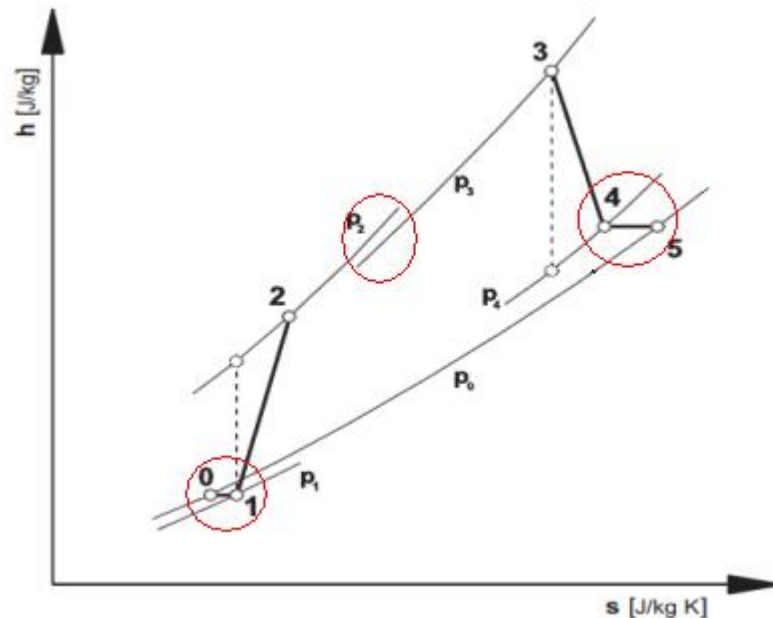


Figura 2 Ciclo Joule-Brayton operato dalla ROVER 1S/60. In evidenza le perdite di carico in fase di aspirazione Δp_{01} , combustione e scarico Δp_{04} .

La girante aperta del compressore con scarico radiale, ha il diametro di uscita che misura 165mm ed è realizzata in lega di Alluminio, garantendo in condizioni nominali un rapporto di compressione pari a 3,1 a 46.000 giri al minuto. In Figura 3 sono mostrate la girante radiale del compressore e quella assiale della turbina calettate sullo stesso albero.



Figura 3 Rotore della ROVERIS/60 con giranti di compressore e turbina calettate sullo stesso albero

L'aria compressa, dopo aver attraversato il diffusore palettato, viene convogliata nella camera di combustione in cui viene miscelata con il combustibile (Diesel) atomizzato. Al suo interno si verifica un processo di combustione turbolento, localmente stechiometrico, ma globalmente con grande eccesso d'aria. Ciò garantisce una combustione completa e contemporaneamente un controllo sulla riduzione della temperatura dei fumi in ingresso turbina. Il controllo sulla formazione degli inquinanti, e in particolare degli NOx termici non viene attuato al suo interno. Il passaggio dei gas attraverso il combustore avviene rapidamente, ma induce anche esso delle perdite di carico (Figura 2), che nel caso della ROVER 1S/60 sono state valutate in circa 80 mbar di caduta di pressione. Una volta espulsi dal combustore, i gas ad alto contenuto entalpico entrano in turbina, dove espandono, generando lavoro. Dapprima uno stadio statorico e poi quello rotorico, guidano l'espansione dei gas verso lo scarico.

La turbina è realizzata con una lega metallica alto resistenziale a base Nickel, policristallina. Nonostante le buone doti di resistenza alle alte temperature, la Temperatura di Ingresso in Turbina è limitata attorno ad un valor medio di 670 °C in corrispondenza di condizioni di funzionamento a carico parziale di 2000 rpm a valle del riduttore. La progettazione delle pale è avvenuta seguendo il criterio del Vortice Libero. Tale criterio, un tempo molto utilizzato per la sua semplicità applicativa, permette di ottenere dalla turbina un lavoro scambiato lungo l'altezza di pala costante.

Per quanto riguarda le perdite di pressione allo scarico Δp_{04} , seppur presenti ($\approx 0,2 \text{ mbar}$) sono state direttamente trascurate al momento della valutazione delle prestazioni globali della turbomacchina. Visto il loro ridotto valore, si è ritenuto possibile trascurarle.

La Tabella 1 mostra le principali caratteristiche della ROVER 1S/60 e le sue prestazioni in condizioni di funzionamento nominali.

Description	
Net power	45 KW
Thermal efficiency	13 %
Compression ratio	3,1
Rotor speed	46.000 rpm
Generator speed	3000 rpm
Compressor	Centrifugal impeller
Combustion chamber	Reverse flow single can with simplex burner nozzle
Turbine	Axial flow
Layout	Single spool with reduction gear
Ignition	High energy ignitor plug with air / fuel emulsion pump
Lubrication	Wet sump with pressure pump, water cooled oil cooler
Starting	Electric
Fuel	Diesel
Weight	63.52 kg

Tabella 1 *Prestazioni in condizioni di funzionamento ISO a 3000 rpm e principali caratteristiche tecniche*

L'obiettivo finale è stato quindi quello di valutare l'influenza delle perdite di carico in fase di aspirazione Δp_{01} sulla potenza e sul rendimento della ROVER 1/60, cercando al contempo di mantenere il più costanti possibili tutti gli altri parametri di ciclo. Per indurre perdite di carico concentrate in fase di aspirazione e contemporaneamente misurare la portata massica fluente nel ciclo, sono stati adottati tre diaframmi normati secondo la normativa EN ISO 5167-1 per i misuratori di flusso. Prima di addentrarsi più nel dettaglio della fase sperimentale è utile descrivere le peculiarità del banco prova adottato.

La Figura 5 mostra lo schema del banco prova strumentato, sito presso i laboratori del dipartimento di Macchine e Sistemi energetici dell'Università Tecnica di Vienna.

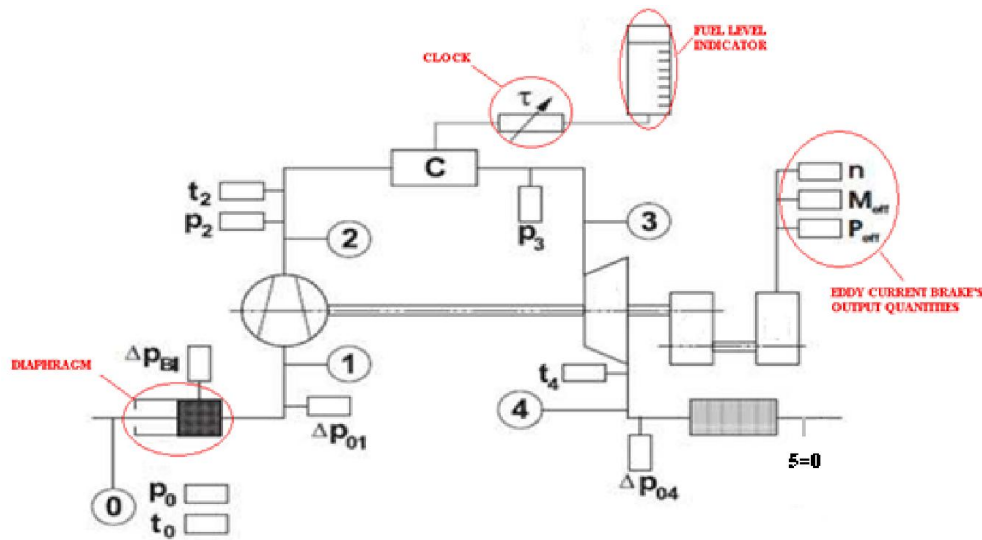


Figura 4 Banco prova allestito presso la TU WIEN

L'aria viene dapprima aspirata nel condotto di aspirazione dal diametro interno di 245mm, che presenta nella sezione di imbocco un diaframma per la misurazione della portata di aria in ingresso \dot{m}_{air} . La valutazione di portata d'aria è avvenuta misurando la perdita di pressione Δp_{BL} a cavallo del diaframma. Nell'attraversamento del condotto, fino all'imbocco del compressore (1), il flusso subisce ulteriori perdite di carico. La riduzione di pressione totale tra ingresso condotto di aspirazione e imbocco compressore (0-1), è stata acquisita con un secondo trasduttore di pressione differenziale Δp_{01} . Una volta compressa, viene quindi misurata la temperatura totale T_2 e la pressione statica assoluta p_2 con la quale l'aria entra nel combustore (2). Al termine della fase di combustione in (3), è stata misurata la pressione statica assoluta p_3 dei gas combusti pronti ad espandere in turbina. Viste le alte temperature in ingresso turbina, si è risaliti alla temperatura T_3 a posteriori basandosi su calcoli di natura Termodinamica e senza effettuare la misura diretta con l'ausilio di termocoppie.

Allo scarico della turbina (4) sono presenti quattro termocoppie dello stesso tipo K di quella utilizzata per misurare la temperatura T_2 . Le quattro sonde sono state disposte circonferenzialmente (Figura 6) così da permettere la misurazione della temperatura dinamica T_4 in quattro punti diversi ed eseguire successivamente una media dei valori ottenuti. I diversi valori registrati nelle quattro diverse posizioni angolari sono stati dovuti alla diversa distribuzione circonferenziale della temperatura a causa della posizione del combustore e della componente di Swirl dei gas combusti espulsi. La presenza di una valvola di sicurezza avrebbe

tagliato l'afflusso di combustibile, in caso di superamento del valore soglia $T_{4\max}=800^{\circ}\text{C}$.

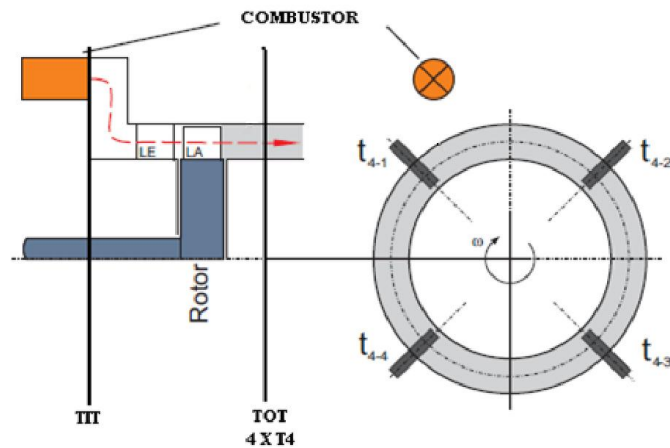


Figura 5 *Disposizione delle quattro termocoppie allo scarico della turbina*

Infine l'impianto è stato dotato di un trasduttore di pressione differenziale per misurare le perdite di carico allo scarico Δp_{04} . Come accennato in precedenza tali perdite sono state trascurate durante il procedimento di calcolo delle prestazioni del ciclo, in quanto di piccola entità e poco o per nulla influenti sulle prestazioni finali.

Per dissipare la potenza generata, l'albero della ROVER 1S/60 lato compressore, è stato collegato tramite una serie di ingranaggi a cascata, ad un riduttore di giri (rapporto di riduzione 15,33) e quindi ad un freno a correnti parassite 'Borghi&Saveri'. Oltre al compito di dissipare la potenza generata, il freno a correnti parassite è stato strumentato con una cella di carico ed un tachimetro con l'obiettivo di misurare grandezze quali coppia, numero di giri dell'albero riduttore in uscita e potenza netta istantanea erogata dal motore. Queste tre grandezze apparivano direttamente sul pannello sovrastante il banco prova. Su un secondo pannello era possibile visualizzare istantaneamente tutte le altre quantità sopra menzionate (Figura 6)



Figura 6 A sx pannello principale di controllo e acquisizione dati, a dx pannello acquisizione dati sovrastante il freno a correnti parassite

Nel corso delle prove sperimentali, sono stati impiegati tre diaframmi, ognuno avente una sezione di imbocco diversa (rispettivamente 169,5mm 140mm e 115,8mm), in modo tale da indurre perdite di carico concentrate crescenti al diminuire del diametro interno. Ogni diaframma è stato realizzato rispettando le indicazioni derivanti dalla normativa per i misuratori di flusso interni (tipo diaframmi) ad una condotta di lunghezza “infinita” EN ISO 5167-2 (Figura 7), e più in particolare si è fatto riferimento alla normativa VDI-VDE 2041 per quanto ha riguardato la correzione da attuare per i misuratori di portata posti all’imbocco di una condotta.

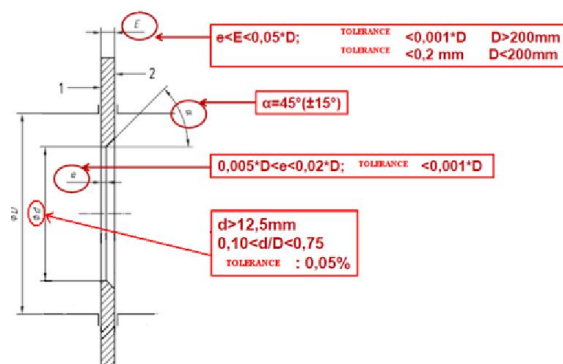


Figura 7 Diaframma-tipo utilizzato nei test riferito alla norma EN ISO 5167-2

Per ogni diaframma, sono stati condotti quattro test in condizioni di funzionamento differenti (Figura 8), ad una velocità costante di uscita riduttore di 2000 rpm. Il motivo per cui si è deciso di condurre i test a carico parziale e non con una velocità di uscita di 3000 rpm, è stato semplicemente quello di preservare l'integrità delle componenti rotanti, i cui ricambi, nel caso di danneggiamento sarebbero stati difficilmente reperibili. La regolazione del carico è avvenuta agendo direttamente sul sistema di controllo del freno a correnti parassite.

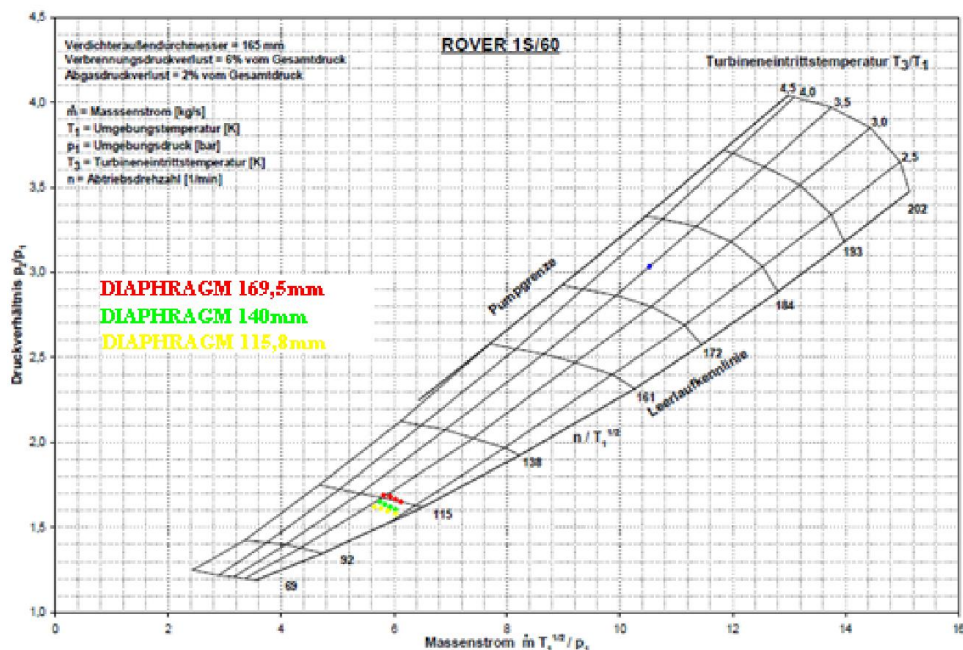


Figura 8 Mappa di funzionamento della ROVER 1S/60 e in evidenza le diverse condizioni di carico, corrispondenti ad ognuno dei tre diversi diaframmi

La procedura di acquisizione dati ha richiesto innanzitutto di misurare con strumenti manuali le condizioni di pressione e temperatura ambiente p_0 e T_0 . Tra un set di quattro prove e l'altro, la turbina a gas e tutto l'ambiente circostante sono stati fatti raffreddare per alcuni minuti, con l'obiettivo di ristabilire condizioni ambientali analoghe a quelle di partenza. La fase di run up ha richiesto molta cautela e in particolare l'albero di potenza della ROVER 1S/60 è stato mantenuto in rotazione da un motore elettrico, fino alla velocità di 4000 rpm. Superata questa fase iniziale, la turbina è stata in grado di grado di trascinare il compressore autonomamente. Oltre all'acquisizione delle grandezze sopra descritte, un ulteriore dato acquisito di fondamentale importanza, è stato il tempo impiegato per consumare un litro di combustibile. Ciò è stato possibile

cronometrando manualmente il consumo, reso visibile attraverso un serbatoio in vetro graduato (Figura 6).

Attraverso la successiva elaborazione dei dati acquisiti, si sono ricavati tutti i parametri di ciclo e quindi le prestazioni della ROVER 1S/60.

Le indicazioni sulle prestazioni della turbina a gas, fornite dal costruttore, sono valutate in corrispondenza delle condizioni ISO (3977-2) di funzionamento, ovvero:

- Temperatura ambiente: 15 [°C]
- Pressione ambiente: 101325 [Pa]
- Assenza di perdite di carico in aspirazione e scarico
- Combustibile Gas Naturale
- Macchina nuova e pulita
- Umidità relativa $p=60\%$

Tuttavia la maggior parte delle condizioni sopra riportate, non viene quasi mai rispettata nelle reali condizioni di funzionamento. Lo scostamento delle prestazioni dallo standard, avviene generalmente in seguito alla variazione singola o contemporanea di diversi fattori, tra cui temperatura ambiente, pressione ambiente, umidità relativa, impiego di altri combustibili, invecchiamento e sporcamento della palettatura, e infine presenza di perdite di carico lato aspirazione e scarico.

In questo caso l'obiettivo non è stato quello di valutare il decadimento delle prestazioni, in condizioni di funzionamento non-ISO, bensì l'oggetto della presente Tesi è stato quello di valutare l'impatto sulle prestazioni della ROVER 1S/60 delle perdite di carico in fase di aspirazione, mantenendo il più possibile costanti tutti gli altri parametri di ciclo. Tuttavia, vista l'impossibilità di condurre le prove rispettando il precedente vincolo, si sono dovute operare alcune ipotesi:

- 1) Tutti i test sono stati eseguiti nel corso della medesima giornata, che ha presentato condizioni atmosferiche stabili con impercettibili variazioni barometriche. Per questo motivo si è potuto assumere con ottima approssimazione che tra una serie di test e l'altra, la pressione p_0 si sia mantenuta stabile e costante.

- 2) La temperatura ambiente del capannone è risultata essere più alta al termine di ogni sessione di quattro test. Ciò è stato dovuto al calore immesso nell'ambiente mentre l'impianto si trovava in funzione. Per ovviare a questo problema, sono stati fatti passare alcuni minuti tra una sessione e l'altra, così da far tornare la temperatura interna al laboratorio ai livelli pre-test. Grazie a questo, si è potuto ritenere $T_0 = T_{amb} = \text{costante}$.
- 3) Per uno stesso diaframma, al variare del carico, la condizione di funzionamento (visualizzabile anche in Figura 8), è variata. Di conseguenza la TIT non si è mantenuta costante di test in test. Tuttavia si è deciso di considerare come TIT di riferimento in corrispondenza della quale valutare l'influenza delle perdite di carico, il valore intermedio $T_3 = 670^\circ\text{C}$.
- 4) Le perdite di carico allo scarico $|\Delta p|_{04}$ sono state ritenute trascurabili. In questo modo si è ipotizzata l'assenza di contropressione allo scarico.
- 5) Umidità relativa costante, per lo stesso motivo della costanza di p_0 indicata al punto 1.
- 6) Numero di giri in uscita dall'albero riduttore costante e pari a 2000 rpm.
- 7) Portata ridotta costante in corrispondenza di ognuno dei punti di carico, al variare del diaframma utilizzato.

La valutazione di un Δp_{01} medio per ognuno dei tre set di quattro prove, corrispondenti ai tre diaframmi, ha permesso di evidenziare il calo di potenza e di rendimento avvertito dalla ROVER 1S/60 all'aumentare delle perdite di carico in aspirazione.

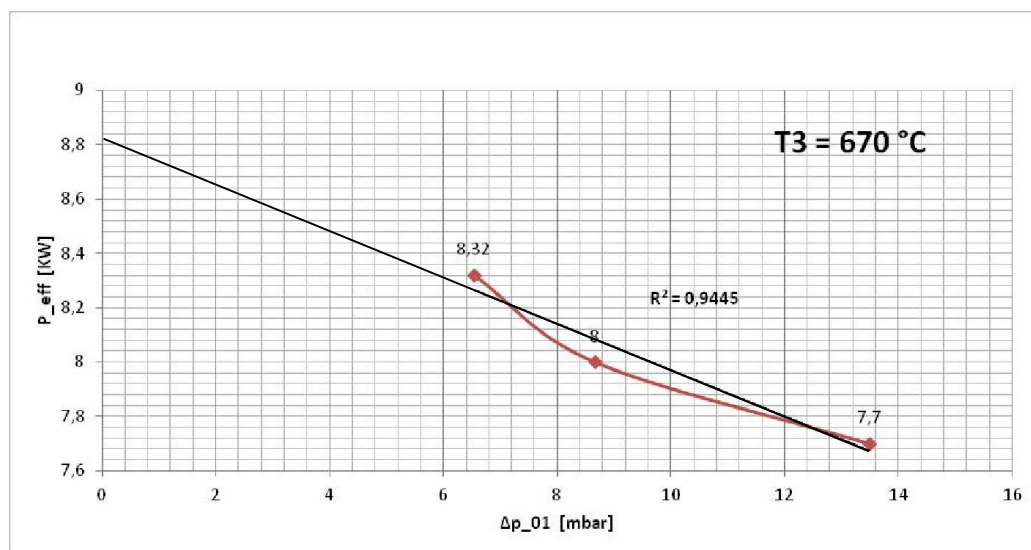


Figura 9 Calo della Potenza netta erogata dalla ROVERIS/60 all'aumentare delle perdite di carico in aspirazione corrispondenza di una TIT=670°C

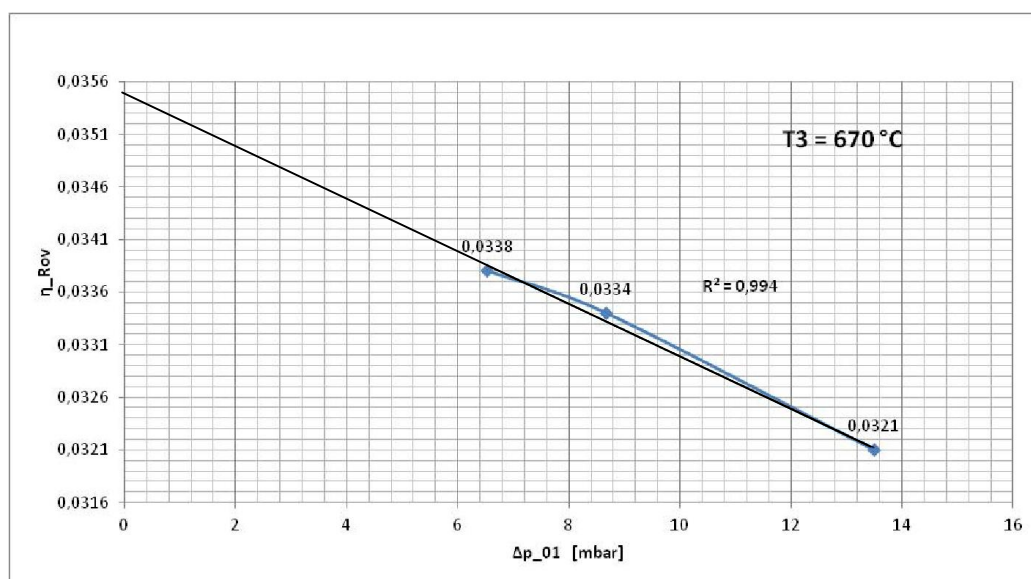


Figura 10 Calo di rendimento della ROVER 1S/60 all'aumentare delle perdite di carico in aspirazione, in corrispondenza di una TIT=670°C

Come si può vedere dalla Figure 9 e 10, la diminuzione di potenza e rendimento all'aumentare delle perdite di carico in fase di aspirazione, può essere ben

approssimata da una retta. Ciò consente anche di determinare il valore teorico di potenza e rendimento in assenza di riduzione di pressione all'aspirazione, semplicemente prolungando la retta fino ad intersecarla con l'asse delle ordinate.

Dalle due precedenti figure, si nota come i già bassi valori nominali di $P_{eff} = 46 \text{ KW}$ e $\eta = 0,13$, siano ulteriormente penalizzati dalle elevate perdite di carico indotte in aspirazione e dal ridotto regime di giri di 2000rpm all'uscita del riduttore, mantenuto in fase di prova.

Una volta ricavati ed elaborati tutti i dati sperimentali, è stato possibile eseguire il confronto con i risultati forniti da un semplice modello teorico sviluppato all'interno della TU WIEN.

Il modello analitico è fondato su alcune ipotesi fondamentali. Oltre alle ipotesi sopra riportate sono state effettuate ulteriori assunzioni:

- C_p costante lungo tutto il ciclo termodinamico
- Rapporto di espansione in turbina influenzato unicamente dalle perdite di carico in fase di aspirazione

Da ciò segue che, il lavoro netto compiuto dalla ROVER 1S/60 può essere espresso come:

$$W_N = \eta_{T_{is}} c_p^T T_3 \left(1 - \Pi_T^{\frac{1-\gamma}{\gamma}} \right) - \frac{1}{\eta_{C_{is}}} c_p^C T_1 \left(\Pi_C^{\frac{\gamma-1}{\gamma}} - 1 \right)$$

E quindi

$$\frac{W_N}{c_p T_1} = \eta_{T_{is}} \frac{T_3}{T_1} \left\{ 1 - [(1 - \xi) \Pi_C]^{\frac{1-\gamma}{\gamma}} \right\} - \frac{1}{\eta_{C_{is}}} \left(\Pi_C^{\frac{\gamma-1}{\gamma}} - 1 \right)$$

In cui $\xi = \frac{|4p_{01}|}{p_0}$ rappresenta il contributo alla diminuzione del rapporto di espansione in turbina, dovuto dalle perdite di carico in fase di aspirazione.

Le espressioni finali a cui il modello consente di giungere, permettono di trarre considerazioni importanti, riassunte nelle seguenti equazioni:

$$\frac{P_{Rover}}{P_{Rover}|_{\xi=0}} = 1 - (1 - \alpha)\xi$$

$$\frac{\eta_{Rover}}{\eta_{Rover}|_{\xi=0}} = 1 + \alpha \xi$$

Dalle precedenti due equazioni, risulta evidente come l'andamento dei rapporti di potenza e rendimento, sia di tipo lineare. Inoltre, il coefficiente angolare che pesa il contributo delle perdite di carico in fase di aspirazione risulta essere maggiore nel caso della potenza. Per questo motivo il modello consente di trarre la prima importante conclusione: la diminuzione di pressione in fase di aspirazione penalizza in minor quantità il rendimento.

Dal confronto con i rapporti di potenze e rendimento ricavati sperimentalmente (Figure 11 e 12) si evince che i risultati sperimentali, si dispongono anch'essi con buona approssimazione secondo una linea retta, passante per il punto (0;1) in corrispondenza di assenza di perdite di carico in aspirazione.

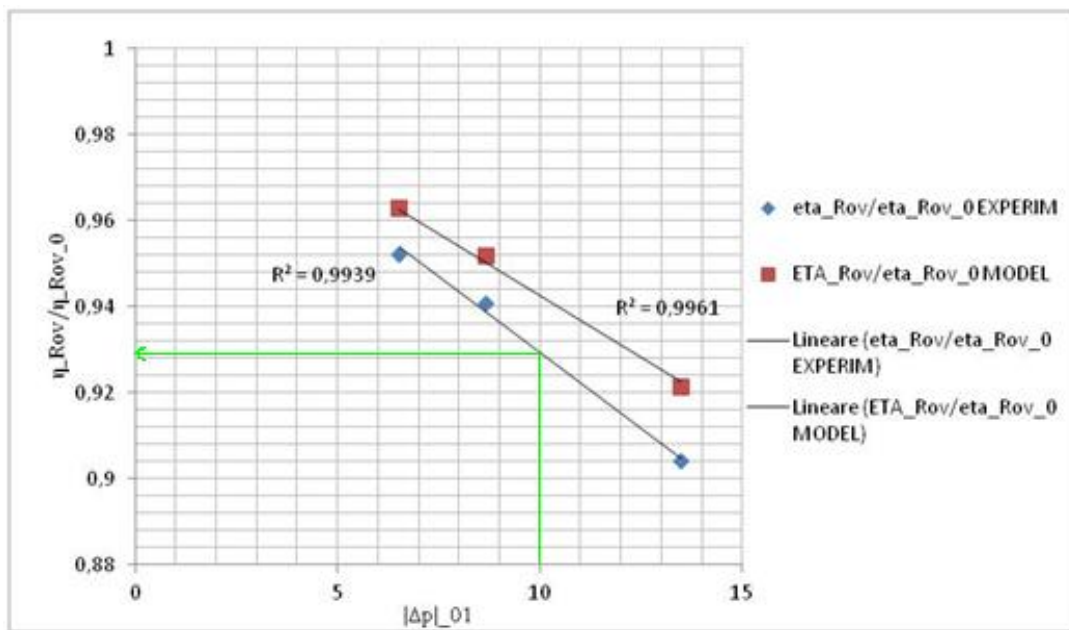


Figura 11 Andamento del rapporto di rendimenti al variare di $|\Delta p|_{01}$ derivante dall'analisi sperimentale e da quella con modello

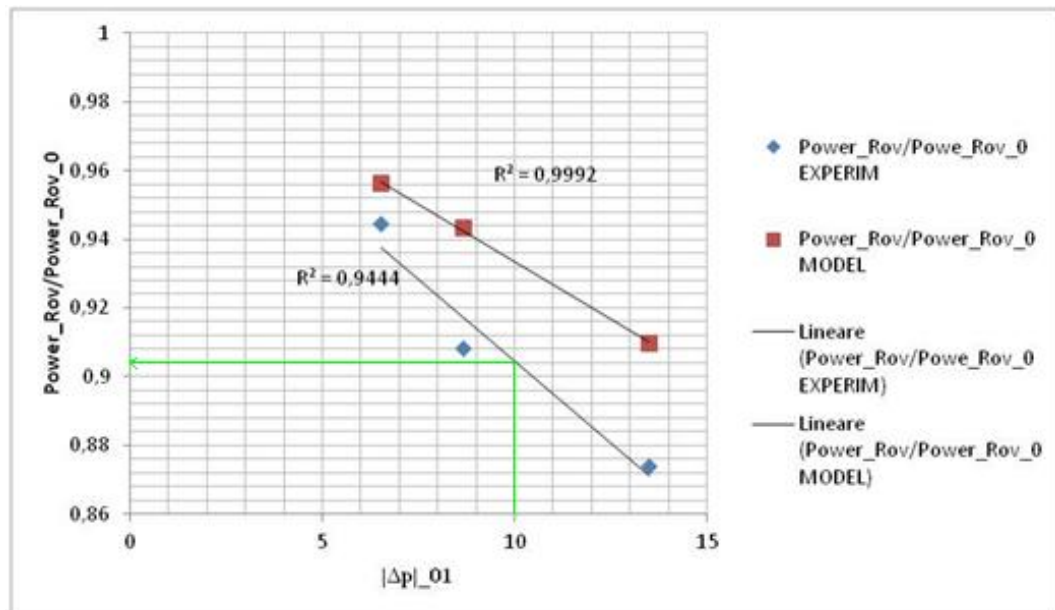


Figura 12 Andamento del rapporto di potenze al variare di $|\Delta p|_{01}$ derivante dall'analisi sperimentale e da quella con modello

I risultati sperimentali mostrano un calo delle prestazioni più marcato, dovuto agli effetti reali di cui non si è tenuto conto nel modello teorico.

Infine dal confronto con i risultati sperimentali ottenuti per una grande turbina a gas heavy duty GE MS7001EA [15], si è potuto constatare che in corrispondenza di un valore di perdite di carico in aspirazione uguale a 10 [mbar], il calo delle prestazioni in termini percentuali di rendimento e potenza è stato rispettivamente dello 0,7% e 1,8%, contro valori di 7% e 8,7% registrati per la piccola ROVER 1S/60 (Figura 13). Questo permette di affermare in prima approssimazione che le grandi turbine a gas risentono meno del calo di prestazioni rispetto alle turbine a gas di taglia inferiore.

Il presente lavoro di Tesi, non ha avuto la pretesa di fornire tramite l'utilizzo di un semplice modello analitico, dati quantitativamente rilevanti per un suo impiego generalizzato, bensì ha permesso di giungere a conclusioni valide sotto un profilo qualitativo. L'applicazione di tutte le condizioni al contorno inserite nel modello, è stata resa possibile grazie ai ridotti valori di rapporto di compressione e TIT raggiunti all'interno del ciclo termodinamico operato dalla ROVER 1S/60..

I successivi sviluppi andranno nella direzione della creazione di modelli più raffinati, che tengano conto del contemporaneo effetto di un maggior numero di fattori penalizzanti le prestazioni. Tuttavia, nonostante i limiti sopra esposti, i risultati raggiunti in questo lavoro possono ritenersi soddisfacenti, essendo un valido strumento a disposizione dei futuri studenti, per migliorare la comprensione dei complessi fenomeni fisici che avvengono all'interno di una turbina a gas.

Chapter 1

Introduction

Nowadays it would be unimaginable to have a society without electricity and airplanes, that move us all around the globe quickly and safely. The extraordinary machines which permit us to live during evenings as though it were daytime, also allowing us to be warm during winter and cool during summer, or to fly fast through the sky, thousands of meters above the ground, all come from a common explanation called: Turbogas Machines. They represent a real challenge for the present and future engineers. Due to their complexity, they require large effort to maintain the high reliability and off project performance.

The Brayton-Joule cycle, that is the basis of their functioning, has been described first in the second half of 19th century; however technological limits in metallurgy, steel industry and of course in Aerodynamics, never allowed for the development of fully functioning prototypes consisting of continuous flow turbogas machines until the beginning of the 1930's. Gas turbines have been used for many years in different fields and for many different purposes. We use them to power aircrafts as well as in energy power plants and to drive various mechanical systems. Thanks to their high specific power and small size, they have been employed since the early fifty's to drive small devices, such as pumps and electricity generators for common or emergency scopes.

1.1 General contents

This final Thesis project work is going to show you how the performance of a micro early fifty's gas turbine is conditioned by small Inlet Pressure Losses, voluntarily created with three different orifice plates. The machinery behavior and its thermodynamic cycle performance have been investigated, starting with the inlet duct's throat to the exhaust pipe duct. All tests have been carried out inside TU WIEN laboratories during my Erasmus Student Exchange Program, adopting a totally equipped and customized test bed, generally used for students training purposes. The test bed was equipped with a mass flow measuring system, pressure transducers and thermocouples. The system allowed to control the ROVER 1S/60 gas turbine fuel consumption and an eddy current brake system permitted to measure the number of shaft revolutions, torque and net

power outputs. Figure 1.1 represents ROVER 1S/60 and its thermodynamic cycle.

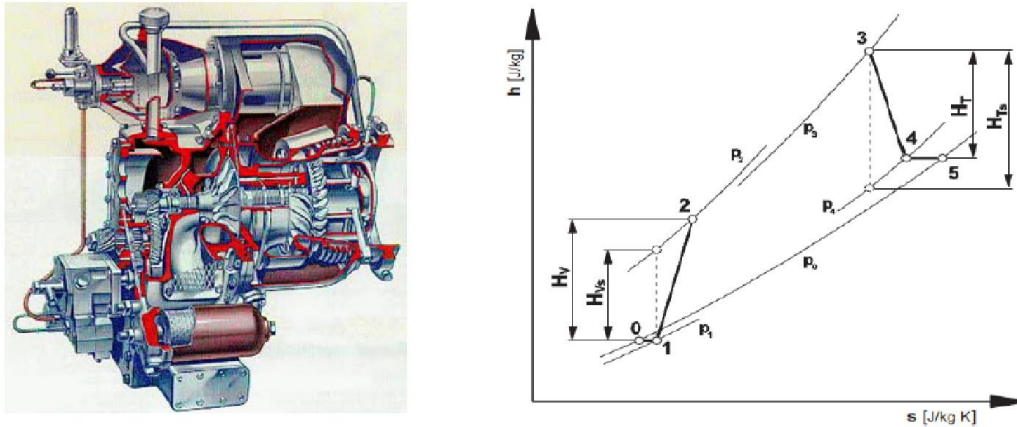


Figure 1.1 *ROVER 1S/60 and simple Brayton_Joule cycle performed by*

Several configurations were tested each one four times, in order to get enough data and verify the repeatability of tests. After a detailed data analysis the data obtained was compared with the equivalent data calculated from a theoretical model. The model (described in chapter 6) properly describes the way inlet pressure loss influences the gas turbine efficiency and power.

1.2 Small gas turbines

The advance in technology, especially in Aerodynamics and Metallurgy, has permitted the impellers and blades to be smaller, more efficient and more heat resistant. ROVER 1S/60 is one of the first small gas turbines launched on the market after the second World War. For decades, its strength and multi-capability uses, has made it a versatile machine with many different purposes. Nowadays markets offer a lot of small gas turbine models for steady state and jet propulsion applications.

1.2.1 An historical background

The first small gas turbines tested after the second World War; induced engineers to transform and improve the earlier 1930's gas turbine prototype used in aircraft engines: one of the most pioneering engineer was Sir Frank Whittle who design the first jet engines for military purposes. The piston engine was not powerful enough to supply the requirements of modern airplanes which required

more consistent power, combined with light weight and speed. Initially, engineers faced a lot of difficulties due to lack of sufficient power generated by the turbine. This was because of the low efficiency of compressors and the low TIT that the first turbine stages could withstand. The work required to drive the compressor is a large fraction of the total work output of the turbine. The most efficient turbomachines available to the early gas turbine engineers were centrifugal compressors and axial turbines as shown in figure 1.2.

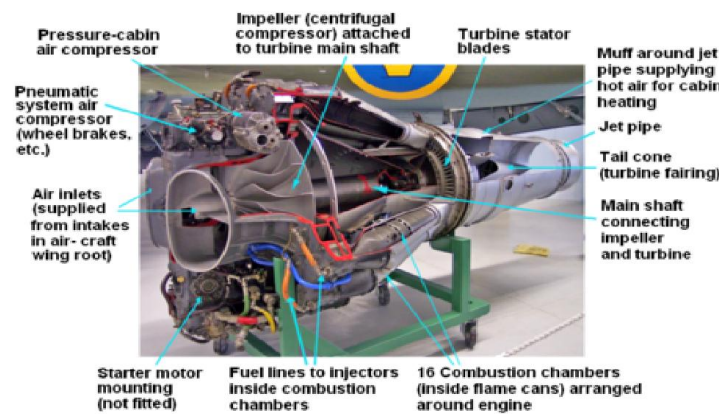


Figure 1.2 *Centrifugal- axial early gas turbine*

As reported in [1], radial turbomachine is, by virtue of the radius change across the impeller, capable of higher specific work transfer than an axial machine of the same speed and mass flow rate. However, the flow undergoes turning in two directions simultaneously and the scope for aerodynamic losses is greater. For early gas turbines operating at cycle pressure ratios up to about 6, a single stage centrifugal compressor was sufficient, just like in ROVER 1S/60. As the desire for better engine efficiencies drove cycle pressure ratios higher, one stage become insufficient, and the multistaging of centrifugal compressors, at least for aircraft applications became unattractive because of the tortuous gas path between stage and the additional size and weight of the necessary ducting.

Nowadays, for the smaller gas turbines of light aircraft, helicopter, scale models, automotive propulsion and auxiliary power generators, the single-stage centrifugal compressor holds its place. On the contrary, an axial turbine stage can support a greater pressure and Hentalpy ratio before the flow breaks down when compared to an axial compressor stage, so that the benefits of a centripetal turbine for this application are relatively smaller. However, in small sizes the axial turbine stage blades have to be made very small and numerous, so that the wetted area and hence the friction losses increase, as do blade blockage effects. Most significantly, the running clearance necessary between the blade tips and the case becomes a significant fraction of the height, and tip leakage losses can be quite severe. The problems and expense of manufacturing are also increased,

and all of these factors together make the radial turbine a strong contender for small gas turbine engines which work in dirty environments and pulsating flow fields such as in internal combustion engines' turbocharger systems. Despite that, today as in the past, the axial stages have been used in small and micro gas turbines; the reason is that they are not required to perform at high efficiencies, but only to guarantee a positive net power.

Chapter 2

The ROVER 1S/60

Can be described as a small, functional, simple, single rotor shaft turbomachine designed for many different tasks.

2.1 Overall features

The ROVER 1S/60 is a single shaft early 1950's designed with small compressor and turbine components, produced by Rover (Figure 2.1) to supply power to other machines or, sometimes, to thrust light aircrafts.

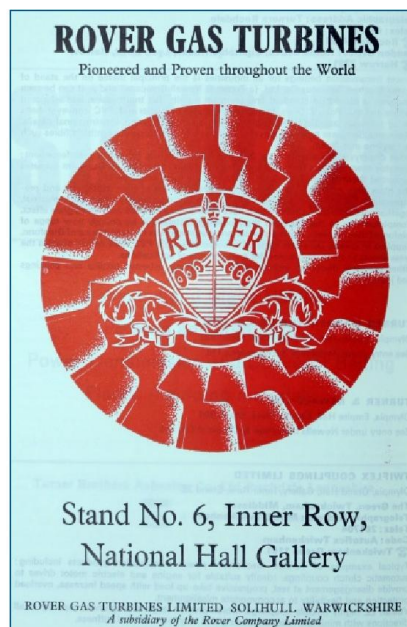


Figure 2.1 *Emblem of Rover's company*

Another variant of the engine was tested in the Rover's jet car "JET 1", which was first shown to the press at the Silverstone race track in 1950. It was also

used as a fire fighting water pump. At the time no other engine found as many applications (see Table 2.1). Its small size combined with an high-level reliability made this machine popular all over the world.

ROVER turbine	IS	Series	gas	APPLICATIONS
Rover 1S/60				Lucas Aerospace Lightweight Ground Power Unit
Rover 1S/60				Fire pump with hand starting
Rover 1S/60				Instructional gas turbine
Rover 1S/60				APU Argosy Aircraft
Rover 1S/82				Vulcan B2 APU
Rover 1S/90				Fighting ships auxiliary gen set
Rover 1S/90				Hovercraft APU
Rover TP/90				De Havilland Chipmunk Aircraft Propulsion Engine

Table 2.1 *Some applications of Rover 1S series*

As detailed in Figure 2.2, the ROVER 1S is made by a single shaft and cannular combustion chamber, with a single stage centrifugal compressor and a single stage axial turbine.

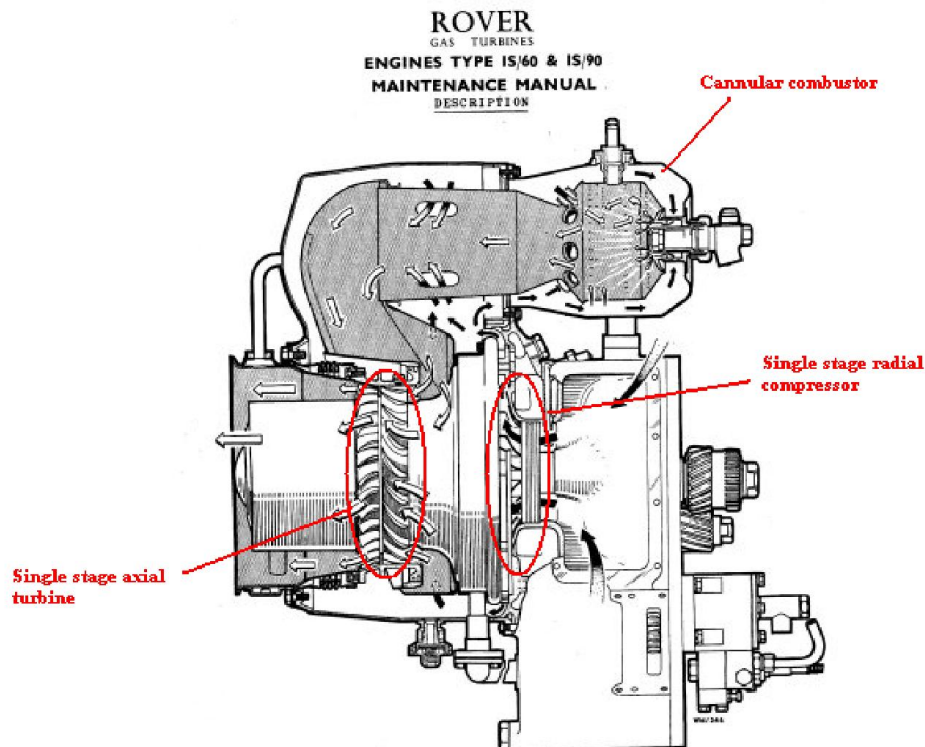


Figure 2.2 *Radial compressor-axial turbine and gas flow diagram*

Rover's thermodynamic cycle is a Joule-Brayton open cycle, without intercooler and afterburning systems. The very simple design, the low mechanical and thermal stress resistant materials and the need for high reliability performance, contributed to reduce the total machine efficiency.

Furthermore the efficiency was reduced by the undesigned functioning conditions, aging and fouling phenomena.

Due to the small impeller's size, the shaft rotational speed is quite high (46000 rpm) which transfers the highest quantity of energy to the working fluid. The real work transferred from the fluid to the rotor blades or contrary from the rotor blades to the fluid, is called Eulerian work and as explained in (Appendix A1) it depends on peripheral rotor speed U and on the component of absolute velocity V acting in peripheral direction. In Table 2.2 some important specification are reported:

Description	
Net power	45 KW
Thermal efficiency	12-13 %
Rotor speed	46.000 rpm
Generator speed	3000 rpm
Compressor	Centrifugal impeller
Combustion chamber	Reverse flow single can with simplex burner nozzle
Turbine	Axial flow
Layout	Single spool with reduction gear
Ignition	High energy ignitor plug with air / fuel emulsion pump
Lubrication	Wet sump with pressure pump, water cooled oil cooler
Starting	Electric
Fuel	Diesel
Weight	63.52 kg

Table 2.2 *Rover 1S/60 specification*

2.2 Main components

The next paragraph will describe which are the main Rover components and why such a simple machine outline has permitted such an engine to be an essential component in many applications.

2.2.1 Compressor stage

In gas turbomachines the work adsorbed by the compression phase is the same order of magnitude as the expansion work, this is due to air that is a compressible working fluid. During the compression phase, air is compressed and pushed out of the compressor stage into the combustion chamber, but to do this, the working fluid must go in the opposite pressure gradient direction. This means that surge phenomenon can occur. Surge is a sudden periodic return flow of the compressed fluid through the compressor into the inlet. It is usually clearly audible and represents a limit to the minimum mass flow rate. Prolonged operation in the surge cannot be tolerated as it can lead to mechanical failure, vibrations and possible interruption of the combustion process that the air supply is supporting. At the other extreme the maximum mass flow rate is limited by the phenomenon known as choking. This occurs when a local velocity, usually in the vaned diffuser or impeller throat, becomes equal to the acoustic velocity, [1]. A feature which the compressor design is often concerned with is to maximize the flow range between surge and choke, and in some applications efficiency may be sacrificed in order to gain this flow range.

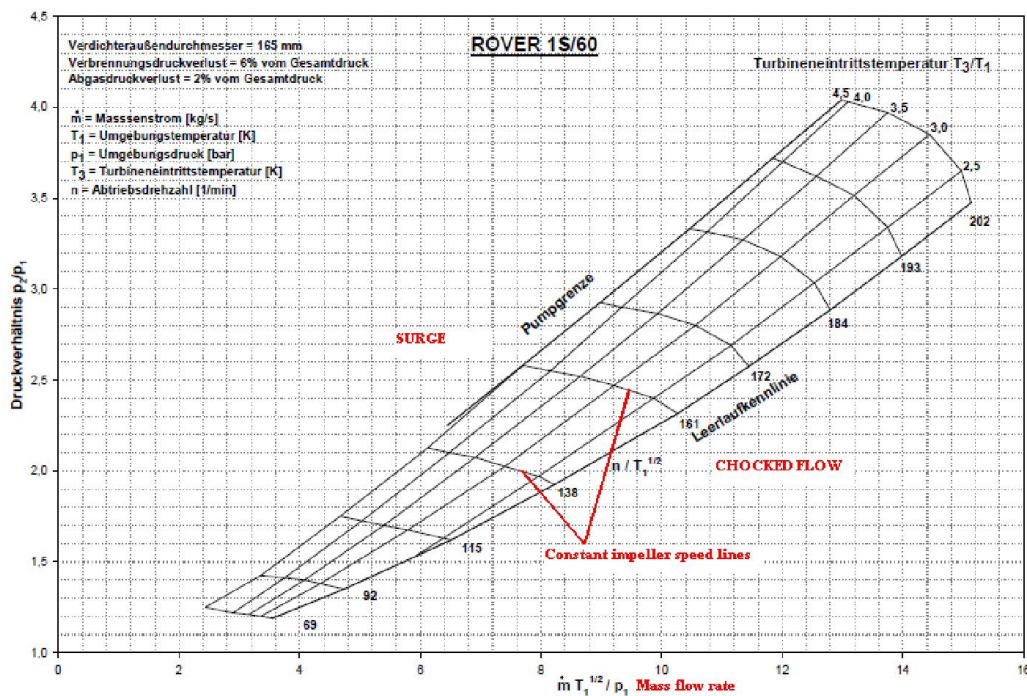


Figure 2.3 Surged and choked regions pointed out into the performance map

Furthermore, due to pressure increasing and temperature rising, this entails an extra work from the turbine in order to face the air expanding tendency. This thermodynamic phenomenon is shown in Appendix A2 and is named Reheat.

The compressor in the compressor housing is a single stage, 0,5 degrees of reaction, centrifugal unit and consists of 17 guide vanes impeller machined from an aluminium alloy forging. The impeller design is made by radial blades (Fig.2.5), and an outer diameter of 165 mm. The intake flow can be assumed to be not prewhirled so that the inlet velocity triangle is a simple right angle triangle.



Figure 2.418*Rover's rotor*

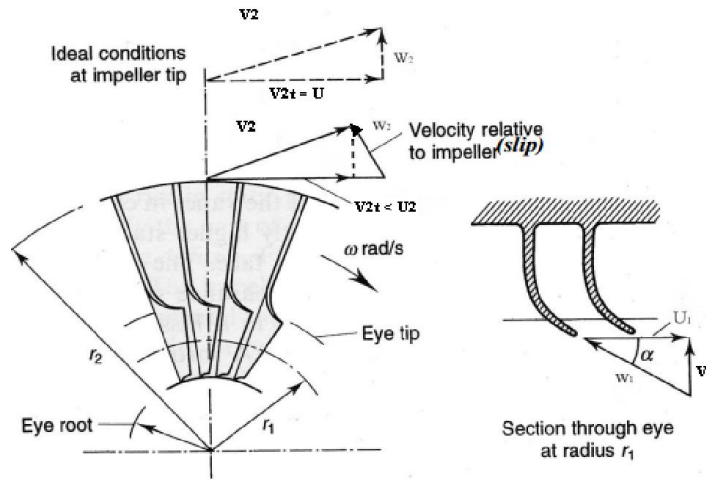


Fig 2.5 Radial blades geometry, [1]

However, the flow, cannot be perfectly guided by a finite number of blades and it is said to slip , leading to the modified velocity triangles shown in Figure 2.5. The effect of slip is to reduce the magnitude of the tangential component of velocity from that which is ideally attainable. This then has the effect of reducing the delivered pressure ratio, thus the impeller must be larger or run at higher speeds in order to deliver the required pressure ratio. This leads to increased stress levels and to increased relative velocities in the impeller, which will then give rise to increased friction losses and a reduced efficiency. The relative flow leaving an impeller, will not be perfectly guided by the blades even under ideal frictionless flow conditions. The classical explanations for slip phenomenon uses the concept of relative eddy, as the interblade flow which rotate with an angular velocity equal and opposite to the impeller. As reported in Osnaghi [2], for radial blades, Stodola (1927) suggested the following μ slip factor :

$$\mu = 1 - \frac{\pi}{N_B} \quad (2.1)$$

Where N_B is the number of blades. Buseman and Stanitz, upon theoretical analyses of the ideal fluid flow suggested another equation satisfactory for blade angles β_{2g} in the range of -45 up to +45 degrees

$$\mu = 1 - 0.63 \frac{\pi}{N_B} \quad (2.2)$$

As you can see in equation (2.1), Stodola's correlation is slightly less positive than the Buseman and Stanitz's one. Numerous other empirical correlations have been developed in an attempt to allow for flow separation in the impeller.

The compressor stage is also formed by the diffuser: it is clear that the fluid discharges from the impeller at high velocity, and consequently it is necessary to convert the kinetic energy efficiently into static pressure. Rover engineers opted for a vane diffuser which is often adopted since its higher pressure rise and higher efficiency at optimum operational point. On the contrary unvaned diffusers are preferred thanks to their simplicity and inexpensive construction, their broad operating range and their ability to reduce a sonic absolute velocity to a subsonic one without the formation of shock waves.

Figure 2.6 represents the flow at entry to the diffuser and its high complexity, consisting in unsteady jets and wakes issuing from each passage of the impeller.

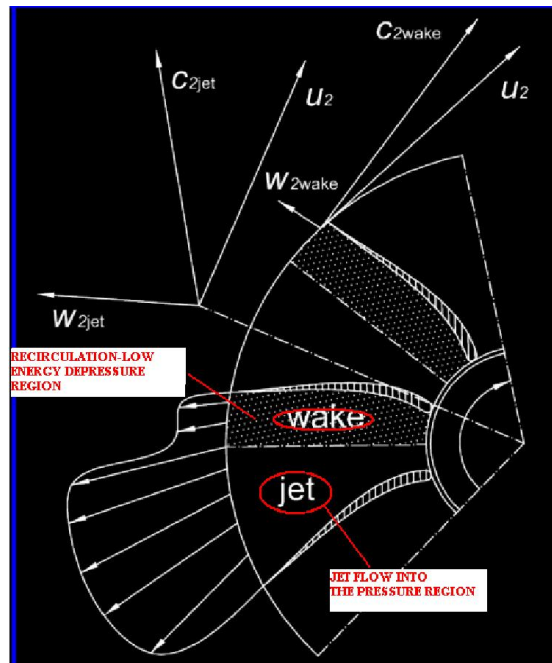


Figure 2.6 *Interblade Jet&Wake flow*

The ROVER 1S/60's compression ratio is about 3.1 in correspondence to the optimum operating point. However during the tests the machine was run at a lower speed in order to preserve the structural integrity, and for this reason the mean compression ratio dropped to a mean value of 1.6.

2.2.2 Combustion Chamber

The ROVER 1S/60 presents a single tubular combustion chamber with a cylindrical liner mounted concentrically inside a cylindrical casing. In the liner a diffusion flame takes place (also called non premixed flame) which consists in two reactant streams separated at the entry to the combustor. Mixing and combustion occur at the same time at the interface between the oxidizer and fuel.

The gas turbine combustion is often considered a steady flow process in which a hydrocarbon fuel is burned with a large amount of air excess to keep the Turbine Inlet Temperature at an appropriate value. The first combustion chambers that were designed, by ROVER engineers, were not equipped with any antipollution systems and the DLNOx mechanisms were not adopted as well.

The Figure 2.7 shows the different parts of a gas turbine combustor:

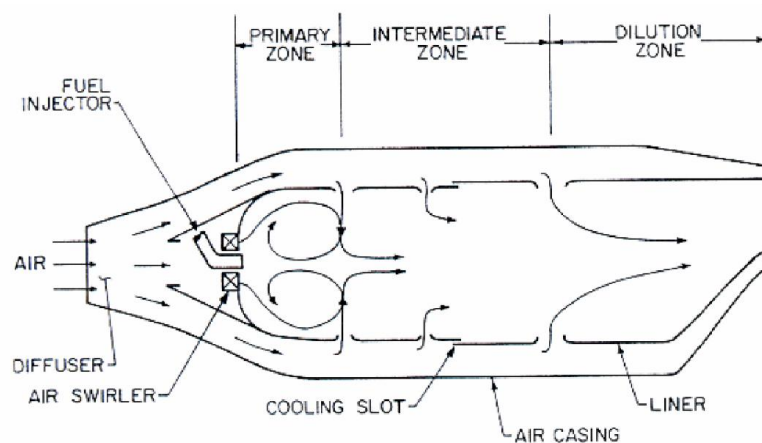


Figure 2.7 *Gas turbine's combustion chamber*

As mentioned in the previous paragraph, the function of the diffuser is to reduce the velocity of the combustor air inlet to a value at which the combustion pressure loss is acceptable and to recover as much of dynamic pressure (Total pressure) as possible. This permits the pressurized air to go into the liner with a smooth and stable flow. The purpose of the primary zone is to anchor the flame and turbulence to achieve the complete local stoichiometric combustion of the fuel at the interface between fuel and oxidizer. In order to avoid the blades melting, lean combustion takes place in the combustor (Figure 2.8).

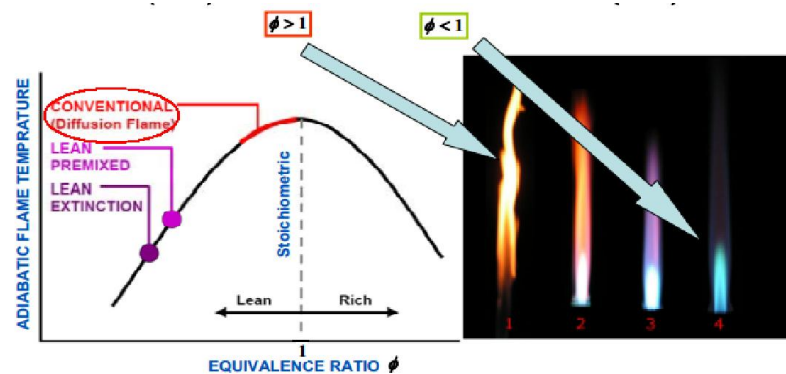


Figure 2.8 *Lean vs. rich combustion*

An essential feature is the toroidal flow reversal (Figure 2.9) that is maintained by air entering through swirl vanes (Figure 2.10), located around the fuel injector and through a single row of holes in the wall of the liner. This flow reversal ensures that some of the hot gases produced in combustion are recirculated back into the primary zone to mix with the incoming air and fuel. This marked swirl effect, contributes to make the circumferential temperature distribution irregular and so producing different values from the four thermocouples.

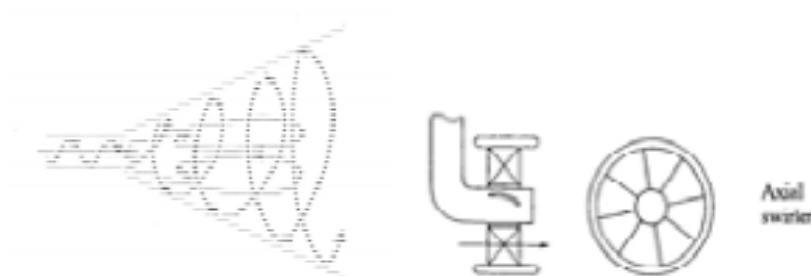


Figure 2.9 *Toroidal flow and axial swirler*

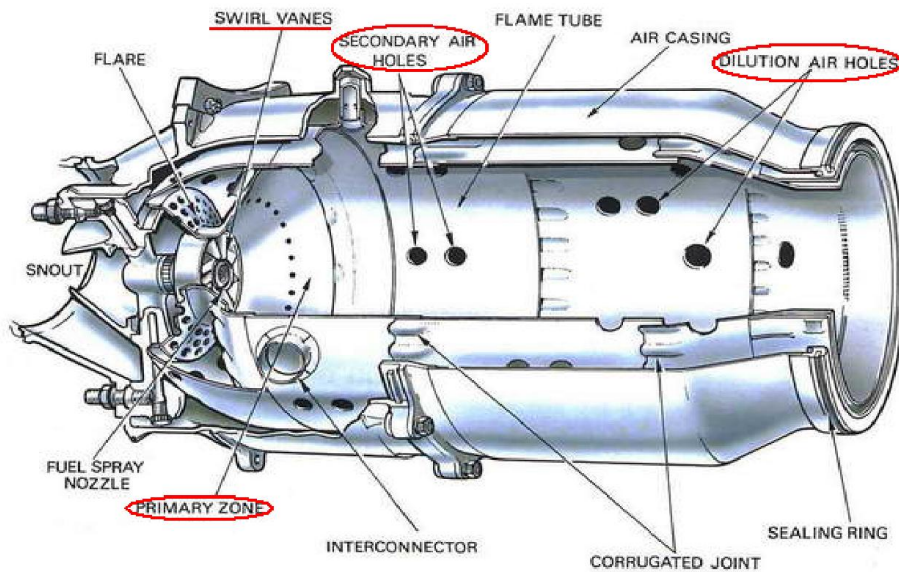


Figure 2.10 *Typical combustion chamber*

The secondary zone is the region that lies between the primary and dilution zones. At low combustion pressures, the rate of chemical reactions is slow and the combustion is far from complete at exit from Primary zone. Under these conditions, the Secondary zone serves principally as an extension to the primary zone, providing increased residence time for combustion to proceed to completion. At high pressure it ensures complete combustion, lowering the flame temperature by injecting prudent amounts of air.

In current combustion chamber, the last component is called “Dilution zone” and it provides to make the very hot gases colder, respecting the TOT restriction. In fact exceedingly hot gases could irreparably damage the uncooled turbine stage. However, the ROVER 1S/60’s combustion chamber does not have the dilution zone. The mean TIT measured value for each diaphragm is approximately 670 °C.

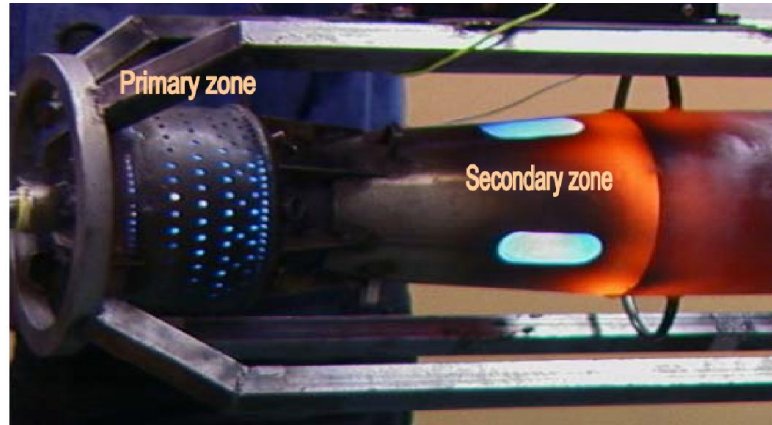


Figure 2.11 *ROVER 1S/60's combustor [3]*

During our data acquisition process we measured the absolute inlet and outlet combustor pressure with absolute pressure transducers. As previously suspected, the pressure dropped by a mean value of 80 [mbar] between the inlet and the outlet sections, due to the internal combustion chamber losses. In fact in an actual cycle there is some slight pressure loss in the combustion system and, hence, the pressure at point 3 is slightly less than at point 2.

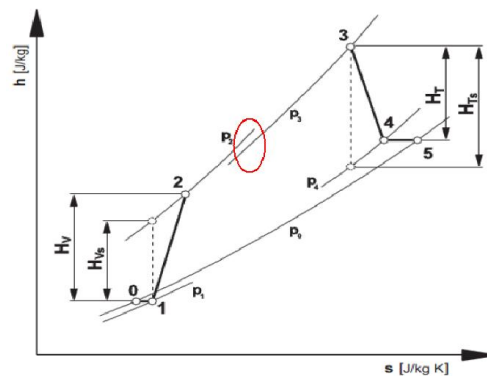


Figure 2.12 *Internal combustor pressure losses*

As the objective of the tests was to measure the data so as to evaluate the influence of inlet pressure loss on power and efficiency, but the pollutant combustor emissions was not take into account.

2.2.3 Turbine stage

After the combustion phase, the hot gases from the combustion chamber enter through volute to the 0.3-0.4 degrees of reaction turbine stage, where gases expand first in the stator and then into the rotor. The turbine impeller is an uncooled Nimonic forging in which blades and disk are machined integrally. The blades are of Free Vortex design and multi-crystal structure. In the Free Vortex design, the law of variation of the swirl velocity is given by the Free Vortex conditions (equations 2.2 and 2.4) and this imposes a certain change of nozzle angle with radius. As mentioned in Osnaghi [2]:

$$rV_t = \text{const} \quad (2.3)$$

$$V_a = \text{const} \quad (2.4)$$

E.A. Simonis and J.Reeman's studies [4] have suggested although the Free flow Vortex conditions do impose some twist on the stationary nozzles, they are convenient to take as a basis of design because of this constancy of work done. The big advantage of this design is that the work output is constant at all radii and there is no shed vortex from the blade. Most of the early designs were based on this Free-Vortex design concept. This is an advantage for the blade momentum stress resistant capability: when radius increases, the difference $V_{1t} - V_{2t}$ decreases giving a small momentum stress on the tip. Even though the loss due to shed vortex is eliminated, the hub wall losses are likely to be higher.

The following technical drawing has been given by TU WIEN and shows the turbine stage section.

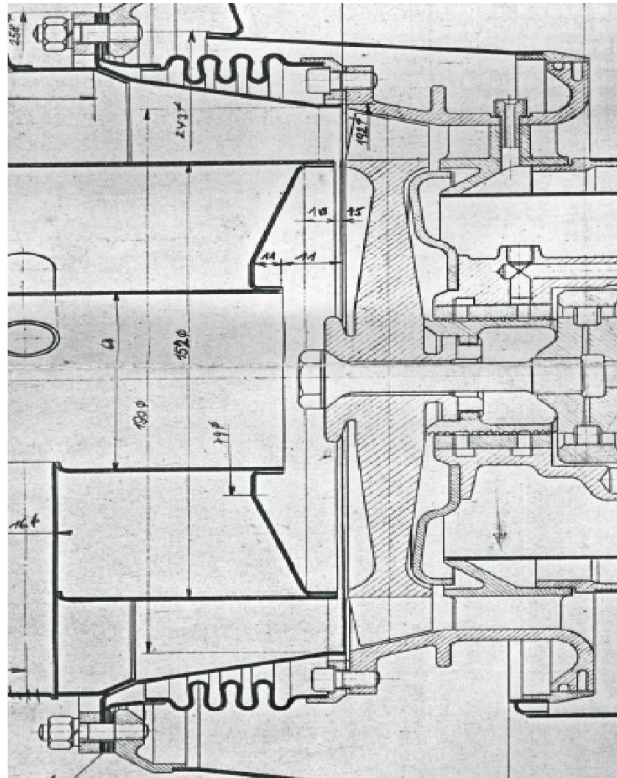


Figure 2.13 *Section of the ROVER's turbine stage*

The multi crystal Nimonic alloy turbine blades, permit it to withstand high TIT. Nowadays this technology is obsolete and new high performance single crystal Nimonic alloys, permit turbine blades to reach higher TIT (thanks to improved creep resistant capability) and consequently higher power and efficiencies. Finally, the ROVER 1S/60 engine has an axial diffuser and a 3000 rpm reduction gearing. The turbine output pinion in the centerline of the compressor and turbine assembly protrudes outward from the meshed gears. The output pinion rotates counter clockwise when viewed from the rear of the ROVER 1S/60 engine.

All those characteristics made this machine well known in many countries and adopted for many purposes, making it very sought after.

Chapter 3

The Test Bed

Test beds have for many years permitted the study of different physical phenomena and to obtain useful experimental data. Nowadays computed and numerical analysis supply almost all the necessary data to describe complex phenomena, but still in many applications experimental tests find their usefulness, especially in university laboratories for educational purposes.

3.1 The TU WIEN's test bed

All the tests, have been carried out at the TU WIEN laboratories on a special test bed built for student education. Previously, it was fitted with analogical equipment which was quite obsolete and with high unsensitive transducers but thanks to TU student Markus Januschewsky's final Master Thesis work [5] it was modernized in 2009 and equipped with a new eddy current brake system. These new digital transducers permit the results of the data to be acquired faster, making their readings easier. The main test bench components are:

- Inlet duct and diaphragms
- Absolute and differential pressure transducers
- Thermocouples
- ROVER 1S/60 gas turbine
- Eddy current brake system and gear box
- Chimney

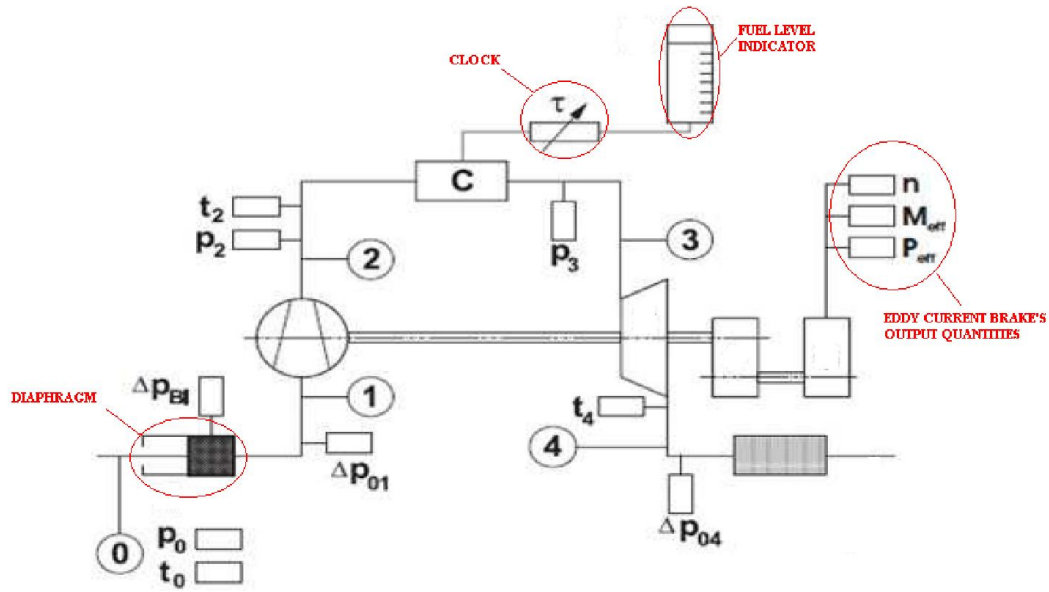


Figure 3.1 Scheme of TU WIEN's test bed

First of all ambient p_0 and T_0 have been assessed making use of hand instruments. Thanks to stable weather conditions, static pressure p_0 kept constant throughout the tests, on the contrary static temperature T_0 increased its value test by test. As illustrated in Figure 3.1, suction ambient air in point (0) is guided into the Rover's compressor through the long pipe inlet duct in point (1) and after the combustion phase (C) in point (3) the hot gases expand into the axial turbine (4), before coming out the chimney. The measured inlet pressure loss through the diaphragm Δp_{BL} permitted to calculate the mass flow rate. Other measures of differential pressure between ambient and inlet compressor Δp_{01} and between outlet turbine and ambient Δp_{04} , have been visualized on the main panel together with T_2 , p_2 , p_3 , T_4 and fuel consumption information. On the eddy current brake's panel, the number of output gear shaft revolutions, output torque and thus the net power, were displayed for each test and recorded. Figure 3.2 shows the main output displays and some other important component such as eddy current brake and the starter battery.

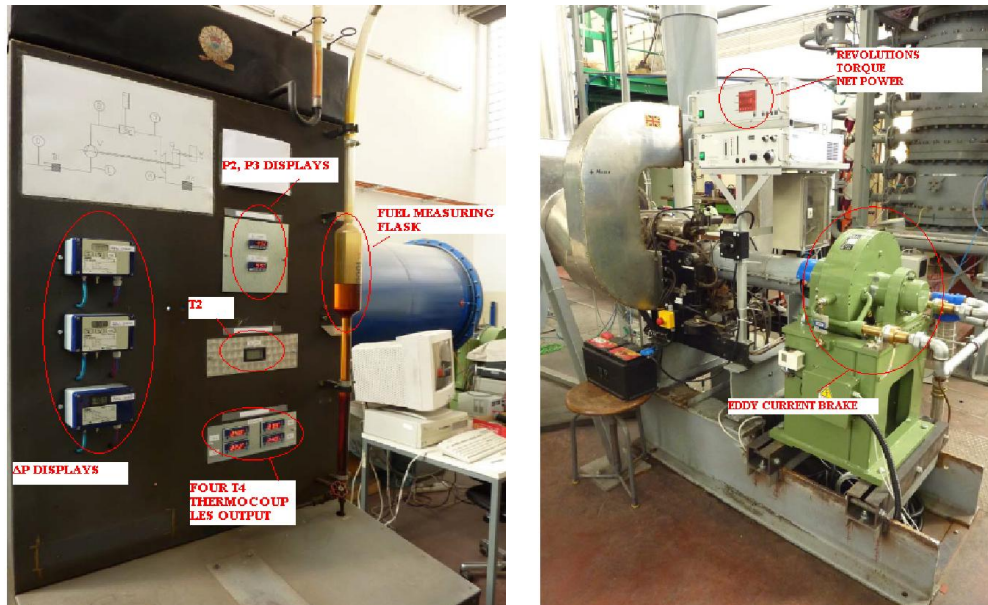


Figure 3.2 Main and eddy current brake's panels

3.2 Components and transducers

3.2.1 Inlet and outlet ducts

The inlet duct is a long pipe with a diameter of 245mm as shown in figure 3.3. A diaphragm assembled at the front of the pipe permits the measurement of the inlet mass flow \dot{m}_{air} , inducing a concentrated pressure loss across its section. The measurements taken will be explained in the following paragraphs.

The outlet duct, leads the expanded hot gases out of the laboratory, into the chimney. After several minutes and tests, the Chimney Effect has occurred, making stronger the outflow. This phenomenon has falsified the outlet pressure drop Δp_{04} output values and created the necessity to overlook this phenomena. However this modified procedure did not influence the final results since the pressure loss values were very small.



Figure 3.3 *Inlet duct and old control panel before Januschewsky's renovation*

3.2.2 Absolute pressure transducers

Resistive absolute pressure transmitters were used as their functional principle is quite simple: the pressure sensor converts the mechanical pressure value into a proportional electrical signal. The pressure sensor consists of a stable main body (frame) and a thin pleated curved diaphragm which allows to improve wet pressure area more than what a flat surface diaphragm can do. Figure 3.4 shows that measured pressure acts on one side of the diaphragm and on the other side there's a vacuum darkroom.

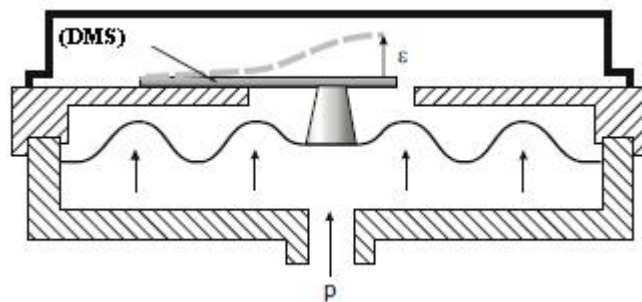


Figure 3.4 *Absolute pressure transducer [6]*

The diaphragm is the most important element for the measurement of the pressure and is equipped with strain-sensitive and compression-sensitive resistance structures, so called strain gauges (DMS). The diaphragm is deflected under the influence of pressure. Thus, the strain gauges attached to it are elongated or compressed and its electrical resistance changes. This change in resistance is directly proportional to the pressure.

The resistive pressure transducers JUMO 40.4346 for non aggressive gases, measure absolute inlet combustor pressure p_2 and absolute outlet combustor pressure p_3 making it possible to estimate the combustor pressure loss Δp_{23} calculating the difference ($p_3 - p_2$). Here below in Table 3.1 some transducer's properties are reported:

p_2 & p_3	Voltage supply	10 – 30 DC [V]
	Pressure range	0 – 2.5 [bar]
	Output power	4 – 20 [mA]

Table 3.1 *JUMO 40.4346 series absolute pressure transducers*

3.2.3 Differential pressure transducers

In order to evaluate Δp_{BL} , Δp_{01} and Δp_{04} the test bed has been equipped with three highly sensitive inductive differential pressure transducers that are represented by a scheme such as in figure 3.5 .An inductive pressure transducer uses the principle of inductance to convert the flexing of a diaphragm into the linear movement of a ferromagnetic core. The movement of the core is used to vary the induced current generated by an AC powered primary coil on another secondary pick-up coil. [7].

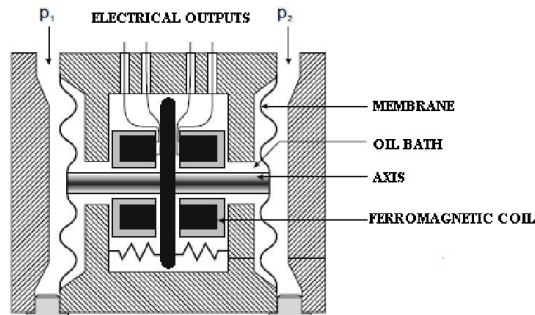


Figure 3.5 *Scheme of an inductive differential pressure transducer*

The ferromagnetic core has two equal inductances and when the pressure acts on one metallic diaphragm, one of the two rises and produces an electrical output. The TU WIEN's test bed was equipped with JUMO 40.4303 series, differential pressure transducers:

$\Delta p_{BL}, \Delta p_{01}$	Pressure range	0 – 25 [mbar]
	Voltage supply	11 – 35 DC [V]
	Diaphragm's diameter	6 [mm]
Δp_{04}	Pressure range	0 – 1.6 [mbar]
	Voltage supply	11.5 – 30 DC [V]
	Diaphragm's diameter	6 [mm]

Table 3.2 *JUMO 40.4304 series differential pressure transducers*

The Δp_{BL} differential pressure transducer's probes were located near the diaphragm's walls, connected to the transducer's control unit, with four tubes two meters long. The reason of this is explained in paragraph 3.3.1.1.

3.2.4 Thermocouples

In order to get temperatures information, the test bed is equipped with five thermocouples. Each transducer has an electrical circuit formed by two metal conductors of different metals soldered together at one extremity (Figure 3.6). The heating of the hot junction creates a voltage (Seebeck EMF) in correspondence to the cold junction. The entire measuring process is based on "Seebeck effect" which consists in a thermoelectric EMF rising when hot junction is warmed.

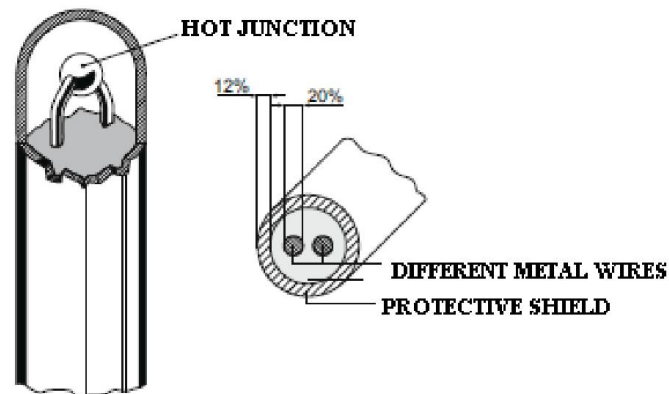


Figure 3.6 *Thermocouple*

When the hot junction is immerse into the hot flow, an Electromotive Force arises at the wires' end. However we cannot measure directly the EMF with a voltmeter due to the presence of a third electrical circuit. To overcome this problem a second COLD junction at a known temperature, built with a homogeneous metal, must be linked to the other two wires. Knowing the cold junction temperature, and measuring the EMF we were able to measure the hot junction temperature, which corresponds to the hot flow temperature (Figure 3.7)

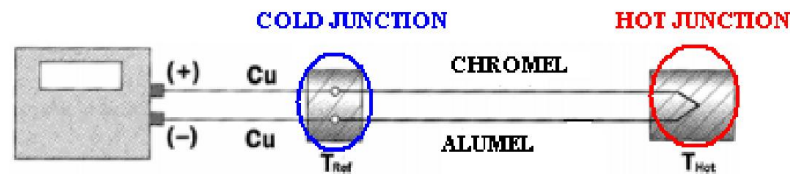


Figure 3.7 *Thermocouple's scheme*

On TU WIEN's test bed the first thermocouple is located near to the outlet compressor and measures the compressed air temperature T_2 . The other four thermocouples 30 cm long have been arranged circumferentially at the turbine diffuser, beside the outlet turbine impeller (Figure 3.8).

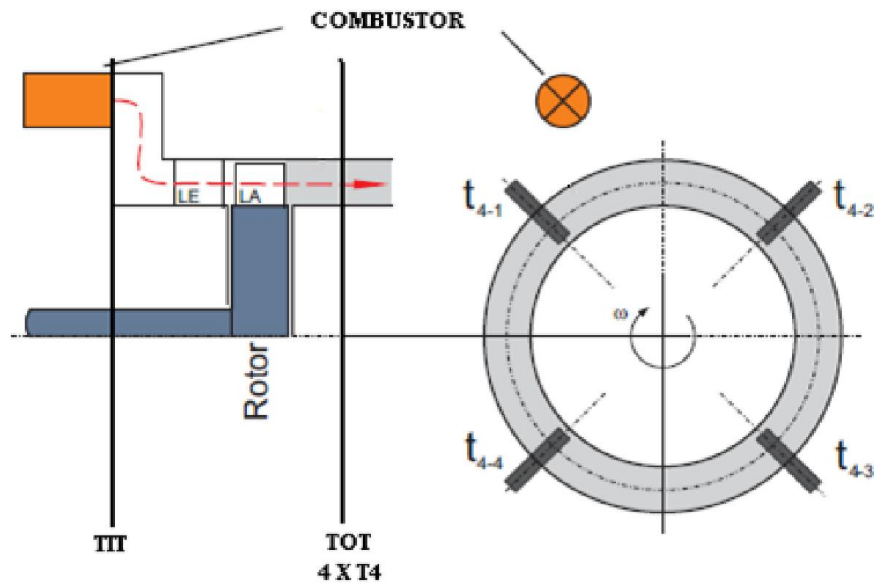


Figure 3.8 *Thermocouples positioning*

Due to the high TOT (mean value of 670°C), the four thermocouples were built with a special metal alloy Chromel®-Alumel® (trademark of Hoskins Manufacturing Company) K-series which contains Nickel. This permits them to withstand very high temperatures (till 1370°C) in an oxidizer and low corrosive atmosphere, such as the mixture of air and burned Diesel. An electric safe valve is present in the event that T_4 is higher than $T_{4max} = 800^{\circ}\text{C}$. This valve cuts off the fuel suction in order to avoid serious damages to the turbine stage. The main characteristics of thermocouples are shown in Table 3.3.

K series	
Temperature range	$-200 \rightarrow +1370^{\circ}\text{C}$
Vmax	$\approx 50 \text{ [mV]}$
Accuracy	$2 [^{\circ}\text{C}]$
Sensitivity	$41 [\mu\text{V}/^{\circ}\text{C}]$
Other Characteristics	Low price, oxidation resistance, slow dynamic response

Table 3.3 *K-series Thermocouples' properties*

3.2.5 Speed adaptor and eddy current brake

During the hot gas expansion the total generated mechanical power in the turbine, flows through the main shaft permitting the shaft to operate the compressor. Another portion of the mechanical power is dissipated in friction losses. Finally the net power flows through a 15.33 rotational speed ratio gear box system, which permits the reduction of the output revolutions from 46.000 rpm up to 3000 rpm . However during tests, it has been decided to reduce the output gear's rotational speed from 3000 rpm up to 2000 rpm in order to preserve the old ROVER's components to avoid failures and damages. The output gear shaft is connected to an eddy current brake system supplied by "Borghi&Saveri" company. The current brake system controls load parameters thanks to the connection with a load cell as shown in figure 3.9.

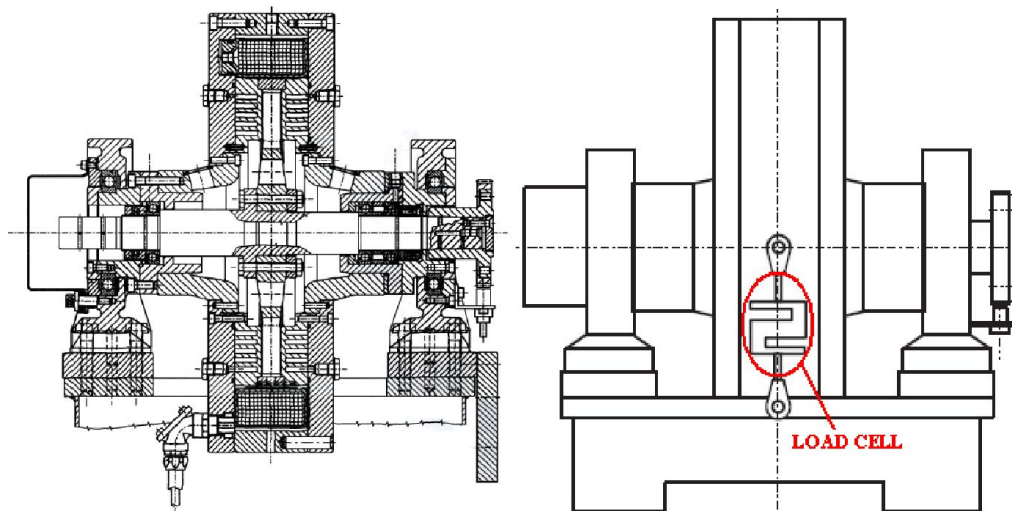


Figure 3.9 *Borghi&Saveri eddy current braking system with load cell connection*

In eddy current braking systems there are a rotor and a stator. The rotor is made by a magnetic alloy. The phenomenon that produces reverse forces is due to the relative motion between the magnet and the stator metal conductor. Thanks to the relative motion, through the stator's turns an electrical current that induces a reverse magnetic field establishes and results in deceleration (Fig. 3.10). Without using friction, an eddy-current braking system transforms the kinetic energy of the moving body into heat energy that is dissipated through the cooling system.

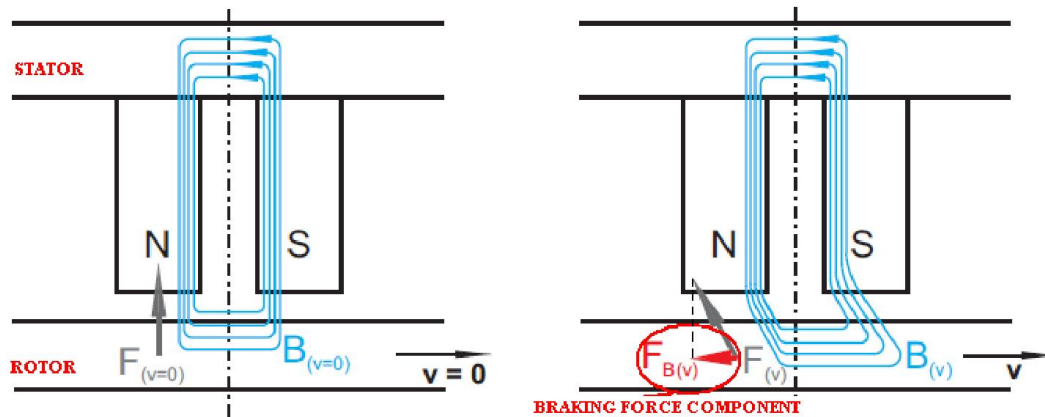


Figure 3.10 Eddy current braking system principle of functioning

The model used for test bed was a Borghi&Saveri FE 150-S, that means its maximum range power is 150 CV or 235 Nm at 13000 rpm. In figure 3.11 are represented the four load points corresponding to one of the diaphragms we tested (169.5 mm inlet diaphragm diameter).

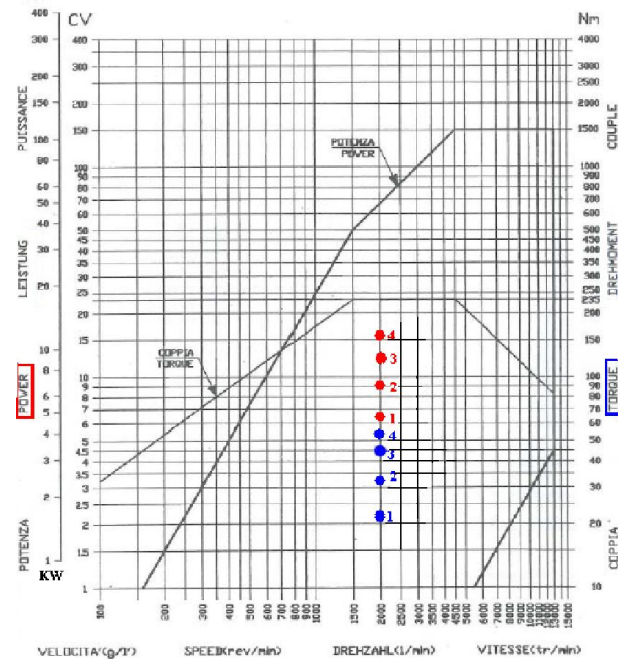


Figure 3.11 169.5mm inlet diaphragm load points represented on functioning map

3.3 Mass flow rate measurement

In order to evaluate ROVER's performance it was necessary to measure the mass flow rate involved in the Joule-Brayton cycle. For this purpose different methods and devices are available on the market. These sensors have been split into two families:

1. Energy Extractive
2. Energy Additive

In the "Energy Extractive" transducers, an energy loss takes place once the fluid passes through the sensor, so that the fluid gives a small amount of its energy to the fluid that generate the output signal.

In the "Energy Additive" transducers the opposite happens. Sensors give energy to the working fluid, obtaining the output signal.

The main devices available on the market work on different physics principles such as, Magnetic Induction, Coriolis forces, Von Karman Vortex, Pressure Losses through calibrated orifices, etc.

3.3.1 Norms for volume and mass flow rate measurement

Currently, norm EN-ISO 5167 describes different techniques for measurement of fluid flow by means of pressure differential devices inserted in circular cross section conduits running full. It is composed of four main sections: the first gives general principles and requirements, the second describes the orifice plates devices (also called Δp meters) and the third and the fourth describe respectively nozzles, Venturi nozzles and Venturi tubes.

However, the VDI/VDE 2041 norm normally used for measurement devices located at the pipe's entrance was applied in order to be able to calculate the mass flow rate \dot{m}_{air} elaborated by the compressor .

3.3.1.1 EN-ISO 5167-1 and 5167-2

The VDI/VDE 2041 norm which was used for the tests, will be discussed using the basis of EN-ISO 5167-1 and 5167-2

Three different Δp meters were adopted because of their simple geometry, global standardization and high reliability.

The reference for measurement of a fluid flow by means of pressure differential devices (Δp meter) inserted in circular cross-section conduits running full are EN-ISO 5167-1 [8] and 5167-2 [9]. A Δp meter functioning principle is quite simple and is based on the application of Bernoulli's law (equation 3.1) into a pipe across an orifice. (Figure 3.12). What is measured permits to extrapolate

the volume or mass flow rate value is the pressure loss originated across the orifice plates.

$$z + \frac{p}{\rho g} + \frac{w^2}{2g} + \frac{u}{g} = \text{const} \quad (3.1)$$

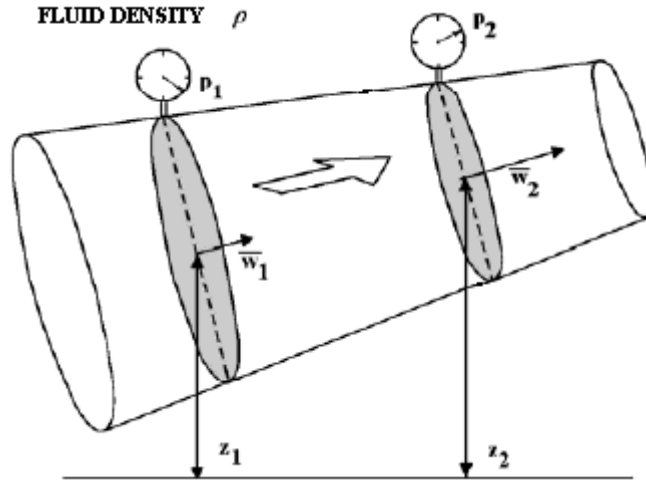


Figure 3.12 Pipe line and Bernoulli's terms

If the working fluid is incompressible ($\rho_1 = \rho_2$), and there is no heat transfer with the outside (internal energy u keeps constant), and the pipe line is horizontal, the equation (3.1) becomes

$$\frac{p}{\rho} + \frac{w^2}{2} = \text{const} \quad (3.2)$$

The diaphragm causes a highly concentrated pressure loss, and as a result the pressure drops going through the diaphragm and the fluid speed increases. For incompressible fluids, the mass flow rate conservation corresponds to the volume flow rate conservation $A_1 w_1 = A_2 w_2$, thus the volume flow rate is obtained (equation 3.3):

$$\dot{V} = \frac{A_2}{\sqrt{1 - (A_2/A_1)^2}} \sqrt{\frac{2\Delta p}{\rho}} \quad (3.3)$$

Furthermore, the other (3.2) equation hypothesis are :

- Steady flow
- Mono-dimensional condition flow rate much earlier is equal to the mono-dimensional mass flow much later after the orifice device

However before orifice's entrance (point I) and immediately after (point II), flow path is irregular, therefore static pressure data should be taken at point 1 and at point 2 as shown in figure 3.12:

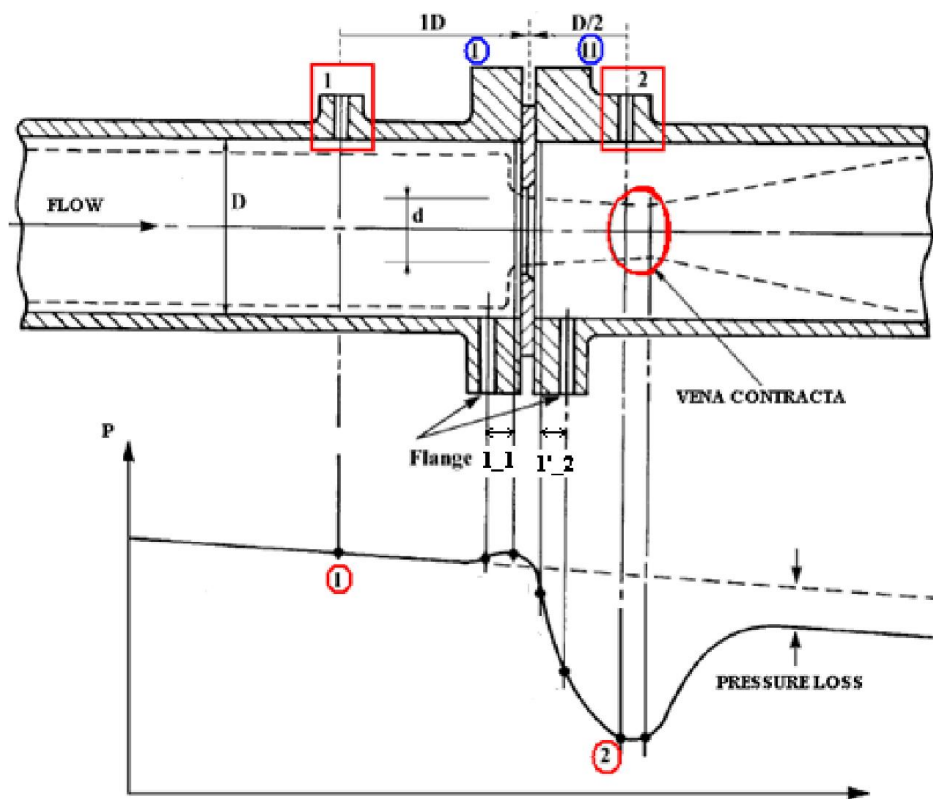


Figure 3.13 *Measuring points*

Usually the position of Vena Contracta is unknown since it changes when the volumetric flow rate (\dot{V}) rises (at constant geometry configuration) or orifice's diameter drops (at constant \dot{V}). For this reason the measurement of pressure in 1 and 2 would be very difficult.

To overcome this problem norm EN-ISO 5167-1 [8] says to connect the static pressure devices in correspondence to the diaphragm's entrance and outlet. The corrective "coefficient of discharge C" is introduced into the equation (3.3) to correct this error. Therefore correct equation (3.3) becomes:

$$\begin{cases} \dot{V} = \chi \frac{\pi d^2}{4} \sqrt{\frac{2\Delta p}{\rho}} \\ A_d = \frac{\pi d^2}{4} \end{cases} \quad (3.4)$$

Where $\overline{\Delta p}$ ($= p_I - p_{II}$) $< \Delta p$ ($= p_1 - p_2$) slightly and χ is called "mass flow rate coefficient" and is equal to:

$$\chi = \frac{C}{\sqrt{1 - \frac{D^4}{d^4}}} \quad (3.5)$$

The mass flow rate coefficient χ depends on $\beta = \frac{D}{d}$ and Reynolds (Re) number because of the relationship between C and Re number correlation (Figure 3.14):

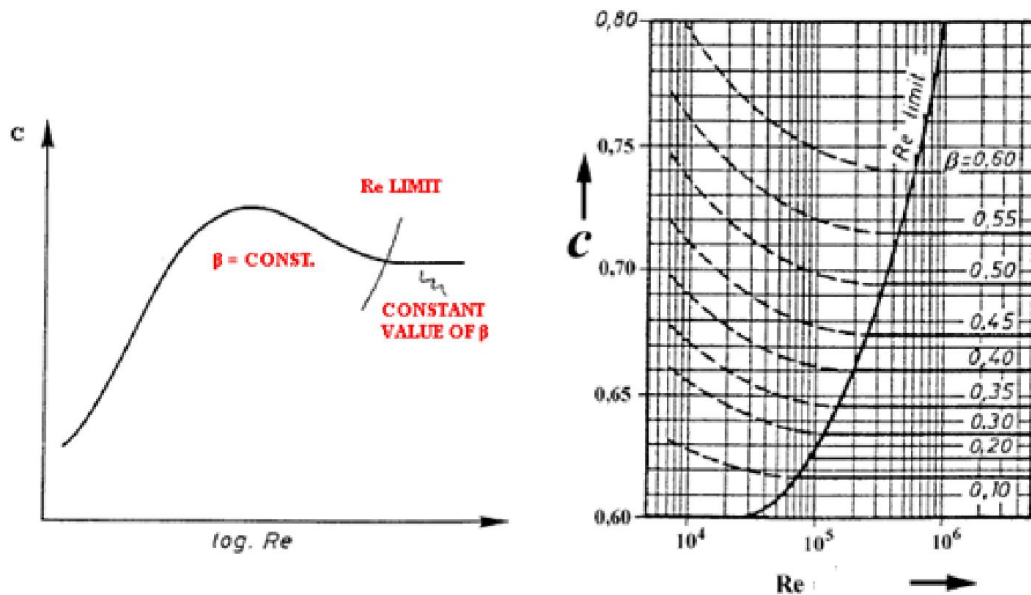


Figure 3.14 C coefficient function of Re and β

The coefficient of discharge C is given by the empirical equation (3.6) of READER HARRIS/GALLAGHER [6]:

$$C = 0.5961 + 0.0261 \beta^2 - 0.261 \beta^8 + 0.000521 \left(\frac{10^6 \beta}{Re_D} \right)^{0.7} + (0.188 + 0.0063A) \beta^{3.5} \left(\frac{10^6}{Re_D} \right)^{0.3} + (0.043 + 0.08 e^{-10L_1} - 0.123 e^{-7L_1}) (1 - 0.11A) \left(\frac{\beta^4}{1 - \beta^4} \right) - 0.031 (M'_2 - 0.8 (M'_2)^{1.1}) \beta^{1.3} \quad (3.6)$$

Where

$$\begin{cases} A = \left(\frac{19000\beta}{Re_D} \right)^{0.8} \\ M'_2 = \frac{2L'_2}{1 - \beta} \end{cases} \quad (3.7)$$

And

$$\begin{cases} L_1 = \frac{l_1}{D} \\ L_2^1 = \frac{l'_2}{D} \\ Re_D = \frac{\rho w D}{\mu} \end{cases} \quad (3.8)$$

One of the most important advantage of these diaphragms is the possibility of measuring incompressible and compressible fluid mass flow rates. However to measure the compressible fluid mass flow rate, the compressibility effect of the gas needs to be taken into account. Pressure loss through the diaphragm modifies the density of the gas (air), thus the compressibility factor ε must be introduced into equation (3.4). Finally the air mass flow rate value is given by:

$$\dot{m}_a = \varepsilon \chi A_d \sqrt{2 \rho \Delta p} \quad (3.9)$$

Where $\varepsilon = \varepsilon(\beta, \overline{\Delta p}, \gamma)$:

$$\varepsilon = 1 - (0.351 + 0.265\beta^4 + 0.93\beta^8) \left[1 - \left(\frac{p_2}{p_1}\right)^{\frac{1}{\gamma}}\right] \quad (3.10)$$

and γ is the ratio of specific heats (equation 4.5).

Norms EN ISO 5167 1 and 5167-2 assume pressure differential devices inserted in circular cross-section conduits for the full length of the pipe. The other specifications for the orifice plates with flange tapplings are:

- $d \geq 12,5 \text{ mm}$
- $50 \text{ mm} \leq D \leq 1000 \text{ mm}$
- $0.1 \leq \beta \leq 0.75$
- Both $Re_D \geq 5000$ and $Re_D \geq 170 \beta^2 D$

As mentioned previously, in the experimental tests, the test bed was equipped with the diaphragm mounted in correspondence to the inlet pipe section. The norm, VDI-VDE 2041 [10] was used and it will be shown how it derives from norm EN ISO 5167-2 .

3.3.1.2 VDI-VDE 2041

A diaphragm at the beginning of a pipe line is used for the flow measurement of fluid at the intersection between a large room (or atmosphere) and the connected pipe line. A large room is defined as a room with dimensional limits which exceed 10 times the distance from the point of intersection (figure 3.15):

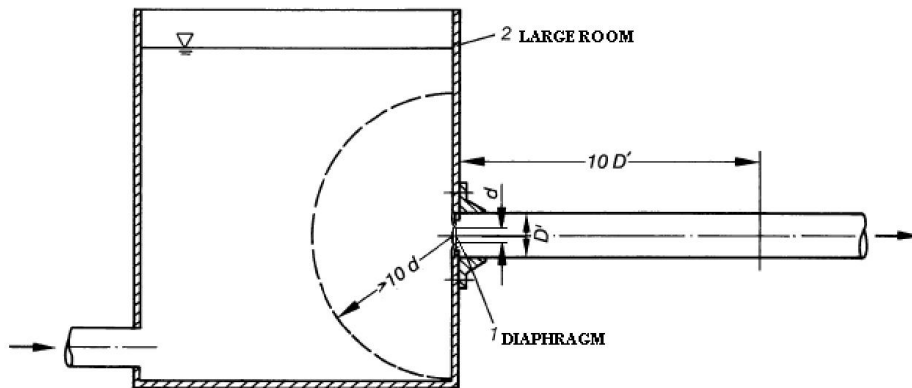


Figure 3.15 *Scheme of the inlet measuring system*

VDI-VDE 2041 norm permits to measure the inlet or outlet flow across a primary device mounted on a pipe's extremity. It requires that the inflow must be swirl free and symmetrical. The Reynolds number Re_d referred to the throat diameter of the primary device must be larger than value of 10^5 .

The orifice's coefficient of discharge is $C = 0,5961$ and since $D \rightarrow \infty$ thus the mass flow rate coefficient is $\chi = C$. For orifices the compressibility factor established by norm VDI-VDE 2041 is:

$$\varepsilon = 1 - 0,351 \left[1 - \left(\frac{P_2}{P_1} \right)^{1/\gamma} \right] \quad (3.11)$$

Where P_1 and P_2 are referred to pressure on inlet and outlet orifice surfaces.

The whole normed procedure and all the hypothesis previously exposed, have been considered true during our tests. Furthermore this measuring procedure assures an accuracy of 1-2%.

3.3.2 Adopted diaphragms

Three different orifice plates were used during tests. Each one was designed to induce concentrated pressure losses across the orifice, following EN-ISO 5167 norm measurement requirements (Figure 3.16).

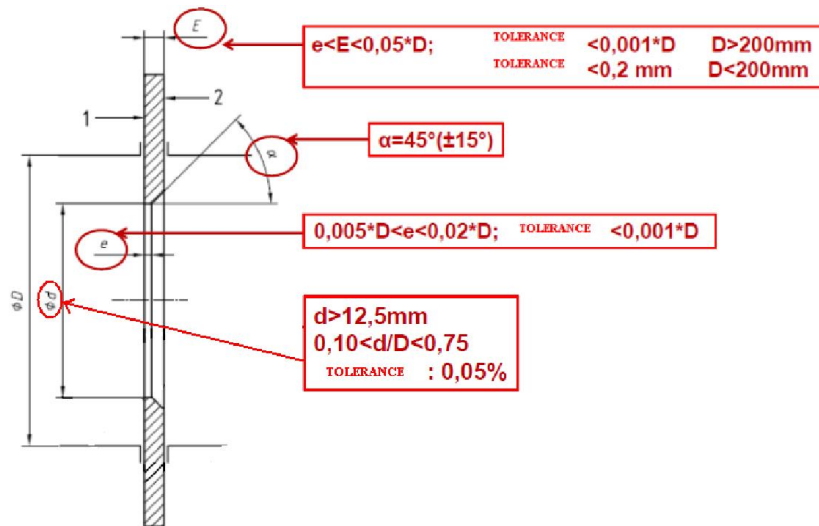


Figure 3.16 Normed orifice plate

The main characteristics of three orifice plates were rounded angles α of 45° , inner diameter 'd' of 169.5 mm, 140 mm, and 115.8 mm for different diaphragms respectively. Figure 3.17 shows the 169,5mm diaphragm with measurements.

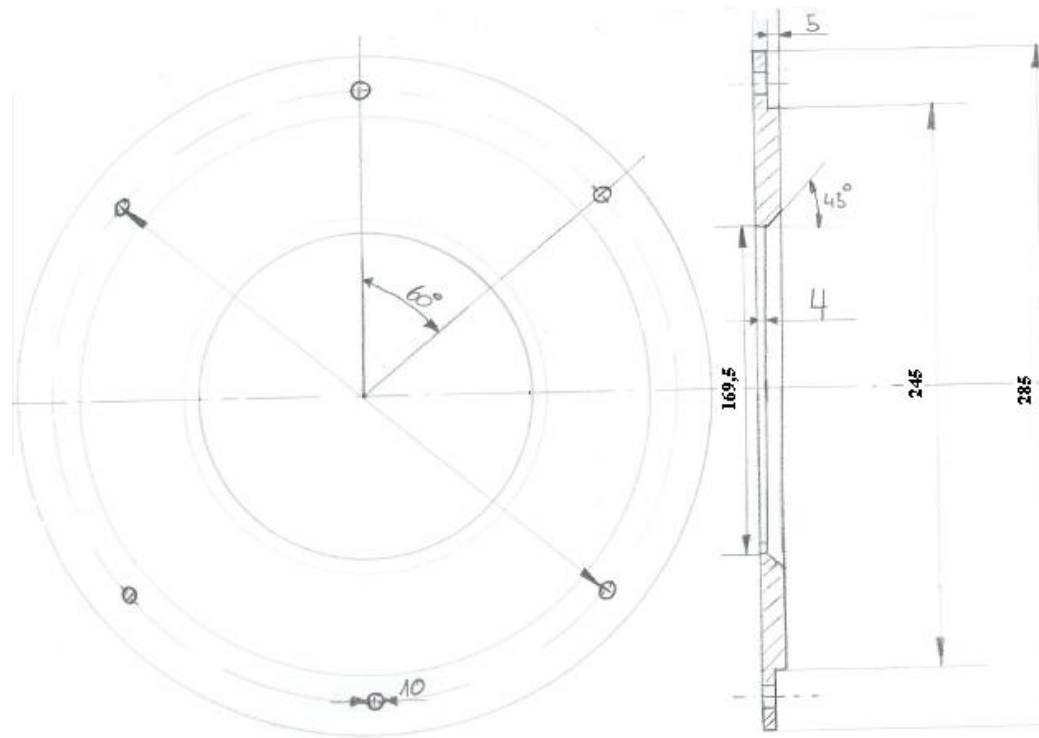


Figure 3.17 169.5 mm orifice plate

Chapter 4

Tests

This chapter will introduce how the tests have been carried out.

4.1 Tests preparation

Before the Rover 1S/60 start, the entire test bed was checked, in order to avoid any kind of problem during the tests. Furthermore, for each test session we fixed the diaphragms to the edge of the inlet duct and before the start the environment static temperature T_0 and pressure p_0 were measured.

Each test session consisted of four tests: every test was conducted on a different operating load point thanks to the control lever which allows to change the eddy current brake's power. The rotating output of the adaptor's shaft was kept at a constant speed of ≈ 2000 rpm instead of 3000 rpm, in order to avoid turbine failure and damages:

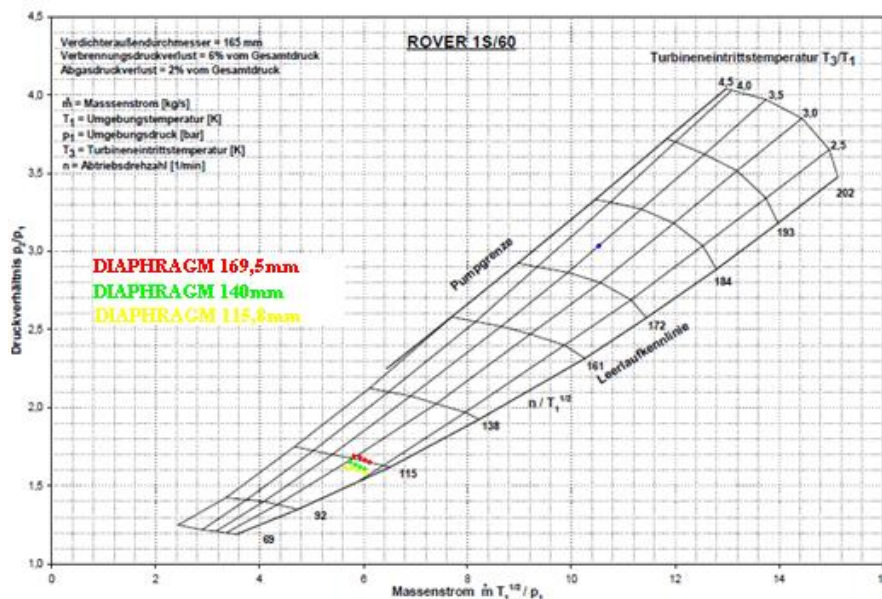
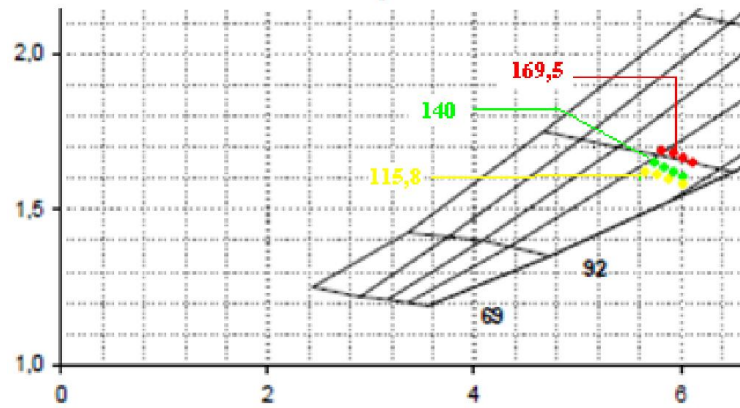


Figure 4.1 *ROVER's functioning map***Figure 4.2** *Focus on the three different diaphragms operating load points*

At first the gas turbine for the run up phase was started, which took few minutes. After which, the real operational tests began with the first, the second, the third and the fourth operating load points. For each test the fuel time consumption was timed and all the data recorded: P_{eff} [KW] (effective power output), Δp_{BL} [mbar] (pressure drops through the diaphragm), Δp_{01} [mbar] (total inlet pressure drop), p_2 [mbar] (compressor inlet static pressure), p_3 [mbar] (combustor chamber inlet static pressure), T_2 [°C] (compressor inlet static temperature), Δp_{04} [mbar] (total outlet pressure loss), $4 \times T_4$ [°C] (turbine outlet static temperatures). After each test the gas turbine took a few minutes to shut down. The Rover 1S/60 was run approximately twelve minutes per test session, with each consecutive test the laboratory room became warmer and warmer due to the hot exhausted gases. As a consequence, it was necessary to wait several minutes in order for the room temperature to cool down, reinstating the ambient temperature, before starting a new test. This procedure was adopted for each diaphragm.

4.2 Data acquisition setbacks

During the test bed test, some problems arose. A test bench requires to be checked every time, in order to avoid setbacks which influence and modify the transducers' data. Furthermore those problems entail loss of time and loss of money. Examples of some setbacks encountered are described below.

4.2.1 Test one repetition for the 169,5mm diaphragm

At first we adopted the 169,5 mm diaphragm (external over internal diameter ratio of 1,445) and ran up the Rover 1S/60 giving it the wrong ramp up slope load. For this reason the machine and the entire system, including the transducers, didn't have enough time to warm up and consequently all data output was inconsistent. Therefore it has been decided to move to the second load point, which showed consistent data. The third and the fourth load points were estimated as well. Finally, the first load point was tested again, and we noticed that T_1 value was higher than the same one for the 140 mm diaphragm. This unforeseen phenomenon was caused by the machine heating after several minutes of operation (see figure 4.3). On the contrary, the 140 mm diaphragm's T_1 was measured after an heat reduction phase.

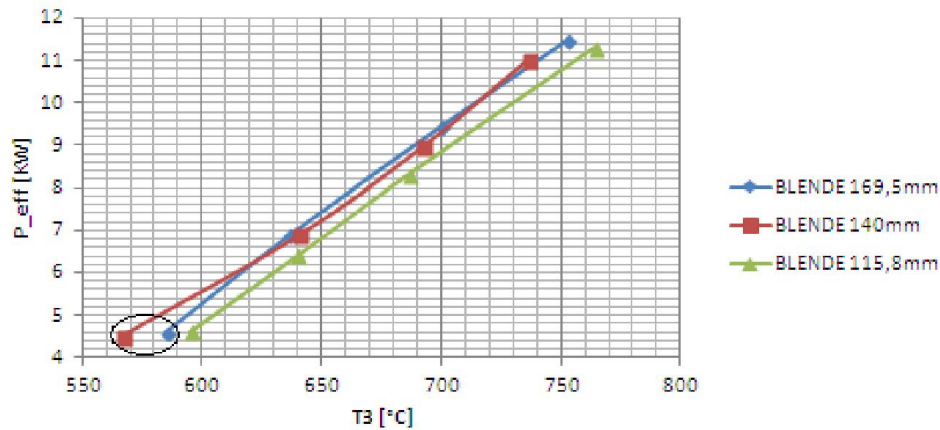


Figure 4.3 T_3 - P_{eff} diagram and the unforeseen phenomenon

This different procedure was adopted only for the 169,5 mm diaphragm.

4.2.2 Chimney Effect

Many instruments are installed on the test bed, and after few tests it was noticed that one of them didn't work. The reason for this being that the differential pressure transducer Δp_{04} provided unexpected and irregular output data.

The output pressure drop was expected to be positive, and because of this a turbine output back pressure should exist. In our instance, not only were the values negative, but also they were also irregular. The major reason for this phenomenon was the Chimney effect (Stack effect) and a wrong transducer's

tubes connection: The chimney effect is the natural phenomenon that occurs when the density difference between a hot and a cold air column creates a natural flow through a chimney. Large temperature differences between the outside air and the flow gases can create a strong stack effect in chimneys [11]. For this reason the output data was irregular as shown in Table 4.1.

Diameter			Test 1	Test 2	Test 3	Test 4
169,5mm	Δp_{04}	[mbar]	0,11	0,39	0,27	0,29
140mm	Δp_{04}	[mbar]	0,28	0,15	0,2	0,13
115,8mm	Δp_{04}	[mbar]	0,17	0,23	0,32	0,31

Table 4.1 *Unsteady output data given by Δp_{04} differential pressure transducer*

In addition to the Stack effect, the tubes connections were wrong, and it caused unexpected negative output values.

4.2.3 Calibration for the outlet differential pressure transducer

In order to verify the transducer's problems , its recalibration was necessary. For this reason, a Meriam Instrument calibrator was adopted: its accuracy is $\pm 0.025\%$ of Full Scale and accuracy is maintained over operating temperatures from -20° to $+50^{\circ}$ °C. Furthermore a five liter container was employed in order to avoid pressure fluctuation during the measuring test caused by the small absolute volume in the tubes. Below in figure 4.4 the measurement equipment is shown:

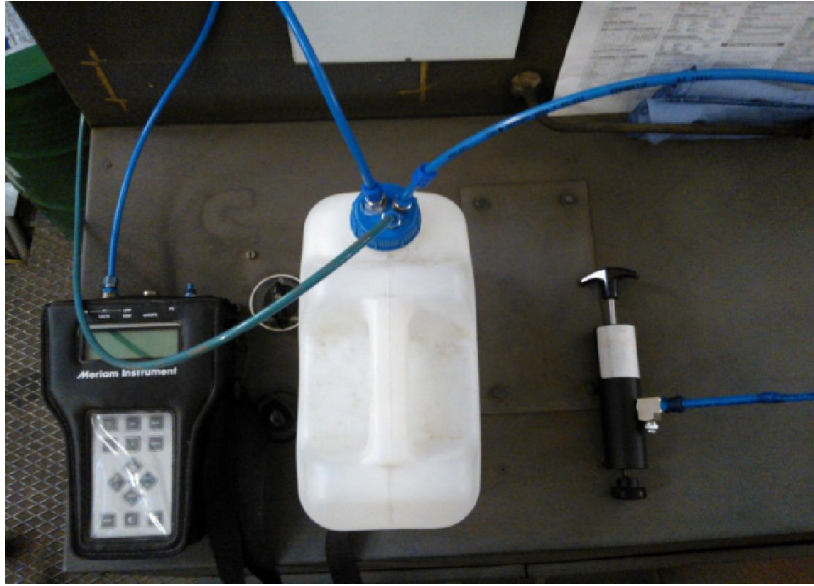


Figure 4.4 Δp_{04} test check equipment

The correct functionality was verified. Nevertheless, the results showed insignificant Δp_{04} and therefore it was decided not to take this into account. The reason is explained hereunder.

4.3 Data set

4.3.1 Air and fuel properties

The good understanding of air properties is fundamental in order to get the right results from the calculations. Table 4.2 was used to evaluate the different values of $R_{gas} = f(\lambda)$ caused by different α/α_{st} ratios:

λ [-]	R_{-G} [J/kgK]
1	288,45
2	288,48
5	288,49
∞	288,51

Table 4.2 *Correspondence between Air Fuel equivalence Ratio and gas constant*

In accordance with engineering literature, Air Fuel Ratio (AFR) is commonly used in the gas turbine industry as well as in government studies of internal combustion engines, and refers to the ratio of fuel to the air.

$$AFR = \alpha = \frac{m_{air}}{m_{fuel}} \quad (4.1)$$

Air-Fuel equivalence Ratio, λ (lambda), is the ratio of actual Air Fuel Ratio (AFR) α to stoichiometry for a given mixture. $\lambda=1.0$ is at stoichiometry, rich mixtures have $\lambda<1.0$, and lean mixtures have $\lambda>1.0$. A value of $\lambda=\infty$ represents a super lean mixture of air and fuel, this means that we have pure air. There is a direct relationship between λ and AFR α . Air Fuel equivalence Ratio is the reciprocal of Fuel-Air equivalence Ratio Φ

$$\lambda = \Phi^{-1} = \frac{\alpha}{\alpha_{st}} \quad (4.2)$$

With regard to specific heat at a constant pressure c_p , it is a function of temperature and Fuel Air equivalence Ratio λ :

In figure 4.5 below is a diagram which represents $c_p = f(T, \lambda)$:

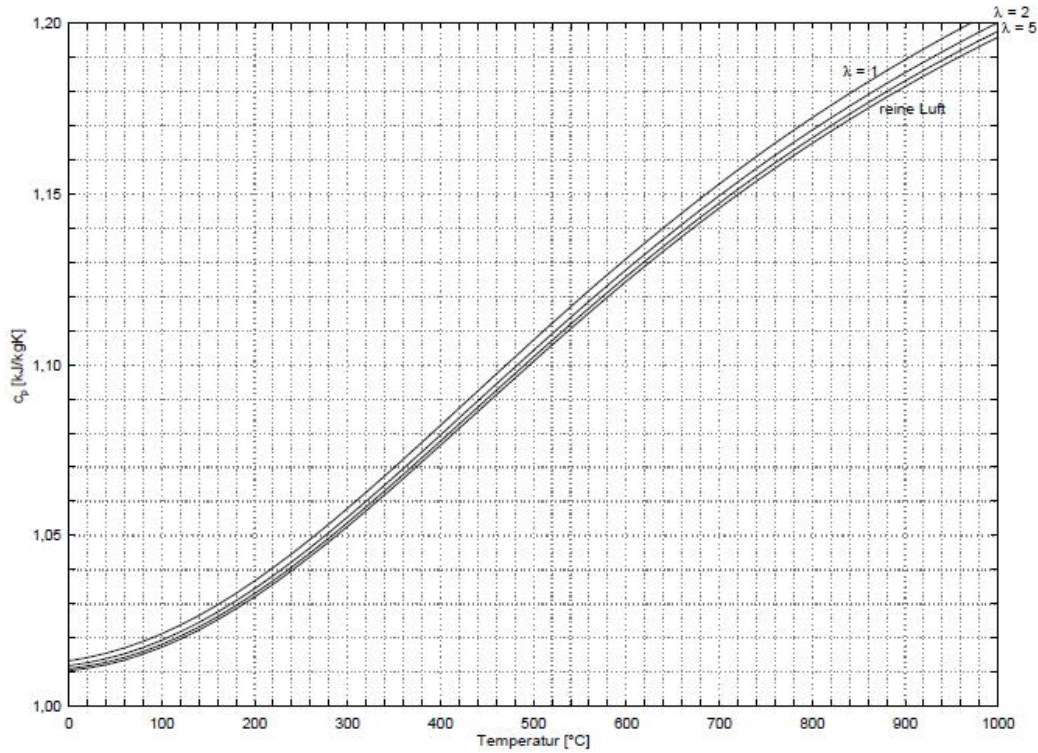


Figure 4.5 *Temperature-specific heat at constant pressure diagram and influence of λ*

The Inlet Temperature T_0 is rather constant (after a laboratory's environment cooling phase) for each test session the inlet air properties was calculated only once. Furthermore the working fluids of many heat engines are gases such as air, steam, or a combusting fuel/air mixture. Over a wide range of temperatures and pressures gases have similar behavior to each other. Therefore the calculations were based on the ideal gas law:

$$c_p - c_v = R \quad (4.3)$$

$$\rho = \frac{p}{R T} \quad (4.4)$$

$$\gamma = \frac{c_p}{c_v} \quad (4.5)$$

$$k = \frac{\gamma - 1}{\gamma} \quad (4.6)$$

Air properties at $T_0 \cong 22^\circ\text{C}$		Measurement units
λ_{air}	∞	[-]
R_{air}	0,28851	[KJ/KgK]
c_{p_air}	1,012	[KJ/KgK]
c_{v_air}	0,72349	[KJ/KgK]
γ_{air}	1,3988	[-]
k_{air}	0,2851	[-]
ρ_{air}	1,1489	[Kg/m3]

Table 4.3 *Air properties at 22 [°C]*

The small ROVER 1S/60 engine used Diesel instead of Natural gas (such as the larger gas turbines), indeed the diluted combustion chambers have no problems with liquid fuels unlike fuel pre-mixed with air. Moreover, premix flames that allow to reduce NOx, were not required in the past. In Table 4.4 Diesel properties are reported:

Fuel properties		Measurement units
α_{st}	14,5	[-]
ρ_{fuel}	0,875	[Kg/dm3]
LHV	42700	[KJ/Kg]

Table 4.4 *Diesel properties*

4.3.2 Static pressure and total temperature

All values of the measured pressure correspond to a static pressure, because of the way pressure transducers have been fitted on the test bed (Figure 4.6). The dynamic part can be considered negligible, as shown in the next. ROVER 1s/60 gas turbine has comparatively small inlet and leaving velocities and it does not tend to have a large difference between total and static parameters. Therefore the

test bed was equipped only with static pressure probes and not with dynamic probes.

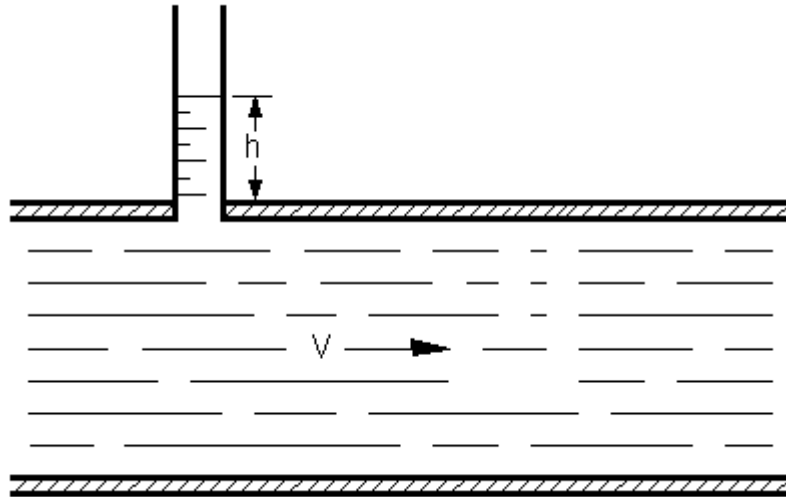


Figure 4.6 *Static pressure probe*

On the other hand, the temperatures through the entire cycle, were measured as total temperatures. The hot thermocouple junctions were awashed into the flow and were not placed at the flow's boundary. However the measured Total to Static ratio for a mono dimensional flow, showed the small contribution given by the dynamic part.

In order to evaluate the effectiveness of static temperature and static pressure measurements, the flow conditions were evaluated into the inlet pipe (Figure 3.17) and in correspondence to the exhaust turbine section (Figure 2.13) . The mono dimensional flow hypotheses are [2]:

- Steady flow
- Adiabatic transformation
- Ideal gas at constant c_p

These hypotheses can be assumed true through the inlet and outlet ducts. Therefore Total to Static ratios can be written as:

$$\begin{cases} \frac{T_T}{T} = 1 - \frac{\gamma - 1}{2} Ma^2 \\ \frac{p_T}{p} = (1 + \frac{\gamma - 1}{2} Ma^2)^{\frac{\gamma}{\gamma - 1}} \\ \frac{\rho_T}{\rho} = (1 + \frac{\gamma - 1}{2} Ma^2)^{\frac{1}{\gamma - 1}} \end{cases} \quad (4.7)$$

The obtained results in correspondence to the inlet and outlet sections for the 169,5mm diaphragm, are reported in Tables 4.5 and 4.6.

DIAPHRAGM 169,5 mm	TEST1	TEST 2	TEST 3	TEST4
c [m/s]	6,4519543	6,3385964	6,2216581	6,10331561
Ma [-]	0,0186882	0,0183599	0,0180212	0,01767841
T1T/T1 [-]	1,0000696	1,0000672	1,0000648	1,00006231
P1T/P1 [-]	1,0002443	1,0002358	1,0002272	1,00021859

Table 4.5 *Inlet pipe flow conditions*

DIAPHRAGM 169,5 mm	TEST1	TEST 2	TEST 3	TEST4
c [m/s]	42,068044	43,78749	46,045297	47,6405777
Ma [-]	0,0764383	0,0774841	0,078987	0,07977150
T4T/T4 [-]	1,0010216	1,0010376	1,0010590	1,00106791
P4T/P4 [-]	1,0039488	1,0040455	1,0041851	1,00425642

Table 4.6 *Outlet duct flow conditions*

These tables show that Total to Static ratios values are equal to one. For this reason the adoption of static pressure probes is acceptable and the dynamic temperature contribution can be assumed equal to zero.

4.3.3 Estimated values

Below, in Tables 4.7, 4.8 and 4.9, all the data that were measured are attached: four tests (1,2,3,4) were carried out for each test session. As explained before, the experiments took more time than expected because of the setbacks.

In chapter three, the thermocouples have been described, and as it can be seen on the table, each thermocouple returned a different TOT. This difference is due to the exhausted gases' Swirl Flow. For this reason, the four thermocouple's output values were averaged.

The output pressure losses Δp_{04} [mbar] were also reported, even if they will be not considered in the modeling procedure: as can be seen $|\Delta p_{04}|$ values are small and quite irregular.

DIAPHRAGM 169,5 mm		Test 1	Test 2	Test 3	Test 4
p0	[mbar]	979	979	979	979
T0	[°C]	22,2	22,2	22,2	22,2
T0	[K]	295,35	295,35	295,35	295,35
Torque	[Nm]	22,3	32,9	43,5	55
Revolutions	[rpm]	2006	2006	2000	1988
P_eff	[KW]	4,6	6,9	9,45	11,5
Δp_{BI}	[mbar]	-2,9	-2,8	-2,7	-2,6
Δp_{01}	[mbar]	-7	-6,8	-6,35	-6
$ \Delta p_{01} $	[mbar]	7	6,8	6,35	6
p2	[mbar]	1606	1618	1626	1625
p3	[mbar]	1532	1547	1558	1560
Δp_{04}	[mbar]	0,11	0,39	0,27	0,29
T2	[°C]	95	97	98	100
T4 (1)	[°C]	489	537	591	627
T4 (2)	[°C]	475	528	597	657
T4 (3)	[°C]	545	592	652	700
T4 (4)	[°C]	510	541	585	626
T4 (mean value)	[°C]	504,75	549,5	606,25	652,5
Time fuel consumption τ [s]		174	159	146	136

Table 4.7 169.5 mm test section output data

DIAPHRAGM 140 mm		Test 1	Test 2	Test 3	Test 4
p0	[mbar]	979,3	979,3	979,3	979,3
T0	[°C]	22,4	22,4	22,4	22,4
T0	[K]	295,55	295,55	295,55	295,55
Torque	[Nm]	21,5	33,3	43,3	52,4
Revolutions	[rpm]	1994	1985	1987	1995
P_eff	[KW]	4,5	6,9	9	11,05
Δp_{BI}	[mbar]	-6,1	-5,7	-5,5	-5,4
Δp_{01}	[mbar]	-9,3	-8,7	-8,4	-8,3

ΔP_{01}	[mbar]	9,3	8,7	8,4	8,3
p2	[mbar]	1586	1596	1610	1624
p3	[mbar]	1514	1527	1542	1558
Δp_{04}	[mbar]	0,28	0,15	0,2	0,13
T2	[°C]	88	92	95	94
T4 (1)	[°C]	476	545	587	622
T4 (2)	[°C]	465	538	594	645
T4 (3)	[°C]	525	602	652	691
T4 (4)	[°C]	508	550	582	618
T4 (mean value)	[°C]	493,5	558,75	603,75	644
Time fuel consumption	τ [s]	177	161	150	140

Table 4.8 140 mm test section output data

DIAPHRAGM 115,8 mm		Test 1	Test 2	Test 3	Test 4
p0	[mbar]	979,5	979,5	979,5	979,5
T0	[°C]	22,3	22,3	22,3	22,3
T0	[K]	295,45	295,45	295,45	295,45
Torque	[Nm]	22,3	30,9	40,3	54
Revolutions	[rpm]	1995	1988	1982	1991
P_eff	[KW]	4,62	6,41	8,34	11,32
Δp_{BI}	[mbar]	-12,4	-11,9	-11,4	-10,9
Δp_{01}	[mbar]	-14,4	-13,8	-13,2	-12,6
ΔP_{01}	[mbar]	14,4	13,8	13,2	12,6
p2	[mbar]	1587	1590	1596	1615
p3	[mbar]	1515	1520	1530	1550
Δp_{04}	[mbar]	0,17	0,23	0,32	0,31
T2	[°C]	91	96	98	102
T4 (1)	[°C]	502	540	579	638
T4 (2)	[°C]	491	532	584	670
T4 (3)	[°C]	558	599	645	635
T4 (3)	[°C]	525	549	576	712
T4 (mean value)	[°C]	519	555	596	663,75
Time fuel consumption	[s]	171	164	153	137

Table 4.9 115.8 mm test section output data

4.4 Data processing and ROVER 1S/60 performance

4.4.1 169,5 mm diaphragm

In this paragraph it will be demonstrated the procedure adopted to extrapolate the 169,5 mm diaphragm's data. For the other two diaphragms, are reported only the final data. The deductive reasoning process is exactly the same.

4.4.1.1 Compressor

According to thermodynamic diagram (figure 1.1), for the compressor holds true:

$$\Pi_c = \frac{P_2}{P_1} \quad (4.8)$$

$$\begin{cases} H_c = c_p|_1^2 \cdot (T_2 - T_1) \\ c_p|_1^2 = \frac{1}{(T_2 - T_1)} \int_1^2 c_p dT \cong \frac{(c_p^1 - c_p^2)}{2} \end{cases} \quad (4.9)$$

$$\begin{cases} H_{Cis} = c_p|_1^{2is} \cdot (T_{2is} - T_1) \\ c_p|_1^{2is} \cong c_p|_1^2 \\ T_{2is} p_2^{\frac{(1-\gamma_{air})}{\gamma_{air}}} = const. \end{cases} \quad (4.10)$$

$$\eta_{Cis} = \frac{H_{Cis}}{H_C} \quad (4.11)$$

$$\eta_{Cpol} = \frac{k_{air}}{\log_{\Pi_C} \left(\frac{\Pi_C^{k_{air}} - 1}{\eta_{Cis}} + 1 \right)} \quad (4.12)$$

At first the Isentropic efficiency was estimated, which depends on pressure ratio, on thermodynamic fluid properties and on the fluid's compressibility. However the use of Polytopic efficiency is preferred in place of the Isentropic efficiency, in fact it represents the true turbomachine efficiency without taking into consideration the compressibility effects: $\eta_{Cpol} > \eta_{Cis}$. A complete discussion of Isentropic and Polytopic efficiency is in Appendix A2 reported.

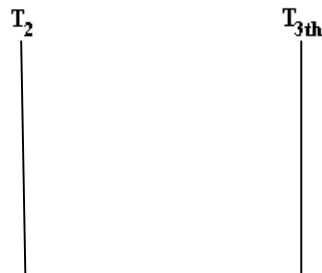
The laboratory equipment was used to calculate the intake mass flow rate in accordance with VDI-VDE 2041 norm, and equation (3.8). Thus Nett Work and the adsorbed compressor power, are described as:

$$W_{net} = \frac{P_{eff}}{\dot{m}_{air}} \quad (4.13)$$

$$P_C = \dot{m}_{air} c_p|_1^2 (T_2 - T_0) \quad (4.14)$$

4.4.1.2 Combustion chamber

The TIT measurement with thermocouples was too complex because of the very high gas temperature, so in order to estimate T_{3th} , the first thermodynamic law has been applied to the combustor chamber:



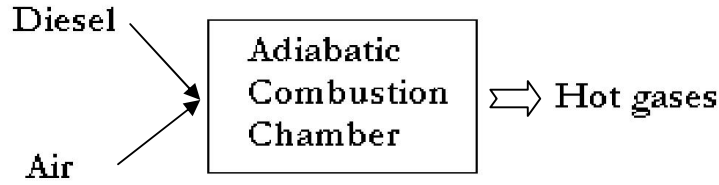


Figure 4.7 *Simplified scheme of combustion process*

Martinez in [12] explains how the adiabatic model very accurately predicts homogeneous combustion temperatures in gas phase, because of the very poor thermal conductivity of gases. The adiabatic model, however, overestimates the temperature in the case of high radiation emission in non-premixed flames. The adiabatic temperature is a thermodynamic state variable that results from the conversion of internal chemical energy to internal thermal energy after the combustion process takes place, and depends on the actual fuel and oxidizer, their ratio (e.g. lean, stoichiometric or rich mixtures), their initial thermodynamic state, and the type and proportions of the compounds formed. It can be measured at the exhaust of an adiabatic combustor, or just after a flame, but the practical difficulties in ensuring minimal heat losses, particularly from the thermometer probe, render a theoretical computation more precise than the actual measurement. The problem with the computation is that the type and proportions of the compounds formed must be known, what is partially solved assuming a set of compounds dictated by experience, and assuming that they are in thermodynamic equilibrium at that pressure and temperature. But, even for the simplest case of a constant-pressure combustion process, the temperature is the unknown result and thus the equilibrium composition cannot be directly computed, yielding an implicit and stiff algebraic mathematical problem.

A drastic simplification of the energy balance occurs if one assumes complete combustion, because then one can resolve the exhaust composition independently of temperature. This approach is useful for combustion of lean mixtures in air (typical for gas turbines), but not for combustion in pure oxygen where temperatures are higher. The adiabatic combustion temperature is obtained from equation (4.15)

$$T_{3th} = \frac{\dot{m}_{fuel} LHV}{c_p|_2^{3th} \dot{m}_{gas}} + T_2 \quad (4.15)$$

Where

$$\dot{m}_{fuel} = \frac{1}{\tau} \rho_{fuel} \quad (4.16)$$

$$\dot{m}_{gas} = \dot{m}_{air} + \dot{m}_{fuel} \quad (4.17)$$

The best precision is obtained with the integration $\int_2^{3th} cp(T)dT$ instead of the approximation $c_p|_2^{3th} \Delta T$, but the form of (4.15) is thought to be the best compromise on precision/effort for non-programmed computations.

However, since $c_p|_2^{3th}$ is λ_3 and T_{3th} dependent, a simplified iterative analysis was required in order to get T_{3th} . The iterative procedure took only two or three steps for each test and before each start, λ_{gas} was calculated using (4.2). A first attempt T_{3th} was taken, hence c_p^{3th} was estimated entering into the T- c_p diagram. At that point, we obtained the new T_{3th} from (4.15). This procedure was repeated until the difference $T_{3th}^n - T_{3th}^{n+1} < 5^\circ C$, indeed this value is considered to be smaller than 1% of error.

TEST 1 ($\lambda=4,7583$)	T3th_n [°C]	cp_m_3-2 [KJ/KgK]	T3th_(n+1) [°C]	ΔT_{3th}
0	700	1,08125	659,1953259	
1	659,195326	1,077	661,4217235	<5
2	661,421723	1,0771	661,3691358	<<5

TEST 2 ($\lambda=4,2726$)	T3th_n [°C]	cp_m_3-2 [KJ/KgK]	T3th_(n+1) [°C]	ΔT_{3th}
0	700	1,082	723,880166	
1	723,880166	1,08425	722,5792848	<<5

TEST 3 ($\lambda=3,8527$)	T3th_n [°C]	cp_m_3-2 [KJ/KgK]	T3th_(n+1) [°C]	ΔT_{3th}
0	700	1,08265	791,5897661	
1	791,589766	1,091	786,2813568	>5
2	786,281357	1,0905	786,5969374	<<5

TEST 4 ($\lambda=3,5218$)	T3th_n [°C]	cp_m_3-2 [KJ/KgK]	T3th_(n+1) [°C]	ΔT_{3th}

0	740	1,0865	854,8177061	
1	854,817706	1,098	846,9120562	>5
2	846,912056	1,092775	850,4833454	<5

Table 4.10 T_{3th} determination with a simple iterative procedure

At the end the specific fuel consumption (4.18) and the combustion chamber efficiency (4.19) were calculated:

$$b_{fuel} = 3600 \frac{\dot{m}_{fuel}}{P_{eff}} \quad (4.18)$$

$$\eta_{cc} = \frac{c_p|_2^3 (T_3 - T_2)}{c_p|_2^3 (T_{3th} - T_2)} \quad (4.19)$$

		Test 1	Test 2	Test 3	Test 4
b_fuel	[Kg/KWh]	3,935532	2,871206	2,283105	2,014066
η_cc	[-]	0,859305	0,854	0,868491	0,871728

Table 4.11 *Combustor's performance*

4.4.1.3 Turbine

Before calculating P_T , the P_{lost} - n diagram was used (Fig.4.8), which shows how the rotational output speed influences the power losses: the curve has an exponential tendency. For each test, P_{lost} was calculated entering into the chart with the rotational speed $n \cong 2000 \text{ rpm}$.

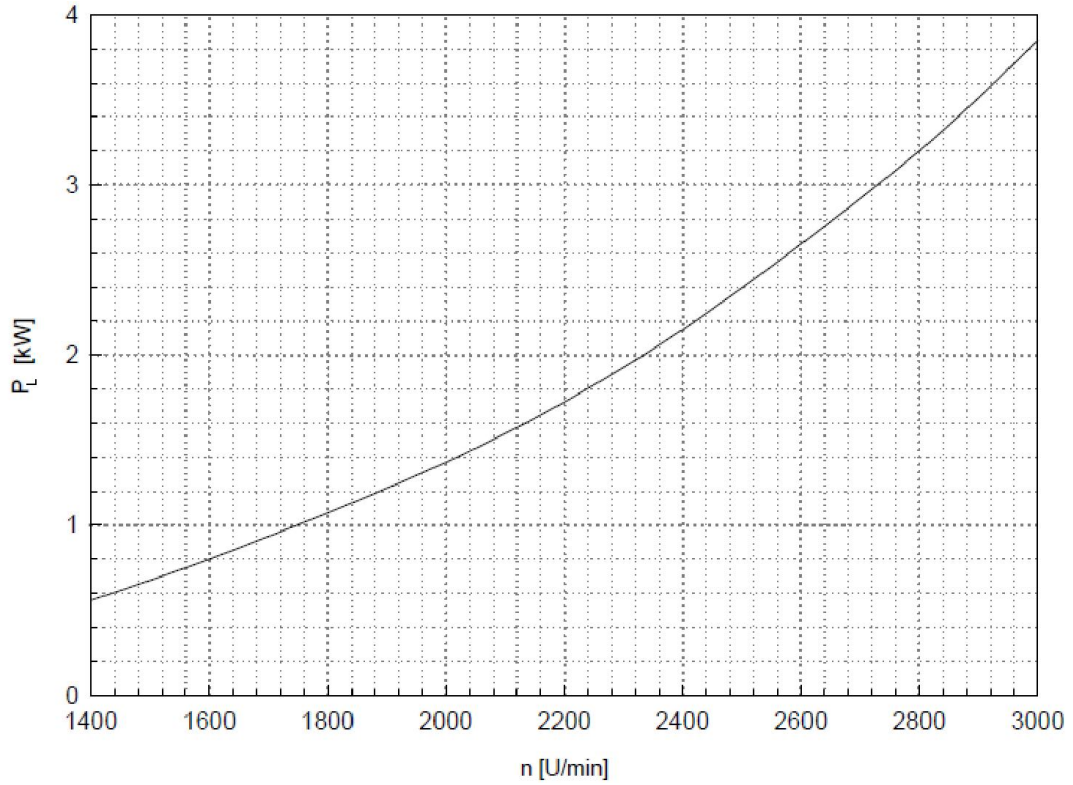


Figure 4.8 Loss power in function of gearbox output shaft revolutions

At that point it was possible to calculate P_T deducting P_{lost} and P_C from P_{eff} .

$$P_T = P_{eff} + P_C + P_{lost} \quad (4.20)$$

The actual T_3 is obtained with (4.21):

$$T_3 = \frac{P_T}{c_p|_{3th}^4 \dot{m}_{gas}} + T_4 \quad (4.21)$$

Where c_p^4 is obtained looking at $c_p = f(T, \lambda)$ diagram for $T = T_4$ and $\lambda = \lambda^{test i}$, and where $c_p|_{3th}^4$ is the mean value $\frac{c_p^{3th} + c_p^4}{2}$. Finally, true c_p^3 and $c_p|_3^4$ values have been evaluated from diagram shown in figure 4.5.

	Test 1	Test 2	Test 3	Test 4
T3_th [°C]	661,369136	722,5792848	786,5969374	850,5
T3_th	934,519136	995,7292848	1059,746937	1124

[K]				
P_compressor [KW]	25,5998184	25,85904437	25,74590665	25,94
P_lost [KW]	1,4	1,4	1,38	1,35
P_turbine [KW]	31,5998184	34,15904437	36,57590665	38,79
cp4 [KJ/Kg*K]	1,10375	1,1132	1,1285	1,138
cpm_3-4 [KJ/KgK]	1,121475	1,13285	1,14625	1,153
T3_eff [°C]	584,800475	636,5374763	699,8818137	753
T3_eff [K]	857,950475	909,6874763	973,0318137	1026
cp3_eff [KJ/Kg*K]	1,123	1,133	1,148	1,158
cpm_3-4_eff [KJ/Kg*k]	1,113375	1,1231	1,13825	1,148

Table 4.12 *Calculated values*

In the same way we did the calculations for the compressor. The calculations on the turbine performances, were made after the gas properties had been previously evaluated. Looking at Table 4.2 R_{gas} was determined and consequently:

$$\begin{cases} \gamma_{gas} = \frac{c_p|_3^4}{(c_p|_3^4 - R_{gas})} \\ k_{gas} = \frac{\gamma_{gas} - 1}{\gamma_{gas}} \end{cases} \quad (4.22)$$

Because Δp_{04} was not taken into account, the coefficient of expansion and the turbine properties were:

$$\begin{cases} \Pi_T = \frac{p_3}{p_4} \\ p_4 = p_0 \end{cases} \quad (4.23)$$

For an isentropic transformation is $T p^{\frac{1-\gamma}{\gamma}} = \text{const}$

$$T_{4is} = T_3 \Pi_T^{\frac{R_{gas}}{c_p}|_3^{4is}} \quad (4.24)$$

Thus

$$H_{Tis} = c_p|_3^{4is} (T_3 - T_{4is}) \quad (4.25)$$

$$H_T = \frac{P_T}{\dot{m}_{gas}} \quad (4.26)$$

Where

$$c_p|_3^{4is} \cong c_p|_3^4 \quad (4.27)$$

Then, Isentropic and Polytropic turbine efficiencies have been calculated

$$\eta_{Tis} = \frac{H_T}{H_{Tis}} \quad (4.28)$$

$$\eta_{Tpol} = \frac{-\log \Pi_T [1 - (1 - \Pi_T^{-k_{gas}}) \eta_{Tis}]}{k_{gas}} \quad (4.29)$$

Moreover the Polytropic index has been evaluated:

$$\frac{1 - \eta_{gas}}{\eta_{gas}} = -\eta_{Tpol} k_{gas} \quad (4.30)$$

Finally the gas turbine's cycle efficiency was obtained, matching the effective output power, the lower heating value and the gas flow rate.

$$\eta_{GT} = \frac{P_{eff}}{\dot{m}_{gas} LHV} \quad (4.31)$$

		Test 1	Test 2	Test 3	Test 4
R_{gas}	[KJ/KgK]	0,28848	0,288487	0,288486	0,288485
γ_{gas}	[-]	1,34971723	1,34565361	1,33948955	1,33563695
		7	4	2	8
(γ_{gas}-1)/γ_{gas}	[-]	0,25910407	0,25686670	0,25344695	0,25129355
		5	8	8	4
p₄	[mbar]	979	979	979	979
Π_t⁻¹	[-]	0,63903394	0,63283775	0,62836970	0,62756410
		3		5	3
Π_T	[-]	1,56486210	1,58018386	1,59141981	1,59346271
		4	1	6	7
T₄_{is}	[K]	763,963616	808,818065	864,938653	912,741128
		5	7	7	9
H_{turbine}	[KJ/Kg]	89,7746068	98,6004049	107,325466	115,810275
		2	8	5	2
H_{turbine}_{is}	[KJ/Kg]	104,642618	113,286435	123,037039	130,149952
		9		4	4
η_{turbine}_{is}	[-]	0,85791628	0,87036373	0,87230208	0,88982187
		5	7	9	9
η_{TG}_{is}	[-]	0,02142254	0,02936366	0,0369274	0,04186015
		9	7		4
η_{turbine}_{pol}	[-]	0,85064687	0,86353858	0,86554931	0,88390537
		9	7	9	7
(1-η_{gas})/η_{gas}	[-]	-0,22040607	-0,2218143	-0,21937084	-0,22211972
b_{fuel}	[Kg/KWh]	3,93553223	2,87120590	2,28310502	2,01406649
		4	6	3	6

Table 4.13 Turbine properties

As seen from the analysis above $\eta_{Tpol} < \eta_{Tis}$ thanks to recovered energy during the expansion process. A fully detailed explanation of this phenomenon is reported in Appendix A2. In the next two chapters it will be demonstrated the final results obtained with the other two diaphragms. As previously stated, Δp_{04} for the expansion ratio assessment were not considered, because they did not influence the final results.

4.4.2 140mm Diaphragm

	Test 1	Test 2	Test 3	Test 4
m_{air}	0,34356	0,33216	0,3263	0,32333
[kg/s]				

W_net [KJ/Kg]	13,09815	20,77312	27,58198	34,17561
Π_c [-]	1,604289	1,615385	1,63005	1,64439
T2_is [K]	340,13	340,68	341,5	342,33
$\eta_{\text{compr_is}}$ [-]	0,679	0,648	0,632	0,653
$\eta_{\text{compr_pol}}$ [-]	0,699493	0,670751	0,65619	0,676219
m_fuel [kg/s]	0,00494	0,00543	0,00583	0,00625
m_gas [Kg/s]	0,34851	0,33759	0,33214	0,32958
λ [-]	4,79294	4,21496	3,85777	3,5678
P_compressor [KW]	22,68	23,27	23,85	23,3
b_fuel [Kg/KWh]	3,952	2,833043	2,332	2,036199
P_lost [KW]	1,35	1,33	1,34	1,35
P_turbine [KW]	28,53	31,5	34,18	35,7
T3_eff [°C]	566,35	640,32	692,63	736,59
T3_eff [K]	839,5	913,47	965,78	1009,74
cp3_eff [KJ/Kg*K]	1,1195	1,1345	1,146	1,1557
cp4 [KJ/Kg*K]	1,107	1,1165	1,1275	1,1365
cpm_3-4_eff [KJ/Kg*K]	1,11325	1,1255	1,13675	1,1461
R_gas [KJ/KgK]	0,28848	0,288487	0,288486	0,288485
γ_{gas} [-]	1,34977	1,344663	1,34009	1,336381
$(\gamma_{\text{gas}}-1)/\gamma_{\text{gas}}$ [-]	0,259133	0,256319	0,253781	0,25171

p4 [mbar]	979,3	979,3	979,3	979,3
Π_t [-]	1,546002	1,559277	1,574594	1,590932
$\eta_{\text{turbine_is}}$ [-]	0,841	0,847	0,865	0,851
$\eta_{\text{turbine_pol}}$ [-]	0,833257	0,839426	0,858082	0,843386
(1-ngas)/ngas [-]	-0,21592	-0,21516	-0,21777	-0,21229
$\eta_{\text{TG_is}}$ [-]	0,021	0,03	0,036	0,041
η_{chamber} [-]	0,841	0,859	0,864	0,866

Table 4.14 *Evaluation of the test bed performances with the 140mm diaphragm*

4.4.3 115,8mm Diaphragm

		Test 1	Test 2	Test 3	Test 4
m _{air}	[kg/s]	0,33478	0,32801	0,3211	0,31402
W _{net}	[KJ/Kg]	13,80011	19,54209	25,97322	36,04866
Π_c	[-]	1,59996	1,600725	1,607736	1,62786
T2 _{is}	[K]	340,56	340,69	340,99	342,09
$\eta_{\text{compr_is}}$	[-]	0,656	0,613	0,601	0,584
$\eta_{\text{compr_pol}}$	[-]	0,677821	0,637522	0,626488	0,611204
m _{fuel}	[kg/s]	0,00512	0,00534	0,00572	0,00639
m _{gas}	[Kg/s]	0,3399	0,33335	0,32682	0,32041
λ	[-]	4,5121	4,23991	3,87213	3,39084
P _{compressor}	[KW]	23,15	24,34	24,47	25,2
P _{lost}	[KW]	1,35	1,34	1,33	1,34
P _{turbine}	[KW]	29,12	32,08	34,14	37,87
T3 _{eff}	[°C]	594,7	639,19	686,35	764,16
T3 _{eff}	[K]	867,85	912,34	959,5	1037,31
cp3 _{eff}	[KJ/KgK]	1,1247	1,1363	1,1245	1,1608
cp4	[KJ/KgK]	1,112	1,114	1,1255	1,1405

cpm_3-4	[KJ/KgK]	1,11835	1,12515	1,125	1,15065
R_gas	[KJ/KgK]	0,28848	0,288487	0,288486	0,288485
γ_{gas}	[-]	1,347621	1,344807	1,344867	1,334605
$(\gamma_{\text{gas}}-1)/\gamma_{\text{gas}}$	[-]	0,257951	0,256399	0,256432	0,250715
p4	[mbar]	979,5	979,5	979,5	979,5
Π_t	[-]	1,546708	1,551812	1,562021	1,58244
$\eta_{\text{turbine_is}}$	[-]	0,833	0,883	0,899	0,914
$\eta_{\text{turbine_pol}}$	[-]	0,824978	0,87701	0,893647	0,909331
$(1-\eta_{\text{gas}})/\eta_{\text{gas}}$	[-]	-0,2128	-0,22486	-0,22916	-0,22798
$\eta_{\text{TG_is}}$	[-]	0,021	0,028	0,034	0,042
η_{chamber}	[-]	0,838	0,856	0,853	0,852
b_fuel	[Kg/kWh]	3,98961	2,999064	2,469065	2,032155

Table 4.15 *Evaluation of the test bed performances with the 115.8mm diaphragm*

Chapter 5

Gas Turbine Performances

Gas turbines have been installed all over the globe, in many countries and in different locations. They work both at sea level or at high altitudes, in winter as in summer, in dry conditions or high humidity. Often they power aircrafts and move from the ground's atmospheric conditions to the limit of Troposphere thirty thousand feet above, observing a performances change. This is not due to a fault of the machine, but because of the different ambient conditions. In order to eliminate such misunderstandings and compare different machines, the gas turbine output and performance is specified at Standard conditions called the ISO ratings. These are specified as per ISO standards 3977-2 (Gas Turbines - Procurement - Part 2: Standard Reference Conditions and Ratings) [11].

5.1 ISO norm performances

ISO (the International Organization for Standardization) [13] is a worldwide federation of national standards bodies (ISO member bodies). Each member body interested in a subject for which a technical committee has been established has the right to be represented on that committee. International organizations, governmental and non-governmental, in liaison with ISO, also take part in the work. ISO 3977-2 defines standard reference conditions as:

- Ambient temperature: 15 [°C]
- Ambient pressure: 101325 [Pa]
- Absence of inlet and outlet pressure loss
- Natural gas fuel (LHV=50000 KJ/Kg) at proper pressure
- Unused machine without fouling
- Relative humidity $\rho=60\%$

In next paragraphs it will be explained how each undesired factor influences the gas turbine performance.

5.2 Factors Affecting Gas Turbine Performance

5.2.1 Ambient temperature

Changes in ambient temperature provoke remarkable effects on gas turbine performance, especially on full-power, heat rate, partial load performance and optimal turbine speed. If the ambient temperature changes, the engine is subject to the following effects:

- The mass flow rate varies in accordance to the specific volume, thus not in proportion to the absolute temperature. If $T_0 = T_1$ rises, p_2 and the compression ratio β drop due to the mass flow rate \dot{m}_{air} and density reduction, as shown in figure 5.1. Therefore increased ambient temperature reduces the power output.

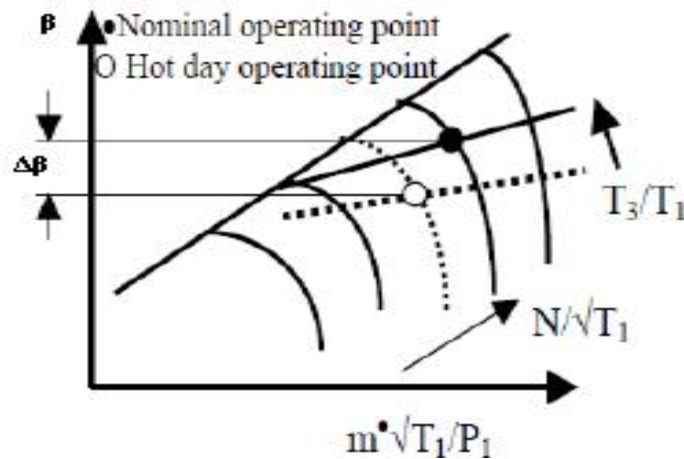


Figure 5.1 Influence of ambient temperature increasing on the operating point

In a single shaft, constant speed gas turbine one would see a constant head (because the head stays roughly constant for a constant compressor speed), and thus a reduced pressure ratio. Because the flow capacity of the turbine section determines the pressure flow firing temperature relationship, an equilibrium will be found at a lower pressure ratio and lower flow, thus a reduced power output.

- The compressor discharge temperature at constant speed increases with increasing temperature. Therefore the amount of heat that can be added to the gas at a given maximum firing temperature is reduced.
- The relevant Reynolds number changes.
- At constant speed and constant TIT, a TOT increasing can be observed thanks to the smaller expansion ratio into the turbine. Ambient temperature increasing makes middle compression phase temperature more similar to the expansion phase middle temperature (see figure 5.2).

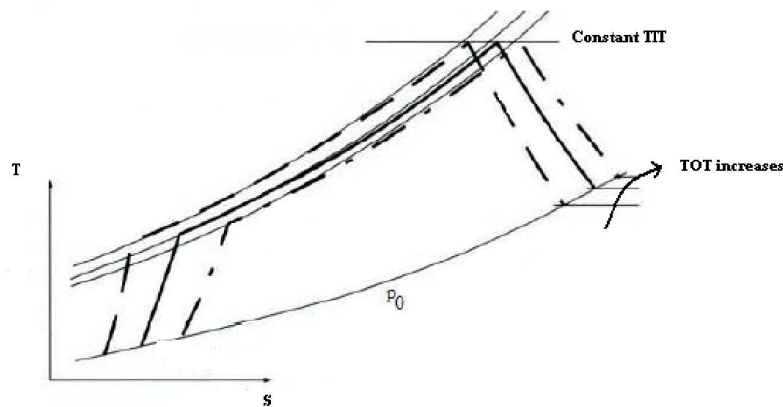


Figure 5.2 Ideal *Joule-Brayton* open cycle *s-T* diagram

Even if it entails a smaller quantity of heat transfer, the consequences of this, are that specific work and efficiency drop.

5.2.1.1 Effects on ROVER 1S/60 performances

Each turbine model has its own temperature-effect curve, as it depends on the cycle parameters and component efficiencies as well as air mass flow.

TU WIEN student Dino Duhovic [14], in two different seasons of 2011 carried out some tests on ROVER 1S/60's test bed in order to estimate the loss in performances caused by the air temperature change. He ran the turbomachine at 2000 output shaft's revolutions per minute, in correspondence of two different ambient temperatures: $T_{0-winter} = 15,6^{\circ}C$ and $T_{0-summer} = 26,2^{\circ}C$. Very small

changes in ambient pressure, produced a $\frac{\Delta P}{P} = \frac{\Delta p_1}{p_1} = -1,542\%$ power loss (for further explanation see paragraph 5.2.2). Inlet and outlet pressure loss have not been taken into account.

The following data analysis showed that the ambient temperature affects the inlet air mass flow rate, the compression ratio, the specific fuel consumption, the turbine outlet temperature, the power and efficiency of the ROVER 1S/60.

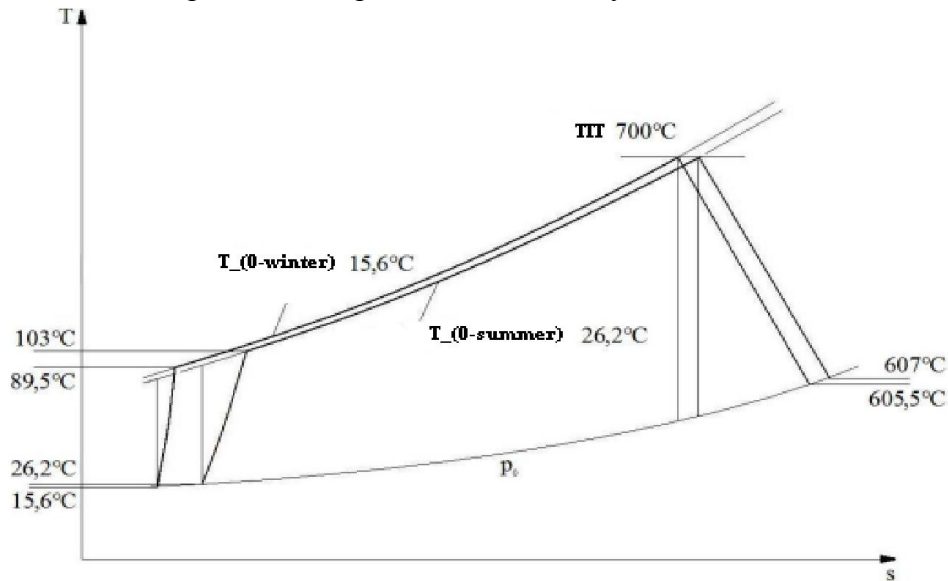


Figure 5.3 Ideal Joule-Brayton open cycle at constant $TIT=700^{\circ}C$ in Duhovic's tests[14]

The Duhovic's data analysis, has shown that small changes in Ambient Temperature returns a high loss in performance. Also in correspondence to $T_3=675^{\circ}C$, power decreases slightly more than global efficiency: $-20,45\%$ and $-17,45\%$ respectively.

Turbine Inlet Temperature T_3 [$^{\circ}C$]	$t_0 = 15,6^{\circ}C$		$t_0 = 26,2^{\circ}C$		rel. Änderung [%]	
	P_{eff} [kW]	η_{eff} [-]	P_{eff} [kW]	η_{eff} [-]	$\Delta P_{eff}/P_{eff}$	$\Delta \eta_{eff}/\eta_{eff}$
600	5,83	0,025	4,05	0,019	-30,57%	-26,59%
625	7,05	0,030	5,29	0,023	-24,90%	-22,00%
650	8,29	0,034	6,47	0,028	-21,98%	-18,82%
675	9,54	0,038	7,59	0,031	-20,45%	-17,46%
700	10,69	0,041	8,61	0,034	-19,48%	-15,89%
715	11,40	0,042	9,20	0,036	-19,30%	-15,49%

Table 5.1 Final results of Duhovic's analysis: influence of Ambient Temperature on Power and Efficiency of ROVER 1S/60, at constant TIT values[14]

5.2.1.2 Sensitivity analysis

The performed sensitivity analysis, permitted him to compare the related loss in power and efficiency at TOT=600°C with the values supplied by Rover Company (Table 5.2). The sensitivity coefficients k_p and k_η result from:

$$\frac{\Delta P}{P} = k_p \Delta T_o [\%] \quad (5.1)$$

$$\frac{\Delta \eta}{\eta} = k_\eta \Delta T_o [\%] \quad (5.2)$$

Rotational speed n=2000U/min		BUILDER	MEASURED
T4 [°C]	ΔT [°C]	$k_p = \Delta P / P / \Delta T [\% / ^\circ \text{C}]$	$k_p = \Delta P / P / \Delta T [\% / ^\circ \text{C}]$
600	26,2-15,6	-1,883	-1,951
T4 [°C]	ΔT [°C]	$k_\eta = \Delta \eta / \eta / \Delta T [\% / ^\circ \text{C}]$	$k_\eta = \Delta \eta / \eta / \Delta T [\% / ^\circ \text{C}]$
600	26,2-15,6	-1,574	-1,559

Table 5.2 ROVER 1S/60's sensitivity coefficients [14]

By the comparison of the data given by some heavy duty gas turbines manufacturers, sensitivity coefficients are smaller for bigger gas turbines. Hence small gas turbines, such as ROVER 1S/60, are more affected by Ambient Temperature variations.

5.2.2 Ambient pressure

The impact of operating the engine at lower ambient pressures (for example due to changing ambient conditions or due to site elevation) is the reduced air density. Therefore the engine sees a reduced mass flow rate (while the volumetric flow is unchanged). The changed density only impacts the power output, but not the efficiency of the engine ($\frac{\Delta \eta}{\eta} = 0$), because the cycle's shape and temperatures stay constant (figure 5.3): cycle is simply moved on the right.

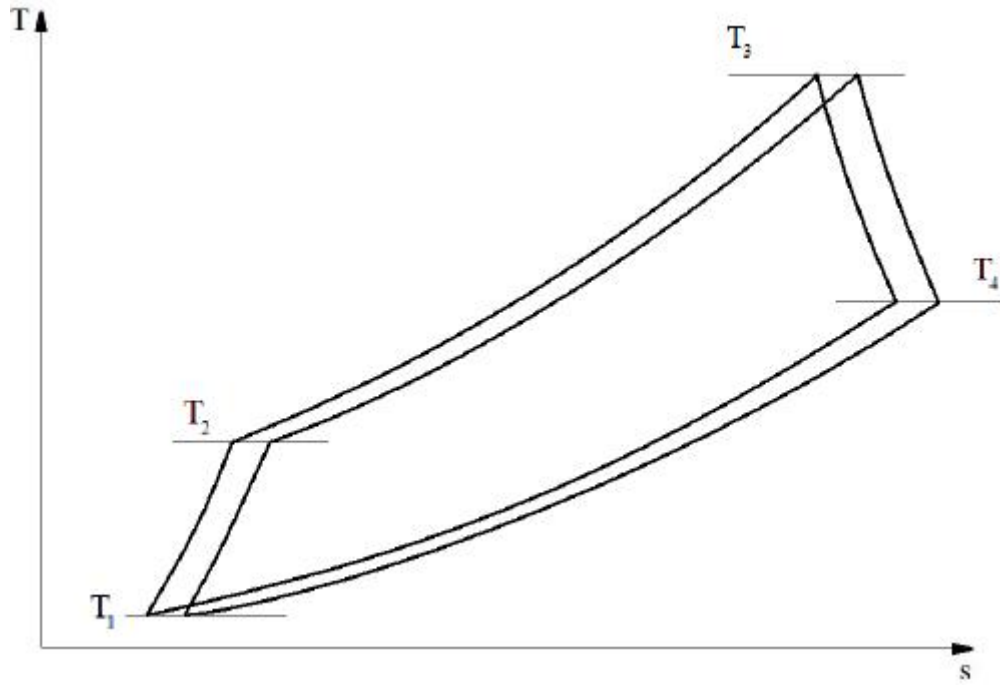


Figure 5.4 *Effects of ambient pressure lowering*

The output power lowering demonstration can be explained in those terms [14]:

$$P_{eff} = \dot{m}_{air} w_{net} \quad (5.3)$$

Thus

$$P_{eff} = \rho_1 \dot{V}_1 w_{net} \quad (5.4)$$

Adopting the ideal gas law:

$$P_{eff} = \frac{p_1}{R T_1} \dot{V}_1 w_{net} \quad (5.5)$$

Therefore, the derivative of P_{eff} leads up to:

$$\frac{\partial P_{eff}}{\partial p_1} = \frac{\dot{V}_1 W_{net}}{R T_1} = \frac{P_{eff}}{p_1} \quad (5.6)$$

And finally:

$$\frac{\partial P_{eff}}{P_{eff}} = \frac{\partial p_1}{p_1} \quad (5.7)$$

As shown in final equation (5.7), when ambient pressure drops, output power drops as well.

5.2.3 Humidity

Similarly, humid air, which is less dense than dry air, also affects output and heat rate, as shown in Figure 5.5. In the past, this effect was thought to be too small to be considered. However, with the increasing size of gas turbines and the utilization of humidity to bias water and steam injection for NOx control, this effect has greater significance.

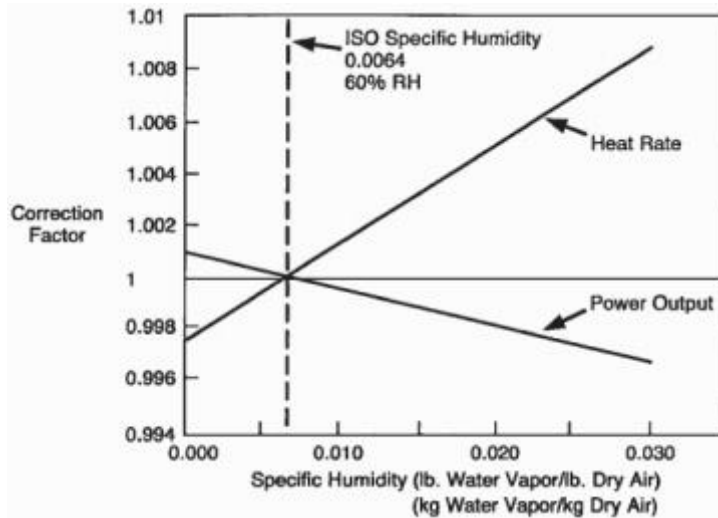


Figure 5.5 Humidity effect curve for an heavy duty gas turbine [15]

5.2.4 Inlet & outlet pressure loss

Any gas turbine needs an inlet and an exhaust system to operate. Usually for heavy duty and aeroderivative turbogas machines the inlet system consists one

or several filtration systems, a silencer, ducting, fogging, deicing, evaporative and other cooling systems. The exhaust system may include a silencer, ducting and waste heat recovery systems. All these systems will cause pressure drops, so that the engine will be subject to an inlet pressure that is lower than ambient pressure and will exhaust against a pressure that is higher than the ambient one. These inevitable pressure losses in the inlet and exhaust systems cause a reduction in power and cycle efficiency.

The TU WIEN test bed shows a lower complexity. However concentrated inlet pressure loss across the diaphragm and distributed pressure loss alongside the inlet pipe, have caused essential changes in power and efficiency of the ROVER 1S/60. Inlet pressure loss could be seen as an isenthalpic transformation (see figure 5.6), thus it caused the mass flow rate reduction and consequently a power drop. Even if it provoked, across the turbine, an expansion ratio reduction, it did not change the compression ratio through the compressor. The expansion ratio drop, influenced the output power and the thermal efficiency.

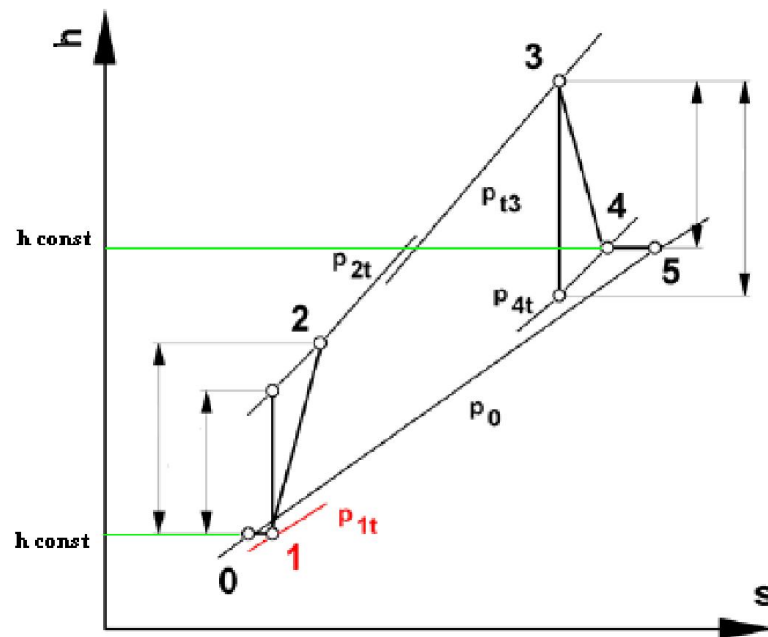


Figure 5.6 *Inlet and outlet pressure loss such as isenthalpic transformations*

Nevertheless in this final Thesis work the outlet pressure loss Δp_{04} was not accounted for due to its very small value. Its contribution to the global performance deterioration could be considered almost negligible.

The next will discuss the most important final results of the data analysis.

Chapter 6

Influence of Inlet Pressure Loss on the ROVER 1S/60s's Performances

In paragraph 4.4 the ROVER 1S/60 performance is calculated as a result of many different calculations. In the next paragraphs it will be explained the way inlet pressure loss influences the micro gas turbine power and efficiency and how it makes the global machine performance worse. As previously shown, usually many other phenomena such as ambient temperature and pressure changing, or outlet pressure drop, cause a generalized deterioration of performances. However this work tried to keep constant as much functioning parameters as possible, in order to focus attention only on performance changes caused by inlet pressure loss. The experimental outcomes will be compared to the results obtained by a theoretical model, supplied by the fluid machine department's Professor Reinhard Willinger. Hence they will be compared to the results obtained for an heavy duty gas turbine. The comparison between the experimental results and the theoretical ones will show a quasi perfect fitting.

6.1 Experimental results

6.1.1 Varying T_3

The data processing made in chapter 4 permitted to obtain the ROVER's values of performance. Figures 6.1 and 6.2 represent the ROVER's Nett Power and Thermal Efficiency trends as a consequence of changing in operating load conditions and therefore in TIT (T_3) values.

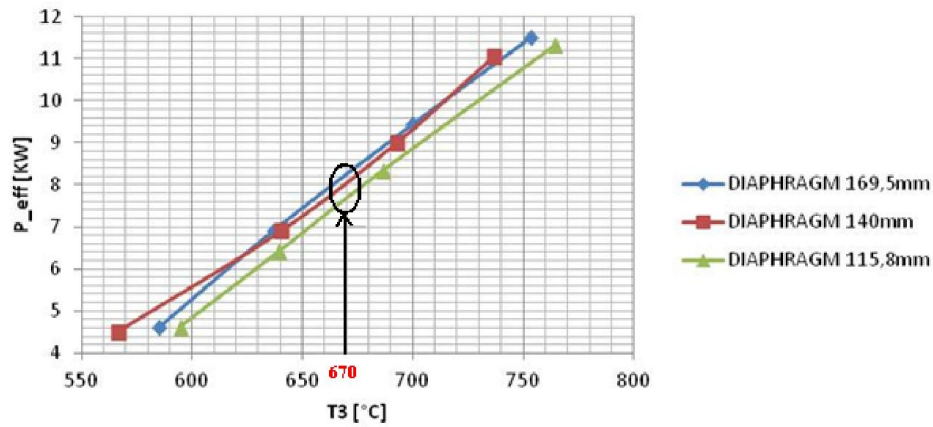


Figure 6.1 *Changing in Nett Power performance as a consequence of TIT variation*

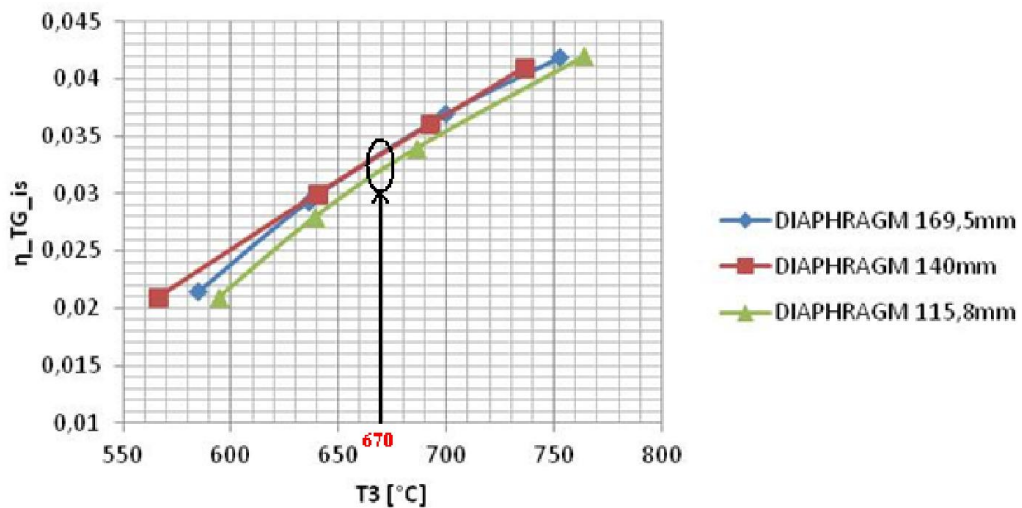


Figure 6.2 *Changing in global thermal efficiency as a consequence of TIT variation*

The TIT variation is caused by the increasing in operating load parameters during the test phase. Furthermore focusing on a single orifice plate, as the T_3 value increases, global turbomachine performance increases accordingly as shown in Figure 6.1 and 6.2. However, the global performance changes from diaphragm to diaphragm due to the different induced mean value of inlet pressure loss. Partial load functioning conditions always worsen the engine power and efficiency. These diagrams highlight the low values in power and

efficiency due to the partial load functioning conditions. Values of 45KW in power and 0.13 in efficiency at full load (see Table 2.2) are far to be reached.

The mass flow rate \dot{m}_{air} through the diaphragm drops (Figure 6.3), as a consequence of changing in load operating conditions.

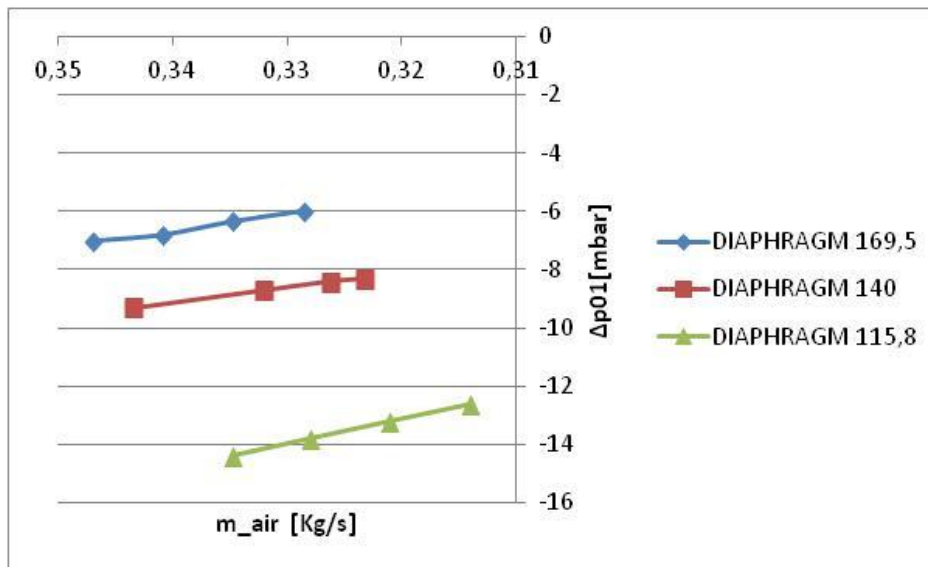


Figure 6.3 Mass flow rate decreases as soon as inlet pressure loss arises

Moving towards higher load operating conditions, the inlet pressure loss decreases (figure 6.4), therefore the absolute inlet pressure p_1 rises.

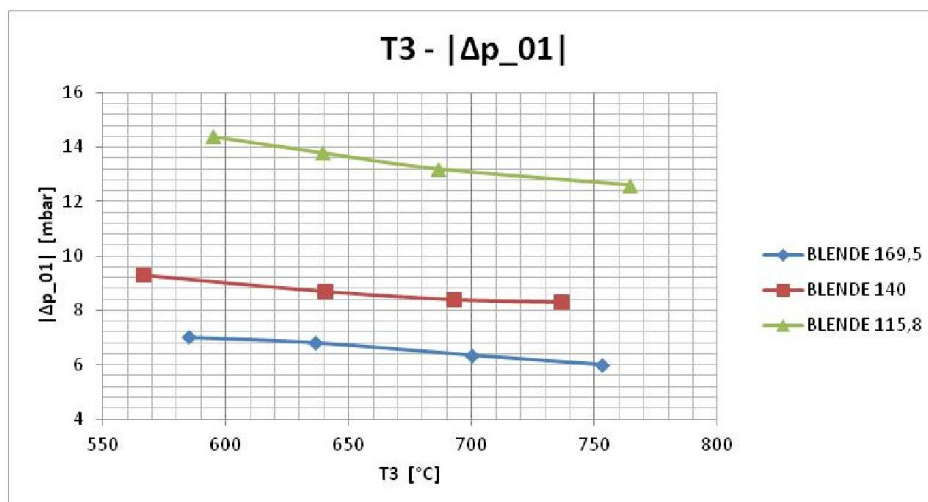


Figure 6.4 Inlet pressure loss drops when operational load increases or diaphragm's diameter decreases

Starting from test one up to test four, we noticed that the absolute fuel consumption increases, so that the Air Fuel equivalence Ratio λ decreases (Figure 6.5) and the gas mixture became richer.

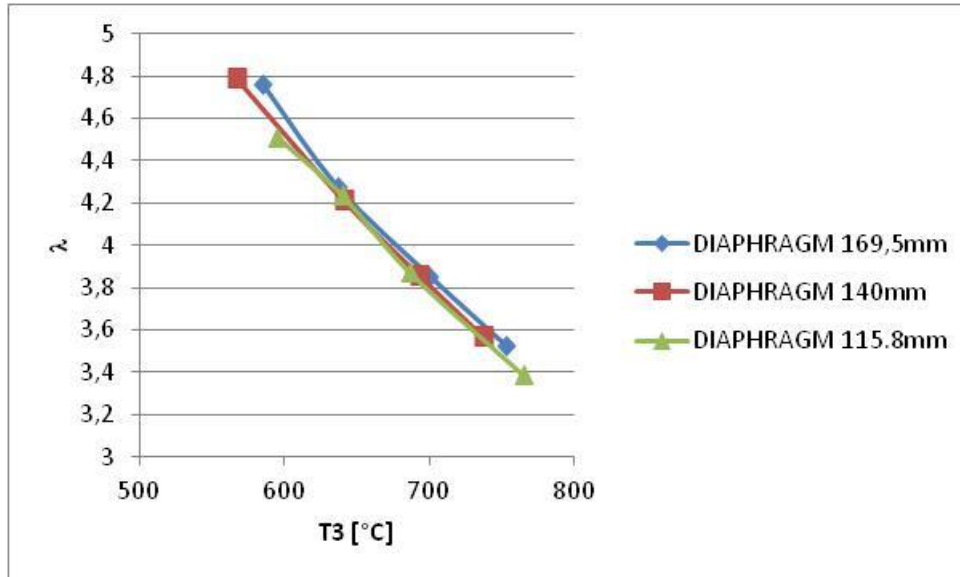


Figure 6.5 Air Fuel equivalent Ratio drops in correspondence of higher T3

Nevertheless, as shown in Figure 6.6 the specific fuel consumption b [kg/KWh] decreases moving to higher loads.

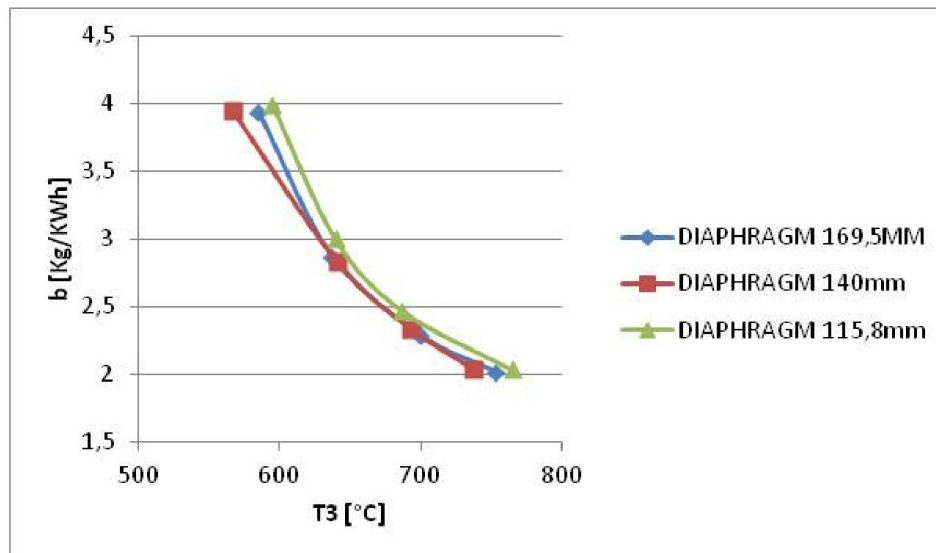


Figure 6.6 Specific fuel consumption drops when load increases

6.1.2 Keeping T_3 constant

However the aim was to evaluate the fall in performances keeping the other parameters as much constant as possible. Constancy of TIT in correspondence to each operating load point (also called test point), has permitted to evaluate the first negative impact of inlet pressure loss on air mass flow ratio (Figure 6.7).

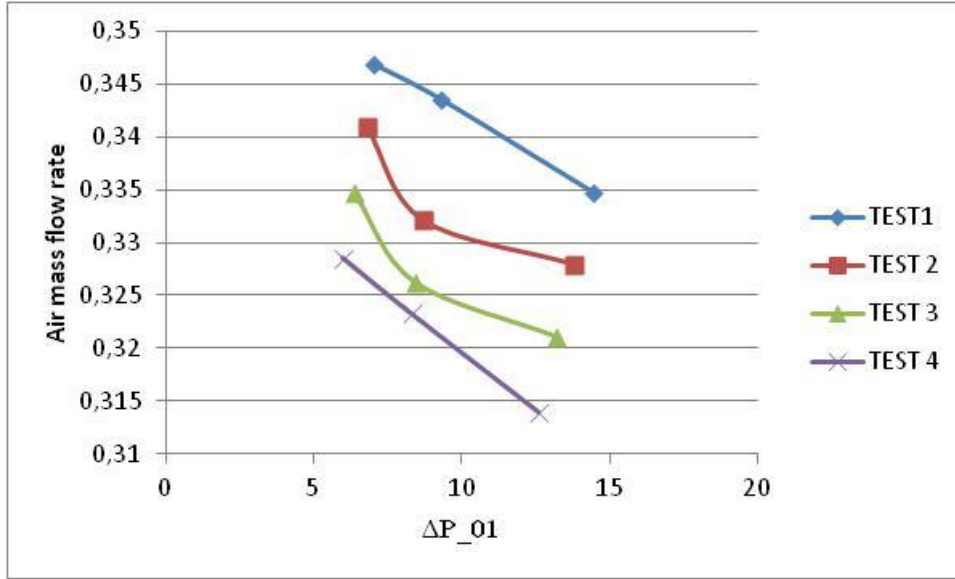


Figure 6.7 Inlet pressure loss increase modifies the inlet air mass flow rate

As the diaphragm's diameter was reduced (169,5mm→140mm→115,8mm), the inlet pressure loss increased while the absolute inlet pressure p_1 and the mass flow rate \dot{m}_{air} decreased. Therefore thanks to the constancy in the ambient temperature $T_0 = T_1 = const$, the reduced mass flow rate parameter $\frac{\dot{m}_{air} \sqrt{T_1}}{p_1}$, can be approximately assumed constant in correspondence to each diaphragm (Figure 6.8):

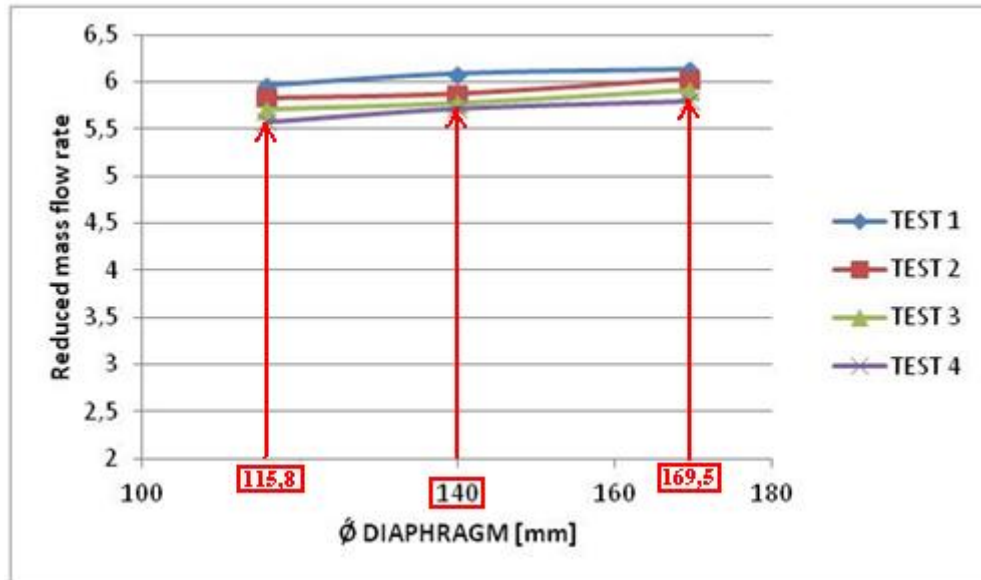


Figure 6.8 *Small variations in the reduced mass flow rate coefficient can be ignored*

In order to only evaluate the impact of inlet pressure losses on ROVER 1S/60 performance, the other parameters were considered as much constant as possible. One of the most significant hypothesis which the entire Thesis work is based on, is the constancy of the parameters. The attempt was to modify only the inlet pressure loss values, keeping the other quantities as much steady as possible. Because of TIT changed going through different operating load conditions, the value $T_3=670^{\circ}\text{C}$ was chosen as the reference temperature for next calculations.

As mentioned before, thanks to the constant value of $\frac{T_3}{T_1}$ ratio and the constant reduced number of revolutions $\frac{n}{\sqrt{T_1}}$, thus the reduced mass flow rate can be assumed constant in correspondence to each test point.

Taking the mean value of the inlet pressure loss Δp_{01} for each diaphragm and the value of power and efficiency at $T_3=670^{\circ}\text{C}$ (see Table 6.1), the graphs reported in Figures 6.9 and 6.10 were obtained.

	$ \Delta p_{01} $ mean value [mbar]	P_{eff} [KW] @ $T_3=670\text{ }^{\circ}\text{C}$	η_{TG} @ $T_3=670\text{ }^{\circ}\text{C}$
DIAPHRAGM 169,5mm	6,5375	8,32	0,0338
DIAPHRAGM 140mm	8,675	8	0,0334
DIAPHRAGM 115,8mm	13,5	7,7	0,0321

Table 6.1 ROVER's performance changes adopting different diaphragms

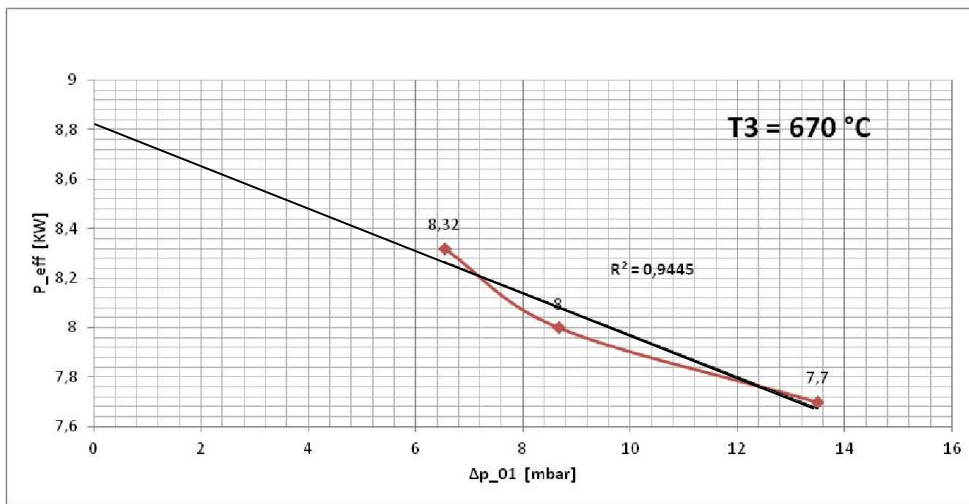


Figure 6.9 Negative influence of inlet pressure loss on gas turbine's power

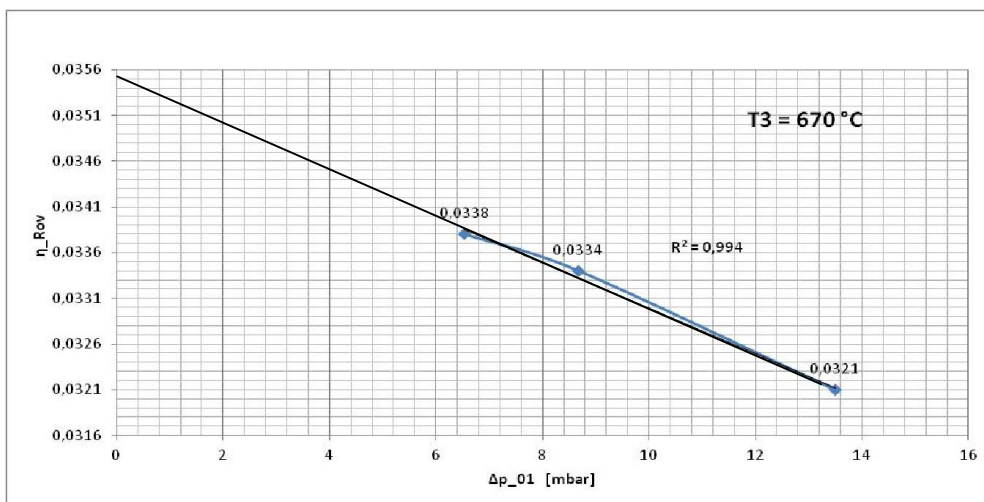


Figure 6.10 *Negative influence of inlet pressure loss on gas turbine's efficiency*

Previous Figures also show the negative impact on total performances due to the inlet pressure loss for a reference $T_3=670^\circ\text{C}$. As soon as Δp_{01} rises, power and efficiency drop.

In order to estimate the ideal value of Power and Efficiency for zero value Δp_{01} , the previous curve have also been interpolated with a linear trend curve. The straight line well fits the experimental data and it gives

- $P_{eff}|_{\Delta p_{01}=0} = 8,81 \text{ KW}$
- $\eta_{Rover}|_{\Delta p_{01}=0} = 0,0355$

in correspondence to absence of inlet pressure loss.

6.2 Modelling of phenomenon

In order to properly describe the influence of inlet pressure loss on ROVER 1S/60 power and efficiency, an analytical model has been developed inside TU WIEN. In next paragraphs the model hypothesis, the equations and the final results will be illustrated.

6.2.1 Model's hypothesis

The model that describes the way inlet pressure loss influences power and efficiency, is based on simple hypothesis:

1. **Constancy of cp:** the specific heat at constant pressure was considered constant from the inlet section up to the exhaust pipe. For ideal cycle analysis of gas turbines it is common to assume that cp and the specific heat ratio are constant throughout the process. This hypothesis is validated by a small pressure ratio and low values in TIT and TOT (see paragraph 4.3).

2. **Turbine pressure ratio** was influenced only by inlet pressure loss. Pressure loss through the combustion chamber and exhaust pressure loss were considered equal to zero. In the presence of annular combustors and absence of an exhaust filters, this remarkable hypothesis can be considered acceptable.
3. **Constancy of reduced mass flow rate:** $\frac{\dot{m}\sqrt{T_1}}{p_1} = const$
4. **Constancy of ambient temperature:** $T_0 = T_1 = const.$ in correspondence of different inlet pressure loss values.

6.2.2 Model's equations

The Nett output work W_N is deduced by the difference between the turbine's output work and the compressor's inlet work:

$$W_N = W_T - W_C \quad (6.1)$$

$$W_N = \eta_{T_is} c_p^T T_3 \left(1 - \Pi_T^{\frac{1-\gamma}{\gamma}} \right) - \frac{1}{\eta_{C_is}} c_p^C T_1 \left(\Pi_C^{\frac{\gamma-1}{\gamma}} - 1 \right) \quad (6.2)$$

Using the first hypothesis $c_p^T = c_p^C = c_p$ and the second hypothesis, thus the equation 6.2 becomes:

$$\frac{W_N}{c_p T_1} = \eta_{T_is} \frac{T_3}{T_1} \left\{ 1 - [(1 - \xi) \Pi_C]^{\frac{1-\gamma}{\gamma}} \right\} - \frac{1}{\eta_{C_is}} \left(\Pi_C^{\frac{\gamma-1}{\gamma}} - 1 \right) \quad (6.3)$$

Where $\xi = \frac{|\Delta p_{01}|}{p_0}$ represents the inlet pressure loss contribution and γ is the Isentropic index.

I renamed $\frac{W_N}{c_p T_1} = W_N^*$ and then its derivative on ξ , is:

$$\frac{\partial W_N^*}{\partial \xi} = dW_N^* = \eta_{T_is} \frac{T_3}{T_1} \left(\frac{1-\gamma}{\gamma} \right) [(1 - \xi) \Pi_C]^{\frac{1-2\gamma}{\gamma}} \Pi_C \quad (6.4)$$

If $\xi=0$ means that inlet pressure loss is equal to zero, and equation (6.4) becomes:

$$dW_N^*|_{\xi=0} = \eta_{T_{is}} \frac{T_3}{T_1} \left(\frac{1-\gamma}{\gamma} \right) [\Pi_C]^{\frac{1-2\gamma}{\gamma}} \Pi_C \quad (6.5)$$

Therefore:

$$dW_N^*|_{\xi=0} = \eta_{T_{is}} \frac{T_3}{T_1} \left(\frac{1-\gamma}{\gamma} \right) \Pi_C^{\frac{1-\gamma}{\gamma}} \quad (6.6)$$

One of most important results of this demonstration, is the linear connection that exists between the inlet pressure loss and the ratio of ROVER 1S/60's efficiency:

$$\frac{\eta_{Rover}}{\eta_{Rover}|_{\xi=0}} = \frac{W_N / c_p T_1}{W_N / c_p T_1 \Big|_{\xi=0}} \quad (6.7)$$

Thus

$$\frac{\eta_{Rover}}{\eta_{Rover}|_{\xi=0}} = \frac{W_N^*|_{\xi=0} + dW_N^*|_{\xi=0} \xi}{W_N^*|_{\xi=0}} = 1 + \alpha \xi \quad (6.8)$$

$$\frac{\eta_{Rover}}{\eta_{Rover}|_{\xi=0}} = 1 + \alpha p_0 |\Delta p|_{01} \quad (6.9)$$

Where $\alpha = \frac{dW_N^*|_{\xi=0}}{W_N^*|_{\xi=0}}$ is the negative angular coefficient of the straight line.

The connection between inlet pressure loss and ROVER's power can be represented with a straight line as well. The proof starts from the definition of the ratio of power P .

$$\frac{P_{Rover}}{P_{Rover}|_{\xi=0}} = \frac{\dot{m} W_N}{\dot{m}|_{\xi=0} W_N|_{\xi=0}} \quad (6.10)$$

Referring to hypothesis number three and four, the reduced mass flow rate in presence of inlet pressure loss is equal to the reduced mass flow rate when inlet pressure loss is equal to zero.

$$\frac{\dot{m} \sqrt{T_1}}{p_1} = \frac{\dot{m} \sqrt{T_1}}{p_1} \Big|_{\xi=0} \quad (6.11)$$

$$\frac{\dot{m}}{\dot{m}|_{\xi=0}} = \frac{p_1}{p_1|_{\xi=0}} = \frac{p_1|_{\xi=0} - |\Delta p_{01}|}{p_1|_{\xi=0}} \quad (6.12)$$

Therefore

$$\begin{cases} \frac{\dot{m}}{\dot{m}|_{\xi=0}} = 1 - \frac{|\Delta p_{01}|}{p_1|_{\xi=0}} = 1 - \xi \\ p_1|_{\xi=0} = p_0 \end{cases} \quad (6.13)$$

At this stage Equation (6.10) can be rewritten as:

$$\frac{P_{Rover}}{P_{Rover}|_{\xi=0}} = (1 - \xi)(1 + \alpha \xi) \quad (6.14)$$

At the second member the element of second order has been discarded. Finally equation (6.14) becomes

$$\frac{P_{Rover}}{P_{Rover}|_{\xi=0}} = 1 - (1 - \alpha)\xi \quad (6.15)$$

Equals to:

$$\frac{P_{Rover}}{P_{Rover}|_{\xi=0}} = 1 - (1 - \alpha) p_o^{-1} |\Delta p|_{01} \quad (6.16)$$

This model explains that as soon as inlet pressure loss increases, thus $\frac{\eta_{Rover}}{\eta_{Rover}|_{\xi=0}}$ and $\frac{P_{Rover}}{P_{Rover}|_{\xi=0}}$ decrease their values with a linear trend. However $\frac{P_{Rover}}{P_{Rover}|_{\xi=0}}$ decreases more rapidly than $\frac{\eta_{Rover}}{\eta_{Rover}|_{\xi=0}}$, due to a higher angle coefficient $-(1 - \alpha)$.

6.2.3 Model fitting to experimental data

Model

As shown in Table 6.2, all inputs necessary for the equations (6.8) and (6.15) were calculated adopting the experimental data obtained during the test campaign in correspondence of a constant TIT value of $T_3 = 670$ °C.

DIAPHRAGM	169,5mm	140mm	115,8mm
$\eta_{C_{is}} @ T_3 = 670$ °C	0,615	0,635	0,605
$\eta_{T_{is}} @ T_3 = 670$ °C	0,871	0,858	0,895
$ \Delta p _{01} [mbar] @ T_3 = 670$ °C	6,5	8,45	13,4
$T_0 = T_1 [^{\circ}C]$	295,35	295,55	295,45
$\Pi_C @ T_3 = 670$ °C	1,669	1,623	1,6045
$\frac{1 - \gamma}{\gamma} @ T_3 = 670$ °C	-0,2551	-0,255	-0,2567
ξ	0,006639	0,008629	0,013680
W_N^*	0,10957	0,10573	0,10429
$W_N^* _{\xi=0}$	0,113721	0,111085	0,113252
$dW_N^* _{\xi=0}$	-0,622621	-0,617067	-0,649584

α	-5,47	-5,55	-5,74
----------	-------	-------	-------

Table 6.2 *Input model's data*

The value of α can be assumed to be quite constant varying the inlet pressure loss. Hence the mean α value ($\alpha = -5,8861$) has been adopted into the equation (6.8) and (6.15).

Finally, the power and efficiency ratios have been calculated. Table 6.3 shows the final results as a consequence of the model implementation.

$\frac{\eta_{Rover}}{\eta_{Rover} _{\xi=0}}$	0,963	0,952	0,922
$\frac{P_{Rover}}{P_{Rover} _{\xi=0}}$	0,956	0,943	0,91

Table 6.3 *Final model results*

Experiment

The experimental power and efficiency ratios were calculated thanks to the experimental data reported in Table 6.4 and thanks to the values of power and efficiency estimated in correspondence to a zero value of inlet pressure loss.

$\frac{\eta_{Rover}}{\eta_{Rover} _{\xi=0}}$	0,9521	0,941	0,904
$\frac{P_{Rover}}{P_{Rover} _{\xi=0}}$	0,944	0,908	0,087

Table 6.4 *Experimental ratios*

The previous results demonstrate that Power decreases faster than Efficiency, both for model and experiment. The reason for this is explained into the model;

indeed for efficiency ratio, ξ is multiplied by α (eq.6.8). On the contrary for the power ratio, ξ is multiplied by $-(1 - \alpha)$ (eq.6.15). Due to the negative value of α , thus $|-(1 - \alpha)| > |\alpha|$. Hence power is more affected by inlet pressure loss than the efficiency.

This important observation is confirmed by the experimental results. Furthermore the experimental ratios follow a linear trend as well as the model outcomes (Figures 6.11-6.12)

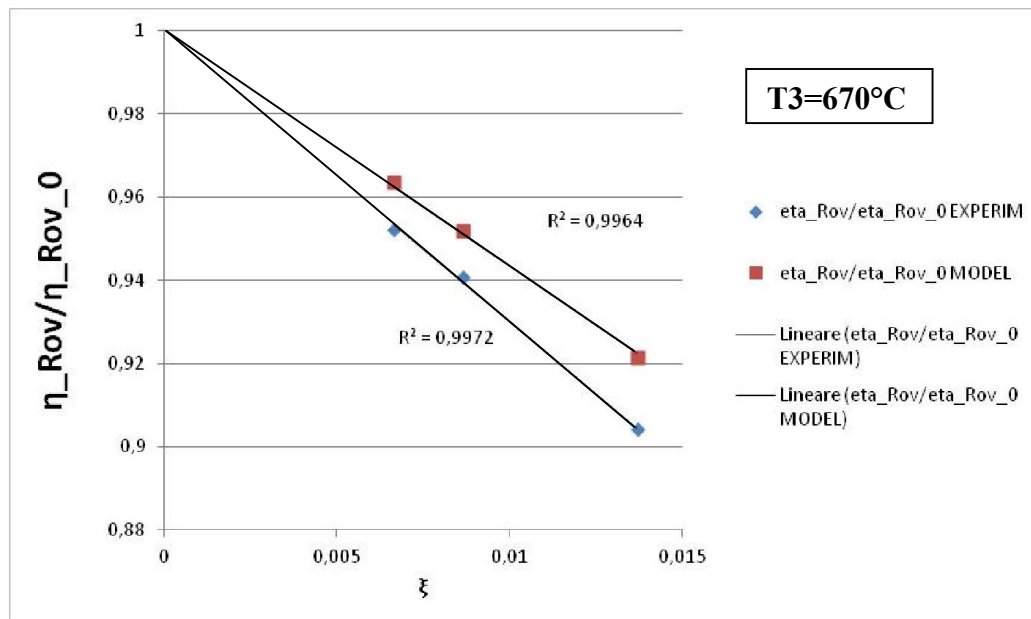


Figure 6.11 *Model and experimental Efficiency ratios as a function of ξ*

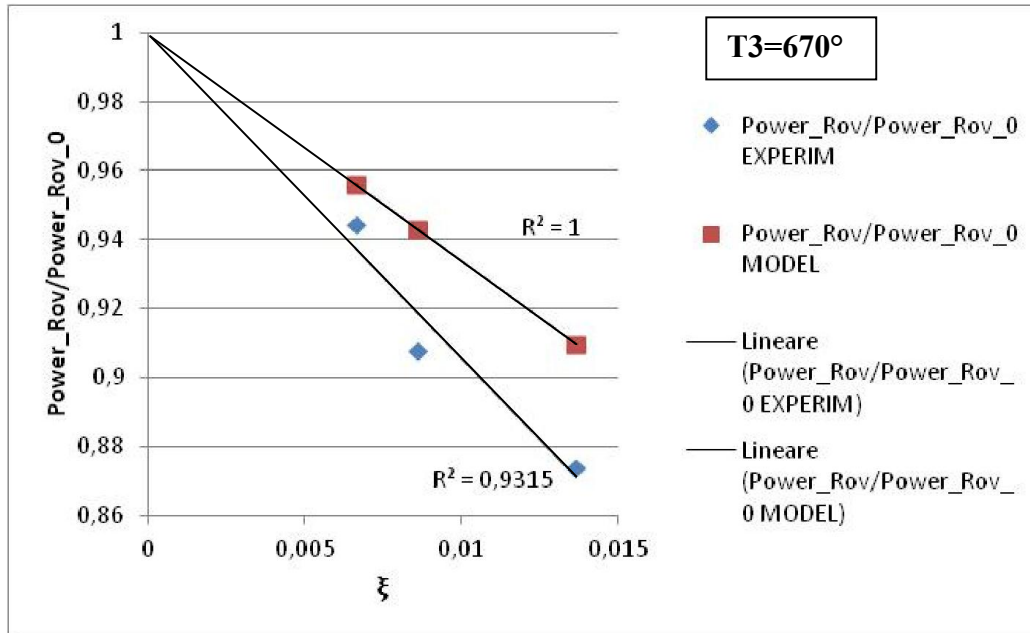


Figure 6.12 Model and experimental Power ratios as a function of ξ

Those information can be also reported on other two diagrams which represent the influence of inlet pressure loss on power and efficiency ratios as a function of $|\Delta p|_{01}$.

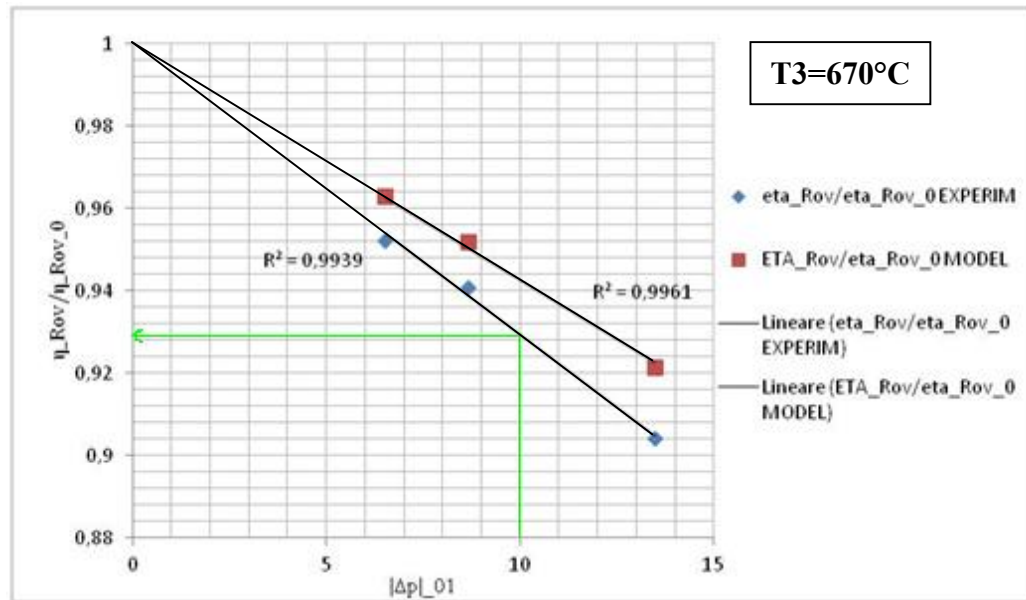


Figure 6.13 Model and experimental Efficiency ratio as a function of $|\Delta p|_{01}$

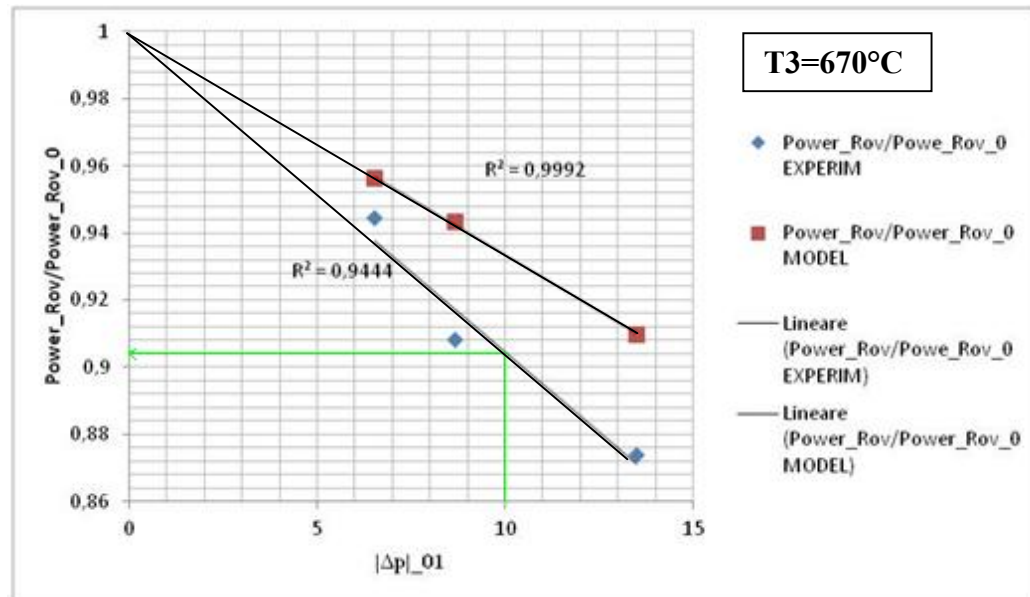


Figure 6.14 Model and experimental Power ratio as a function of $|\Delta p|_{01}$

All these figures permit to say that as soon the diaphragms' diameter drops as the performances drop linearly; in fact the experimental results fit the straight line very well. There is no too much difference between the theoretical model and the experimental results.

From Figures 6.13 and 6.14 it is clearly visible that in correspondence to $|\Delta p|_{01} = 10$ [mbar] the loss in performance is almost 8,7% and 7% for power and efficiency respectively.

6.3 Comparison with the results obtained for a heavy duty gas turbine

The heavy duty GE MS7001EA gas turbine's experimental data [15] demonstrate smaller power and efficiency drops in correspondence to $|\Delta p|_{01} = 10$ [mbar]. The percentage performance reduction is 0,7% and 1,8% for efficiency and power respectively (Figure 6.15). Hence, it comes clear that a micro gas turbine such as the ROVER 1S/60 is more affected by negative inlet pressure loss effect than a large size gas turbine.

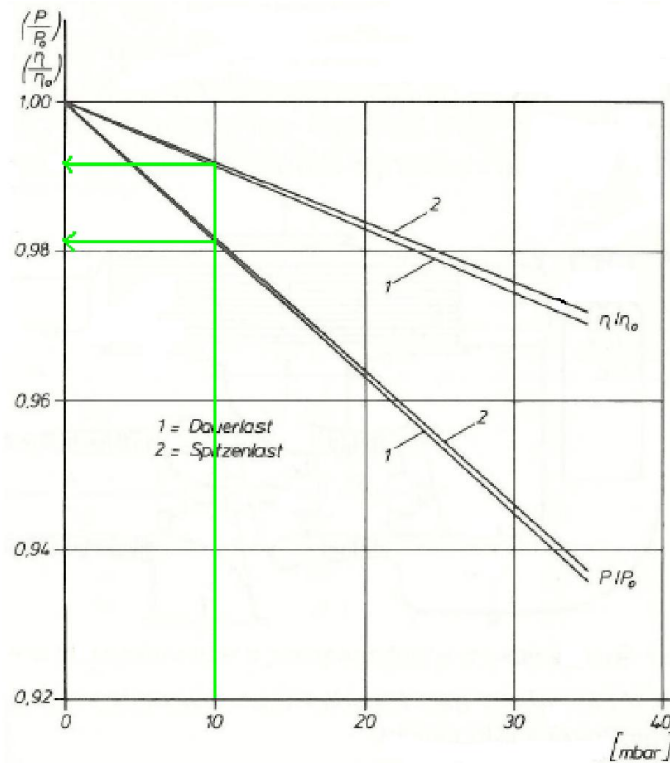


Figure 6.15 Influence of inlet pressure loss on power and efficiency of a heavy duty GE MS7001EA gas turbine.

The reason for this can be explained looking at the higher compression ratio ($\Pi_{GE\ MS7001EA} = 14,6$) and TIT ($\approx 1200^\circ\text{C}$) reached by the heavy duty gas turbine.

Conferring reference values of 0,9 to the compressor and turbine efficiency, 1,4 to the isentropic coefficient, 15 to the compression ratio and 5 to the $\frac{T_3}{T_1}$ ratio, then they can be used into the theoretical model. Hence the model equations lead to $|\alpha_{HeavyDuty}| = 0,526$. This value is much smaller than the $|\alpha_{ROVER1S/6}| = 5,6$. Alpha weighs the influence of inlet pressure loss and on global performance, therefore an higher value means higher loss.

6.4 Conclusions

The Thesis work here presented has permitted to describe the way inlet pressure loss affects the global performance of a ROVER1S/60 micro gas turbine. It must be considered as the start point also for future works, such as the way

measurement uncertainties can affect the experimental data acquisition process. Anyway, in this work, the experimental results have been compared to a simple analytical model. This theoretical model did not have the claim to perfectly describe and predict the gas turbine response as a consequence of inlet pressure loss, but only to give a general trend.

The model's hypothesis simplifications have been made possible thanks to the low values of ROVER1S/60's compression ratio, TIT, combustion and outlet pressure loss. More powerful turbines have higher pressure ratios, pressure losses, TIT and hence high variation of thermodynamic parameters.

For these reasons the observance of the boundary conditions is fundamental in order to make the model application reasonable.

However, as previously shown, the model outcomes for the ROVER 1S/60 micro gas turbine, are not so far from the experimental results, so that its use make of it a powerful tool for students education and understanding of machine behavior.

Notation

List of Symbols

α	Air fuel ratio
γ	Ratio of specific heats
Δp	Differential static pressure
ε	Compressibility factor
η	Efficiency
λ	Air fuel Equivalence Ratio
μ	Slip factor
χ	Mass flow rate coefficient
Φ	Fuel Air equivalence Ratio
Π	Pressure ratio
ρ	Fluid density
τ	Time fuel consumption
b	Specific fuel consumption
c_p	Specific heat at constant pressure
c_v	Specific heat at constant volume
d	Internal Diaphragm's diameter
g	Acceleration of gravity
h	Enthalpy
\dot{m}	Mass flow rate
n	Polytropic exponent of the gas
p	Absolute pressure
r	Blade radius
u	Internal energy
w	Flow speed
z	Altitude

A	Surface area
C	Coefficient of discharge
D	Inlet pipe's diameter
H	Specific head
N_B	Number of rotor blades
P	Power
R	Universal gas constant
T	Temperature
\dot{V}	Volume flow rate
V_t	Tangential component of absolute flow speed
V_a	Axial component of absolute flow speed
W	Work

References

- [1] A Whitfield, N.C. Baines: *Design of radial Turbomachines*, Longman Scientific&Technical, first edition, 1990
- [2] C.Osnaghi, *Teoria delle turbomacchine*, Progetto Leonardo, Bologna, ristampa 2006
- [3] J.Jayasuria, A.Manrique, *Laboratory notes -A gas turbine combustor exercise-*, Royal Institute of Technology, Stockholm, 2005
- [4] E.A.Simonis, J.Reeman, *Gas Turbine Design Based on Free Vortex Flow*, Reports and Memoranda No.2541, May 1944
- [5] M.Januschewsky, *Modernisierung eines Gasturbinenprüfstandes*, Master Thesis, TU WIEN, November 2009
- [6] A.Benoni,R Willinger, *Unterlagen zur Laborübung "Gasturbinenkennlinie – ROVER 1S/60"*, TU WIEN, October 2010
- [7] <http://www.sensorsone.co.uk/pressure-measurement-glossary/pressure-transducer.html>
- [8] EN ISO 5167-1, *Measurement of fluid flow by means of pressure differential devices inserted in circular cross section conduits running full*, Part 1 General principles and conditions, 2003
- [9] EN ISO 5167-2, *Measurement of fluid flow by means of pressure differential devices inserted in circular cross section conduits running full*, Part 2 Orifice plates, 2003
- [10] VDE-VDE 20141, *Durchflußmessung mit Drosselgeräten –Blenden und Düsen für besondere Anwendungen*, 2001
- [11] <http://www.brighthubengineering.com>
- [12] I.Martinez, *Combustion thermodynamic*, 2014
- [13] <http://www.iso.org>

- [14] D.Duhovic, *Einfluss der Umgebungstemperatur auf Leistung und Wirkungsgrad einer klein Gasturbine*, Master Thesis, TU WIEN, April 2011
- [15] Frank J.Brooks ,*GE Gas Turbine Performance Characteristics*, GE Power Systems, Schenectady NY

Appendix A1

Eulerian work

The Eulerian work (equation A1.1) is the real work transferred from the fluid to the rotor blades or contrary from the rotor blades to the fluid. It includes a small energy friction loss in correspondence to the blade entrance and exit. However this small energy loss can be omitted.

$$W_u = U_2 V_{2t} - U_1 V_{1t} \quad (\text{A1.1})$$

Where number 1 and 2 represents the entrance and exit borders. This equation shows the importance of peripheral rotor speed U mostly for radial impeller and the component of the absolute velocity V acting in peripheral direction. There is a second way to write the Eulerian work:

$$W_u = \frac{V_2^2 - V_1^2}{2} - \frac{U_2^2 - U_1^2}{2} - \frac{W_2^2 - W_1^2}{2} \quad (\text{A1.2})$$

The second member of equation (A1.2) contains three terms which represent the Kinetic energy changing, the Potential energy changing and the Reaction effect respectively.

The Eulerian work is closely related to the Total Enthalpy h_T . If we consider only the blades entrance and exit, and no other rotating surfaces, thus equation (A1.1) can be written as:

$$\Delta h_T = U_2 V_{2t} - U_1 V_{1t} \quad (\text{A1.3})$$

And for steady flow hypothesis $V_1=V_2$, equation (A1.3) becomes:

$$h_2 - h_1 = g(z_1 - z_2) - \frac{U_1^2 - U_2^2}{2} + \frac{W_1^2 - W_2^2}{2} \quad (\text{A1.4})$$

$$h_R = h + g z - \frac{U^2}{2} + \frac{W^2}{2} = \text{const.} \quad (\text{A1.5})$$

Hence, the Total Enthalpy throughout a rotor stage (also called Rothalpy) keeps constant.

Appendix A2

Polytropic Efficiency

In this Appendix, I 'm going to describe the importance of Polytropic Efficiency for Joule-Brayton cycles.

Polytropic Efficiency permits to estimate the machine's efficiency without taking into account the compressibility effects of the working fluid. Focusing the attention on Figure A2.1, it shows a real adiabatic compression.

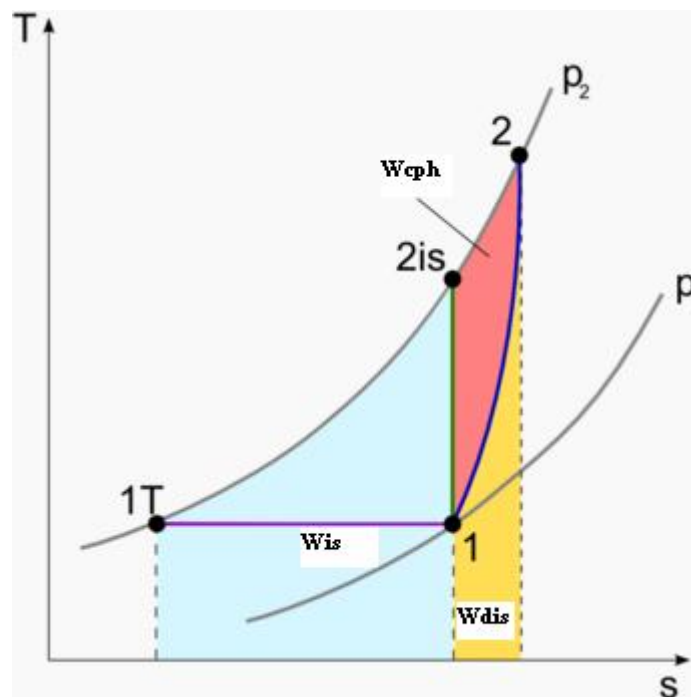


Figure A2.1 *Compression tranformation*

The real compression (1-2) needs more energy than the isentropic one (1-2_{is}) to be completed. This is due to internal machine friction losses that make the transformation possible only consequently to the Entropy increasing. Therefore

the total amount of energy necessary to complete the compression is given by three parts: isentropic work, energy to win friction loss, and finally the extra energy to face the gas expansion tendency (also called reheat) caused by the heat generated into friction loss.

$$W_{tot} = W_{is} + W_{diss} + W_{cph} \quad (A2.1)$$

The third term depends on the compressibility effects of the working fluid. This effect also makes that the lines of constant pressure in typical H-s or T-s diagrams are diverging. Hence, plotting into this diagram a compression process, the distance between 2-3'' will be greater than distance 2'-3' (Figure A2.2)

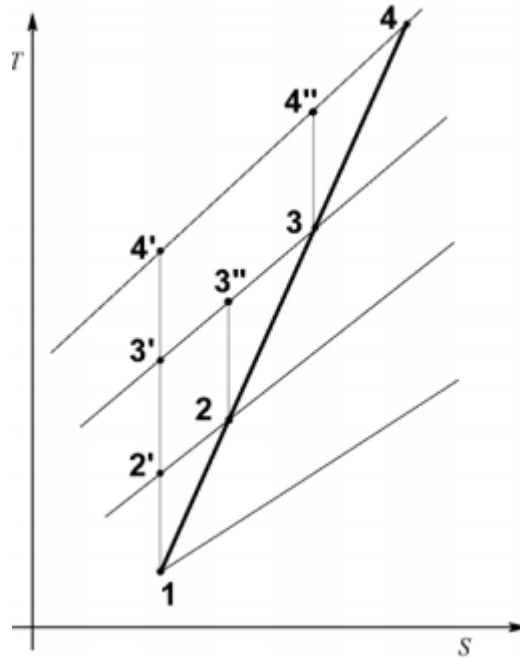


Figure A2.2 *Real adiabatic compression*

Similar considerations can be made for the expansion process.

In order keep into consideration the compressibility effects of fluids during compression or expansion processes, the polytropic efficiency has been introduced. Hence the polytropic efficiency sometimes is referred to as the true aerodynamic efficiency, since it eliminates the effects of pressure ratio; that is it defines the efficiency as if the fluid were incompressible. This concept is

frequently used to assess the compressibility effect on the efficiency of turbomachines by assuming that the polytropic efficiency is constant and independent of pressure ratio. Therefore the theoretical construct introduced by polytropic efficiency is more complex than the theoretical construct introduced by the definition of isentropic efficiency. The polytropic efficiency is referred to the ideal work throughout the real transformation 1-4.

Since the process is assumed to be a polytropic transformation with $p v^n = \text{constant}$, the relation for the polytropic compressor and turbine efficiencies reads:

$$\eta_{C_{pol}} = \frac{W_{tot} - W_{diss}}{W_{tot}} = \frac{n}{n-1} \frac{\gamma-1}{\gamma} \quad (\text{A2.2})$$

$$\eta_{T_{pol}} = \frac{W_{tot}}{W_{is} - W_{ph}} = \frac{\gamma}{\gamma-1} \frac{n-1}{n} \quad (\text{A2.3})$$

Where n is the Polytropic Index and γ is the Specific Heat ratio.

The polytropic compressor efficiency is always higher than the adiabatic (isentropic) compressor efficiency (see equation 4.12). On the contrary, the polytropic turbine efficiency is always lower than the adiabatic (isentropic) polytropic turbine efficiency (see equation 4.9).